MONASH University

DOCTORAL THESIS

General relativistic smoothed particle hydrodynamics with application to the tidal disruption of stars by supermassive black holes

DAVID LIPTAI

B.SC. (HONS)

A thesis submitted for the degree of

Doctor of Philosophy

at the School of Physics and Astronomy,
Monash University, Australia

March, 2020

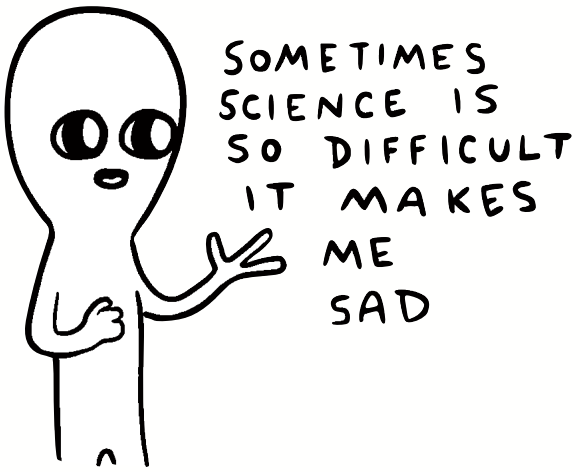

“ S C I E N T I S T ” — *Strange Planet* (Nathan W. Pyle)

COPYRIGHT NOTICE

ABSTRACT

Relativistic astrophysics has become an increasingly important field of study with the advent of gravitational wave detectors and an ever-growing number of observations of extremely luminous phenomena. These phenomena, such as active galactic nuclei, gamma-ray bursts and tidal disruption events, are powered by the accretion of matter onto black holes. Alongside observations, numerical methods are an important tool for studying these systems.

In this thesis, we develop a general relativistic smoothed particle hydrodynamics method for performing numerical hydrodynamics calculations in curved spacetimes around black holes. We perform rigorous tests of our method, demonstrating its ability to capture ultra-relativistic shocks and accurately reproduce Einstein and spin-induced precession.

We use this new numerical tool to simulate the tidal disruption of a one solar mass star by a million solar mass, spinning black hole. We consider both eccentric and parabolic stellar orbits. In the eccentric case, we investigate the effect of black hole spin on the formation of accretion discs from the fallback of stellar debris after disruption. We found that Lense-Thirring precession only delays disc formation by a few orbital periods. This broad conclusion is robust with respect to the initial orbital inclination, the penetration factor, and the black hole spin.

In the parabolic case, we follow the debris evolution self-consistently for one year after disruption, revealing the formation of an expanding asymmetric bubble of material with an optically thick inner region that encases the black hole. Previously hypothesised by a number of analytic studies, we found that this 'Eddington envelope' correctly reproduces some puzzling features of optical and UV emission from observed tidal disruption events. We measure a photospheric radius of $\sim$ 10–100 au, a photospheric temperature of $\approx 2.5 \times 10^4$ K that remains nearly constant with time, and a peak bolometric luminosity of $\sim 10^{44}$ erg/s. The optical light curve reflects the expansion and contraction of the photosphere, and is sensitive to the viewing angle. Our photosphere evolution shows remarkable agreement to the radii inferred from observations. We find accretion to be inefficient ($\sim 10^{-2} M_\odot/\mathrm{yr}$), powering mechanical outflows moving at speeds up to $\sim$ 20,000 km/s.

THESIS INCLUDING PUBLISHED WORKS DECLARATION

I hereby declare that this thesis contains no material which has been accepted for the award of any other degree or diploma at any university or equivalent institution and that, to the best of my knowledge and belief, this thesis contains no material previously published or written by another person, except where due reference is made in the text of the thesis.

This thesis includes one original paper published in a peer reviewed journal and two submitted publications. The core theme of the thesis is *general relativistic smoothed particle hydrodynamics and tidal disruption events*. The ideas, development and writing up of all the papers in the thesis were the principal responsibility of myself, the student, working within the School of Physics and Astronomy under the supervision of Daniel J. Price.

The inclusion of co-authors reflects the fact that the work came from active collaboration between researchers and acknowledges input into team-based research. In the case of Chapter 3, 5 and 6, and Appendices A, B and C, my contribution to the work involved the following:

- Chapter 3 and Appendix A: The writing of the publication, developing the code and conducting the simulations and subsequent analysis.
  Extent of contribution by candidate: 80%
  Publication title: General Relativistic Smoothed Particle Hydrodyamics
  Status: Published (2019, MNRAS, 485, 819)
  Co-author names: Daniel J. Price
  Nature of co-author's contribution: Comments and feedback during the writing of the paper, guidance in developing code structure, and suggestions for designing the time integration algorithm and shock capturing terms.

- Chapter 5 and Appendix B: The writing of the publication, implementing the isentropic formulation, and conducting the simulations and subsequent analysis.
  Extent of contribution by candidate: 80%
  Publication title: Disc formation from tidal disruption of stars on eccentric orbits by Kerr black holes using GRSPH
  Status: Submitted to the Monthly Notices of the Royal Astronomical Society (MNRAS)
  Co-author names: Daniel J. Price, Ilya Mandel, Giuseppe Lodato
  Nature of co-author's contribution: Comments and feedback during the writing of the paper, and suggesting how to implement efficient radiative cooling.

- Chapter 6 and Appendix C: The writing of the publication, and conducting the simulations and subsequent analysis.
  Extent of contribution by candidate: 70%
  Publication title: Eddington envelopes: The fate of stars on parabolic orbits tidally disrupted by supermassive black holes
  Status: Submitted to Nature
  Co-author names: Daniel J. Price, Ilya Mandel, Giuseppe Lodato, Yuri Levin
  Nature of co-author's contribution: Comments and feedback during the writing of the pa-

per, small edits to the discussion and suggesting how to compute the photosphere radius. The ideas in Appendix C.3 were conceptualised by Yuri Levin and written by Ilya Mandel.

I have renumbered sections and equations of submitted or published papers in order to generate a consistent presentation within the thesis.

Student signature:

Date: 29 November 2019

I hereby certify that the above declaration correctly reflects the nature and extent of the student's and co-authors' contributions to this work. In instances where I am not the responsible author, I have consulted with the responsible author to agree on the respective contributions of the authors.

Main Supervisor signature:

Date: 29 November 2019

ACKNOWLEDGEMENTS

I sincerely thank my supervisor Daniel Price for his continued and unwavering support throughout my Ph.D. He has undoubtedly shaped me into the scientist that I am today. It has been a pleasure to work with him not only because he is a great scientist and supervisor, but also because he is a good person.

I thank Paul Lasky, Bernhard Mueller and Yuri Levin for their feedback, advice and mentorship during my time at Monash. They are all incredible scientists and I have learnt a lot from working with them. I would also like to thank Ilya Mandel. Although we only worked together for a short time, his never-ending enthusiasm and his depth of knowledge was incredibly helpful during the final six months of my candidature. He was also kind enough to fund me after my scholarship ended, for which I am extremely grateful.

I acknowledge financial support from the Australian Government in the form of the Research Training Program (RTP) Scholarship. This research was also made possible by CPU time on OzStar, funded by Swinburne University and the Australian Government. I thank the School of Physics and Astronomy at Monash University for my J.L. William PhD Top Up Scholarship and financial support while travelling. A special thanks to Jean Pettigrew for her assistance and all the work she does to make life easier for each of us.

I am grateful to all the friends I have made on this journey. They are some of the most intelligent and wholesome people I know, and have made my life better because of it. There are too many to list, but I want to thank Conrad, Hayley and Zac in particular, my 'PhD siblings', for helping me get through the tough times and providing the laughs.

Finally, I want to thank my family, Valeria, Robert, Suzie and Peter for their unconditional love and support. It's been a tough road to get here, but they have always believed in me and been there whenever I needed them. I am glad they can share in my success, since I wouldn't have made it here without them.

Contents

1 Introduction **1**

2 Background: Smoothed particle hydrodynamics **5**
2.1 Non-relativistic fluid dynamics 5
2.1.1 Continuum equations 5
2.1.2 Computing density 6
2.1.3 Equations of motion 8
2.1.4 Conservation properties and energy equation 9
2.1.5 Shock capturing 10
2.1.6 Evolving entropy 13
2.1.7 Time integration – Leapfrog 13
2.2 Relativistic fluid dynamics 14
2.2.1 Continuum equations 15
2.2.2 Computing density 15
2.2.3 Equations of motion 15
2.2.4 Conservation properties and energy equation 16

3 General Relativistic Smoothed Particle Hydrodynamics **19**
3.1 Introduction 19
3.2 Relativistic hydrodynamics 20
3.2.1 Definitions 20
3.2.2 Conserved variables 21
3.2.3 Equations of relativistic hydrodynamics 21
3.3 SPH Equations of relativistic hydrodynamics 22
3.3.1 Interpolating kernel 23
3.4 Shock capturing 24
3.4.1 Artificial viscosity 26
3.4.2 Artificial conductivity 26
3.4.3 Signal speed — viscosity 27
3.4.4 Signal speed — conductivity 27
3.5 Evolving entropy 28
3.6 Time Integration 29
3.6.1 Generalised leapfrog method 29
3.6.2 Alternative generalised leapfrog method 29
3.6.3 Hybrid leapfrog, and implementation in GRSPH 30

3.6.4 Timestep constraint . . . 32
3.7 Recovery of primitive variables . . . 32
3.8 Numerical tests . . . 34
3.8.1 Special Relativity . . . 35
3.8.2 Orbital dynamics — Schwarzschild Metric . . . 41
3.8.3 Orbital dynamics — Kerr Metric . . . 47
3.8.4 General relativity — Bondi accretion . . . 49
3.9 Conclusions . . . 52

4 Background: Tidal disruption events 53
4.1 Disruption . . . 53
4.2 Fallback . . . 55

5 Disc formation from tidal disruption of stars on eccentric orbits by Kerr black holes using GRSPH 59
5.1 Introduction . . . 59
5.2 Method . . . 61
5.2.1 Setup . . . 61
5.2.2 Accretion luminosity and heating rate . . . 62
5.2.3 Radiative cooling . . . 64
5.3 Results . . . 64
5.3.1 Disc formation around Schwarzschild black holes . . . 64
5.3.2 Disc formation around Kerr black holes . . . 64
5.3.3 Energy injection rate . . . 67
5.3.4 Misalignment angle . . . 68
5.3.5 Remnant disc properties . . . 68
5.3.6 Penetration factor . . . 69
5.3.7 Radiative efficiency . . . 70
5.4 Discussion . . . 72
5.5 Conclusion . . . 75

6 Eddington envelopes: The fate of stars on parabolic orbits tidally disrupted by supermassive black holes 77
6.1 Introduction . . . 77
6.2 Method . . . 79
6.3 Results . . . 79
6.4 Discussion . . . 86
6.5 Conclusions . . . 88

7 Conclusions 89
7.1 Summary . . . 89
7.2 Future work . . . 90
7.2.1 Applications . . . 90
7.2.2 Methods . . . 91

A GRSPH **93**
A.1 Positivity of the entropy change . . . 93
A.1.1 Conductivity . . . 93
A.1.2 Viscosity . . . 94
A.2 Recovery of primitive variables . . . 94
A.3 Metrics in Cartesian Coordinates . . . 95
A.3.1 Schwarzschild metric . . . 95
A.3.2 Kerr metric . . . 96
A.3.3 Derivatives of the metric . . . 98
A.3.4 Inverse . . . 98
A.4 Computing oscillation frequencies . . . 98

B Tidal disruption of stars on eccentric orbits **99**
B.1 Effect of resolution . . . 99
B.2 Self-gravity . . . 99

C Tidal disruption of stars on parabolic orbits **103**
C.1 Effect of resolution . . . 103
C.2 Radiatively efficient cooling and disc formation . . . 103
C.3 Stream disruption . . . 103

List of Figures

2.1 Approaches to calculating density 6
2.2 Comparison between the cubic spline and Gaussian 7
2.3 Non-relativistic Sod-shock tube 12
2.4 Non-relativistic Sod-shock tube with no conductivity 12
2.5 Leapfrog vs RK2 14

3.1 Mildly relativistic shock performed in 1D, with artificial conductivity 33
3.2 Mildly relativistic shock performed in 3D, with artificial conductivity 33
3.3 Mildly relativistic shock performed in 1D, without artificial conductivity 34
3.4 Relativistic blast wave in 1D 36
3.5 Relativistic blast wave in 3D 36
3.6 Density spike at different resolutions for the blast wave problem in 1D 37
3.7 Sine wave shocktube in 1D and 3D 37
3.8 Shocktube in 1D with initial transverse velocity on the right side of the interface . 40
3.9 Shocktube in 1D with initial transverse velocity on both sides of the interface . . 40
3.10 Spherical blast wave in 3D 42
3.11 Slice through the spherical blast wave in 3D showing the primitive density ρ. . . 42
3.12 Maximum (central) density ρ^* and total gravitational potential energy for the oscillating polytrope 42
3.13 Circular orbits computed in the Schwarzschild and Kerr metrics 43
3.14 Epicyclic frequency and vertical oscillation frequency 43
3.15 Velocity as a function of radius for radially infalling test particles 44
3.16 Precession in the Schwarzschild and Kerr metrics 44
3.17 Fractional error in angular momentum throughout the precessing orbit in the Schwarzschild metric 45
3.18 Spherically symmetric 'geodesic' Bondi accretion without artificial viscosity . . 45
3.19 Spherically symmetric 'geodesic' Bondi accretion with artificial viscosity 45
3.20 Spherically symmetric 'sonic point' Bondi accretion with reduced artificial viscosity 46
3.21 Spherically symmetric 'sonic point' Bondi accretion with standard artificial viscosity 46
3.22 Rendered slices of spherically symmetric 'sonic point' Bondi accretion 46

4.1 Parameter space for the tidal disruption of different types of stars 54
4.2 Trajectory of the star and stellar debris during a TDE 55
4.3 Distribution of specific energy in a hydrodynamical simulation of a TDE 57

4.4 Light curves of observed tidal disruption events 57

5.1 Snapshots of the debris fallback in the adiabatic, Schwarzschild TDE simulation . 63
5.2 Snapshots of the debris fallback in the adiabatic, Kerr TDE simulation 63
5.3 Energy injection rate ($L_{\rm shock}$) and accretion luminosity ($L_{\rm acc}$) in adiabatic simulations 65
5.4 Effect of inclination on $L_{\rm acc}$ and $L_{\rm shock}$ 66
5.5 Cross sections of final tori for varying initial inclinations 67
5.6 Surface density profile of the final torus 68
5.7 Effect of penetration factor on debris circularisation 69
5.8 Effect of penetration factor on $L_{\rm acc}$ and $L_{\rm shock}$ 70
5.9 Snapshots of the debris fallback in the isentropic, Schwarzschild TDE simulation 71
5.10 Snapshots of the debris fallback in the isentropic, Kerr TDE simulation 71
5.11 $L_{\rm acc}$ and $L_{\rm shock}$ in isentropic calculations 73

6.1 One year in the life of a tidal disruption event 80
6.2 Distributions in density, radial velocity and temperature at one year post disruption 81
6.3 Evolution of the energy dissipation rate, accretion luminosity, photspheric radius and photon diffusion timescale 82
6.4 One year in the life of a $\beta = 5$ tidal disruption event 83
6.5 Photospheric radius and temperature evolution for a $\beta = 5$ TDE 84

A.1 Measuring epicyclic frequency 98

B.1 Effect of resolution on debris circularisation in eccentric TDE simulations 100
B.2 Effect of resolution on mass accretion rate in eccentric TDE simulations 101

C.1 Effect of resolution in parabolic TDE simulations 104
C.2 Disc formation assuming an isentropic evolution in parabolic TDE simulations . 104

Chapter 1

Introduction

Black holes power the brightest objects in the universe. They allow matter to release enormous amounts of gravitational potential energy during accretion. This is in part due to their large mass, but also due to their extreme compactness, since the gravitational potential energy per unit mass available from an object of mass M and radius R scales as $\propto M/R$. A black hole with the mass of the Sun has a radius of only ≈ 3 km, roughly a factor of 2×10^5 smaller than the radius of the Sun. This means that matter has the potential to release 200,000 times more energy by landing onto a solar mass black hole than by landing onto the Sun! It is this energy that powers gamma-ray bursts (GRBs), quasars and active galactic nuclei (AGN), X-ray binaries, and tidal disruption events (TDEs).

Although fundamentally relativistic, the basic concept of a black hole can be understood using Newtonian physics. John Michell and Pierre-Simon Laplace both independently put forth the idea of a 'dark star' in 1784 and 1796, respectively, more than two centuries ago (Montgomery et al., 2009). They considered an object that is so massive that the escape velocity at its surface is equal to (or exceeds) the speed of light. Assuming that light is affected in the same way as ordinary matter by gravity, then these objects would be 'invisible' or 'dark', in the sense that no light would be able to escape from them. The radius for such an object is $R = 2GM/c^2$, where M is its mass, G is the gravitational constant and c is the speed of light, which turns out to give the correct location of the event horizon (see below).

Our modern understanding of black holes is as solutions to Einstein's field equations of gravitation (Einstein, 1915). Initially, Einstein believed that his equations were so complex that no analytic solution would be found. However, only a year later, Schwarzschild (1916) found a spherically symmetric, static, vacuum solution, which describes spacetime around a non-rotating point mass, or black hole. It has a true singularity at $r = 0$, which is the black hole, and a coordinate singularity at $r_s = 2GM/c^2$, known as the *Schwarzschild radius*. The surface bounded by r_s is called the *event horizon*, since anything that crosses this invisible boundary becomes causally disconnected from the outside universe (Finkelstein, 1958) and will inevitably fall into the central singularity; even light cannot escape. The more general solution for a rotating black hole was found by Kerr (1963) for which the event horizon depends on the black hole angular momentum.

Although the solutions to Einstein's equations allow for the existence of black holes with arbitrary mass, we are currently aware of two[1] distinct classes of astrophysical black holes: stellar-

[1] There is some evidence to suggest that there exists a third class of intermediate-mass black holes, $\sim 10^2 - 10^4 M_\odot$, at the centres of large globular clusters, but this is still not known for certain (Bambi, 2018).

mass black holes that are five to several ten times the mass of the Sun, and supermassive black holes hundreds of thousands to tens of billions times the mass of the Sun. Stellar-mass black holes are formed by the gravitational collapse of massive stars (Oppenheimer and Snyder, 1939; Oppenheimer and Volkoff, 1939), while supermassive black holes exist at the centres of galaxies. The origin and formation of supermassive black holes, however, is still not well understood, since with even optimistic estimates of their growth rate it is difficult to produce these massive objects from small seed black holes within the age of the Universe.

For many years, black holes were thought to be purely theoretical objects. Generally, most people believed that some unknown mechanism would prevent the gravitational collapse of massive bodies from forming black holes. It was not until the development of radio astronomy, which allowed for the discovery of luminous and compact sources at the centres of galaxies (e.g. quasars, Schmidt, 1963), when people began to consider the reality of black holes more seriously, since it was only supermassive black holes that were compact enough to power these phenomena (Zel'dovich, 1964; Salpeter, 1964). Similarly, strong X-ray sources such as Cygnus X-1 were identified to be powered by stellar-mass black holes (Bolton, 1972; Webster and Murdin, 1972). Since then, 'an increasing number of astronomical observations have pointed out the existence of stellar-mass black holes in some X-ray binaries (Remillard and McClintock, 2006) and of supermassive black holes at the centre of many galaxies (Kormendy and Richstone, 1995)' (Bambi, 2018).

In 2015, the Laser Interferometer Gravitational-Wave Observatory (LIGO) made the first direct detection of gravitational waves from the merger of two stellar-mass black holes (Abbott et al., 2016). This was concrete evidence for the existence of black holes, and brought relativistic astrophysics, particularly the study of black holes, into the forefront of astronomical research. In the next three years, the Large Synoptic Survey Telescope (LSST) will become fully operational and will be able to observe AGN and other luminous sources over the whole sky, with unprecedented detail (Ivezić et al., 2019). It will also dramatically increase the number of black hole transients observed, which will be particularly useful for the study of flares from the tidal disruption of stars by supermassive black holes, of which only several dozen have been observed so far (Komossa, 2015; Stone et al., 2019). The rate of TDE detections with LSST is expected to be between approximately 3000–8000 per year (Thorp et al., 2019; Bricman and Gomboc, 2020), which will help explain many of the puzzling features of recently detected TDEs in the optical/UV (e.g. van Velzen et al., 2011) (see Chapter 6).

In addition to an increased number and better quality of observations, our understanding of the many luminous phenomena powered by black holes can also be aided by numerical simulations. The method of smoothed particle hydrodynamics (SPH) is particularly useful for modelling many of these systems since in SPH the resolution follows mass. This makes it relatively easy to simulate geometrically complex and dynamic systems over a wide range of spatial scales. The main limitation of current implementations of SPH however, is the approximate treatment of general relativity in relativistic hydrodynamics (Metzger, 2017). Since black holes are fundamentally relativistic, this can be a significant drawback, especially in modelling tidal disruptions of stars for which relativistic effects, such as orbital precession, are thought to play a crucial role (see Chapter 5).

The aim of this thesis is to develop a new computational tool for performing hydrodynamics in curved spacetimes and to apply it to the study of the tidal disruption of stars by supermassive black holes. The structure of the thesis is as follows: In Chapter 2, we review and introduce some of

the basic concepts relevant for non-relativistic and relativistic smoothed particle hydrodynamics. In Chapter 3, we formulate our general relativistic smoothed particle hydrodynamics method and implement it within an existing SPH code, performing rigorous numerical tests. Following this, we give a brief background on tidal disruption events in Chapter 4, before undertaking two numerical studies on TDEs using our newly developed code. In Chapter 5, we investigate disc formation from the tidal disruption of stars on bound, eccentric orbits by rotating supermassive black holes. We then investigate the disruption of stars on marginally bound, parabolic orbits in Chapter 6, in which we find the formation of an optically thick Eddington-envelope that may explain the puzzling optical and UV emission observed in TDEs.

Chapter 2

Background: Smoothed particle hydrodynamics

2.1 Non-relativistic fluid dynamics

Here we briefly review the fundamentals of non-relativistic smoothed particle hydrodynamics (SPH), much of which is relevant to the formulation of general relativistic SPH discussed in Section 2.2 and Chapter 3. For a more comprehensive review, including the formulation of magnetohydrodynamics and dust, see e.g. Price (2012) or Monaghan (2005).

SPH is a Lagrangian numerical method for solving the fluid equations, and was first formulated by Lucy (1977) and independently by Gingold and Monaghan (1977). It discretises fluid by mass (rather than volume) into what are typically referred to as particles. This terminology can be somewhat confusing, however, since they do not represent real particles, but rather they should be thought of as resolution points moving with the fluid, keeping track of hydrodynamic quantities such as velocity, density and thermal energy.

Since the resolution points follow the mass in the fluid, SPH is well suited to model a variety of astrophysical problems, which typically have complex, dynamically evolving geometries, and density contrasts of many orders of magnitude. Examples include: i) cosmological structure formation (e.g. Springel and Hernquist, 2003; Borgani et al., 2004; Governato et al., 2007); ii) galaxy mergers (e.g. Barnes and Hernquist, 1991; Mihos and Hernquist, 1996; Di Matteo et al., 2005); iii) star cluster formation (e.g. Bate et al., 2003; Clark et al., 2008; Liptai et al., 2017); iv) the mergers of stars (e.g. Benz and Hills, 1987; Oechslin et al., 2007); v) planet formation (e.g. Mayer et al., 2002; Lufkin et al., 2004; Dipierro et al., 2016); vi) black hole accretion (e.g. Lanzafame et al., 1998; Lodato and Price, 2010; Nealon et al., 2015); and vii) tidal disruption of stars by black holes (e.g. Evans and Kochanek, 1989; Laguna et al., 1993; Hayasaki et al., 2013).

2.1.1 Continuum equations

First, we present the equations of compressible hydrodynamics in continuum form before deriving their discrete counterparts. The Lagrangian form of the fluid equations are given by

$$\frac{d\rho}{dt} = -\rho\nabla\cdot\mathbf{v}, \tag{2.1}$$

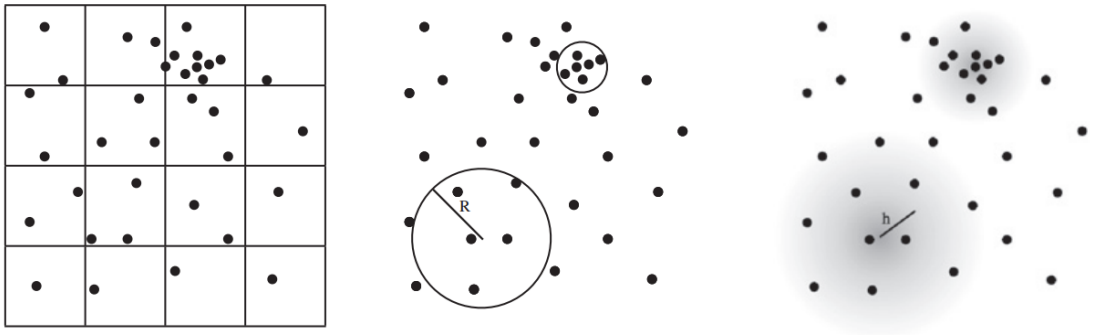

Figure 2.1: Approaches to calculating density at points in space given an arbitrary distribution of point mass particles (Price, 2012). *Left:* sampling via a fixed mesh *Middle:* local sampling with spheres *Right:* weighted local sampling.

$$\frac{d\mathbf{v}}{dt} = -\frac{\nabla P}{\rho}, \tag{2.2}$$

$$\frac{de}{dt} = -\frac{1}{\rho}\nabla \cdot (P\mathbf{v}), \tag{2.3}$$

where ρ, $\mathbf{v}$, and P are the density, velocity, and pressure of the fluid, respectively. The total energy per unit mass is $e \equiv \frac{1}{2}\mathbf{v} \cdot \mathbf{v} + u$, where u is the specific thermal energy. The Lagrangian time derivative is defined according to

$$\frac{d}{dt} \equiv \frac{\partial}{\partial t} + \mathbf{v} \cdot \nabla. \tag{2.4}$$

2.1.2 Computing density

SPH is founded on the way it computes density at any point in space given an arbitrary distribution of particles. Figure 2.1 from Price (2012) illustrates three approaches to this problem. Most straightforward is to simply construct a mesh and count the number of particles that fall within each cell (Figure 2.1 *left*). While this approach is simple in its implementation, it cannot sample both high and low density regions uniformly with a fixed mesh. An alternative, to address the issue of under/oversampling, is to take samples using spheres containing a fixed number of particles (Figure 2.1 *middle*). But this is also problematic because it is sensitive to particles that lie close to the sampling spheres, which leads to a noisy estimate of the density.

A better approach and the one that SPH follows is to use weighted local sampling, where the contribution of each particle to the density estimate drops off with distance (Figure 2.1 *right*). That is, particles that are further away should contribute less to the density estimate than particles that are closer. This can be represented by

$$\rho(\mathbf{r}) = \sum_{b=1}^{N} m_b W(|\mathbf{r} - \mathbf{r}_b|, h), \tag{2.5}$$

where ρ is the density at a point in space $\mathbf{r}$, N is the number of particles, m_b and $\mathbf{r}_b$ are the mass and position of neighbouring particles, W is a weighting function (or smoothing kernel), and h is the smoothing length, which characterises the fall-off of W with distance.

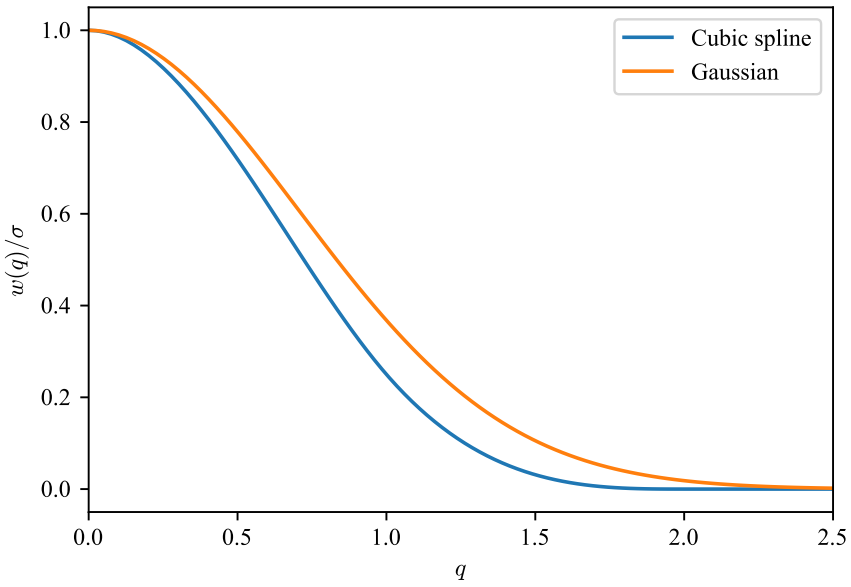

Figure 2.2: Comparison between the cubic spline (Eq. 2.8) and Gaussian, $w(q) = \sigma \exp(-q^2)$. Note: the normalisation constant σ is different for each function.

In order for Equation 2.5 to be dimensionally correct, W must have dimensions of inverse volume. It must also be normalised such that mass is conserved. That is,

$$\int_V \rho(\mathbf{r}) dV = \sum_{b=1}^{N_{\text{neigh}}} m_b = M_{\text{tot}}, \tag{2.6}$$

where M_{tot} is the mass contained in the volume V that is enclosed by the kernel W, and N_{neigh} is the number of particles in V. Substituting Eq. 2.5 into Eq. 2.6 gives

$$\int_V W(|\mathbf{r} - \mathbf{r}_b|, h) dV = 1. \tag{2.7}$$

The functional form of W must be chosen carefully since this determines the accuracy of the density estimate. An intuitive choice is a Gaussian since it is always positive, decreases monotonically, is smooth and has smooth derivatives, and gives a weighting to all particles. But, with computational costs in mind, a Gaussian is a poor choice since computing the density sum (Eq. 2.5) on each of the N particles would scale as $\mathcal{O}(N^2)$ (i.e. $N_{\text{neigh}} = N$). For this reason, kernels that are truncated after a finite distance, known as having compact-support, are more desirable from a computational standpoint.

The most common class of kernels used in practice are the B-splines. These functions are Gaussian shaped but tend to zero after a finite distance (see Figure 2.2). The cubic spline, for example, is given by

$$w(q) = \sigma \begin{cases} \frac{1}{4}(2-q)^3 - (1-q)^3, & 0 \leq q < 1; \\ \frac{1}{4}(2-q)^3, & 1 \leq q < 2; \\ 0, & q \geq 2, \end{cases} \tag{2.8}$$

where σ is a normalisation constant (equal to $1/\pi$ in 3D). In order to have dimensions of inverse volume, the kernel is then defined according to

$$W(|\mathbf{r}-\mathbf{r}_b|,h) \equiv \frac{1}{h^d} w(q), \tag{2.9}$$

where d is the number of dimensions, and $q \equiv |\mathbf{r}-\mathbf{r}_b|/h$.

When using kernels with compact support, the number of particles contained by the kernel $N_{\rm neigh}$ should be kept roughly constant to ensure uniform sampling. This means that, if all particles have the same mass m, the smoothing length h must depend on the local density. In other words, low density regions require a large sampling volume (large h) and high density regions require a small sampling volume (small h). We can represent this relation according to

$$h(\mathbf{r}) = h_{\rm fac}\left(\frac{m}{\rho(\mathbf{r})}\right)^{1/d}, \tag{2.10}$$

where $h_{\rm fac}$ is a numerical factor to control the average number of neighbours (or particles sampled) [1]. Thus Equations 2.5 and 2.10 are coupled and must be solved simultaneously in practice. This is typically done via a bisection or Newton-Raphson root-finding algorithm (Price and Monaghan, 2007).

2.1.3 Equations of motion

The equations of motion in SPH can be derived from the discrete Lagrangian

$$L = \sum_b m_b \left[\frac{1}{2}\mathbf{v}_b\cdot\mathbf{v}_b - u(\rho_b,s_b)\right], \tag{2.11}$$

where $u(\rho_b,s_b)$ is the specific thermal energy of each particle, which is a function of its density ρ_b and specific entropy s_b. Here, we consider a fluid in the absence of any external forces, magnetic fields, or other physics. From the principle of least action, the Euler-Lagrange equations for each particle a are:

$$\frac{d}{dt}\left(\frac{\partial L}{\partial \mathbf{v}_a}\right) - \frac{\partial L}{\partial \mathbf{r}_a} = 0. \tag{2.12}$$

The relevant derivatives are given by

$$\frac{\partial L}{\partial \mathbf{v}_a} = m_a \mathbf{v}_a, \tag{2.13}$$

$$\frac{\partial L}{\partial \mathbf{r}_a} = -\sum_b m_b \left.\frac{\partial u_b}{\partial \rho_b}\right|_s \frac{\partial \rho_b}{\partial \mathbf{r}_a}, \tag{2.14}$$

and from the first law of thermodynamics

$$du = Tds + \frac{P}{\rho^2}d\rho, \tag{2.15}$$

where T is the gas temperature, in the absence of dissipation (i.e. constant entropy s) we have

$$\left.\frac{\partial u_b}{\partial \rho_b}\right|_s = \frac{P_b}{\rho_b^2}. \tag{2.16}$$

[1] In practice we use $h_{\rm fac} = 1.2$ when using the cubic spline, which corresponds to an average of 57.9 neighbours.

Taking the derivative of Equation 2.5 and using Equations 2.13, 2.14 and 2.16 in Equation 2.12 it can be shown that the equations of motion are given by

$$\frac{d\mathbf{v}_a}{dt} = -\sum_b m_b \left[\frac{P_a}{\Omega_a \rho_a^2} \frac{\partial W_{ab}(h_a)}{\partial \mathbf{r}_a} + \frac{P_b}{\Omega_b \rho_b^2} \frac{\partial W_{ab}(h_b)}{\partial \mathbf{r}_a} \right] \tag{2.17}$$

where

$$\Omega_a \equiv \left[1 - \frac{\partial h_a}{\partial \rho_a} \sum_b m_b \frac{\partial W_{ab}(h_a)}{\partial h_a} \right], \tag{2.18}$$

and we have defined $W_{ab}(h) = W(|\mathbf{r}_a - \mathbf{r}_b|, h)$ for simplicity in notation. Equation 2.17 is the discretised version of Equation 2.2.

The equations of motion can also be derived using kernel interpolation theory (e.g. Monaghan, 1992). However, in the context of this thesis, it is more useful to consider the derivation from a Lagrangian since the analogous relativistic equations are best derived in a similar fashion. Beginning with a Lagrangian also highlights some important conservation properties.

2.1.4 Conservation properties and energy equation

Since our equations are derived from a Lagrangian, the discrete system will maintain the Hamiltonian properties that arise from symmetries in the Lagrangian. In particular, the Lagrangian is invariant under translations and rotations in space. It is also symmetric in time and invariant under time translations. This amounts to the exact conservation of linear momentum, angular momentum, and energy. Consider for example the time derivative of the Hamiltonian (or total energy E):

$$\frac{d}{dt}(H) = \frac{d}{dt}\left(\sum_a \mathbf{v}_a \cdot \frac{\partial L}{\partial \mathbf{v}_a} - L \right) \tag{2.19}$$

$$= \frac{d}{dt} \sum_a m_a \left(\frac{1}{2} \mathbf{v}_a \cdot \mathbf{v}_a + u_a \right), \tag{2.20}$$

$$= \sum_a m_a \left(\mathbf{v}_a \cdot \frac{d\mathbf{v}_a}{dt} + \frac{du_a}{dt} \right). \tag{2.21}$$

From the first law of thermodynamics (Eq. 2.16) we have the relation

$$\frac{du_a}{dt} = \frac{P_a}{\rho_a^2} \frac{d\rho_a}{dt}. \tag{2.22}$$

which, after taking the time derivative of Equation 2.5 becomes

$$\frac{du_a}{dt} = \frac{P_a}{\Omega_a \rho_a^2} \sum_b m_b (\mathbf{v}_a - \mathbf{v}_b) \cdot \frac{\partial W_{ab}(h_a)}{\partial \mathbf{r}_a}. \tag{2.23}$$

Substituting the momentum and thermal energy equations (Eq. 2.17 and 2.23) into Equation 2.21 we obtain

$$\frac{dE}{dt} = -\sum_a \sum_b m_a m_b \left(\frac{P_a \mathbf{v}_b}{\Omega_a \rho_a^2} \cdot \frac{\partial W_{ab}(h_a)}{\partial \mathbf{r}_a} + \frac{P_b \mathbf{v}_a}{\Omega_b \rho_b^2} \cdot \frac{\partial W_{ab}(h_b)}{\partial \mathbf{r}_a} \right) = 0, \tag{2.24}$$

where the double sum equals zero because of the anti-symmetry of the kernel gradient. (You can relabel/switch the summation indices for half of the sum and add it to the original half to get zero). Similarly, it can be shown that

$$\frac{d}{dt}\sum_a m_a \mathbf{v}_a = 0, \tag{2.25}$$

$$\frac{d}{dt}\sum_a \mathbf{r}_a \times m_a \mathbf{v}_a = 0, \tag{2.26}$$

that is, linear and angular momentum are conserved exactly.

Since the total energy is $E = \sum_a m_a e_a$ where e_a is the specific energy per particle, Equation 2.24 allows us to identify the discrete version of the continuum energy equation (Eq. 2.3)

$$\frac{de_a}{dt} = -\sum_b m_b \left(\frac{P_a \mathbf{v}_b}{\Omega_a \rho_a^2} \cdot \frac{\partial W_{ab}(h_a)}{\partial \mathbf{r}_a} + \frac{P_b \mathbf{v}_a}{\Omega_b \rho_b^2} \cdot \frac{\partial W_{ab}(h_b)}{\partial \mathbf{r}_a} \right). \tag{2.27}$$

Note that since both Eq.2.23 and 2.27 are derived from the Lagrangian there is no difference in terms of conservation when evolving either u or e in practice.

2.1.5 Shock capturing

When deriving Equation 2.17 we implicitly assumed that the Lagrangian was a differentiable function of the coordinates. This assumption means that we have excluded the possibility of discontinuous solutions (i.e. shocks), which means that, in practice, discontinuities require careful treatment. The standard approach is to add dissipative terms into the SPH equations, which smooth discontinuities over a few h. The 'careful' part is in constructing the dissipative terms in such a way that they only 'activate' near shocks, that they don't break the conservation laws in Section 2.1.4, and that they only ever increase the total entropy.

One way to design shock capturing terms is by analogy to Riemann solvers. The advantage of following this line of thinking is that it gives a fairly simple procedure for constructing shock capturing terms when more complex physics is required (such as magnetic fields and/or relativistic hydrodynamics). In fact, this was first put forward by Chow and Monaghan (1997) in the context of special relativistic SPH and later generalised to non-relativistic SPH by Monaghan (1997).

The basic idea is to consider two particles as the left and right states of the Riemann problem, and identify that in approximate Riemann solvers the dissipative term acts on jumps in the conservative variables. The conservative variables in non-relativistic hydrodynamics are the specific momentum $\mathbf{p} = \mathbf{v}$ and specific energy $e = \frac{1}{2}(\mathbf{v}\cdot\mathbf{v}) + u$ (and also density ρ, but this does not require dissipation since Eq. 2.5 is an integral representation of the continuity equation). Thus the dissipative terms should be something like

$$\left.\frac{d\mathbf{v}_a}{dt}\right|_{\text{diss}} = \sum_b C_{ab} v_{\text{sig}} (\mathbf{v}_a - \mathbf{v}_b), \tag{2.28}$$

$$\left.\frac{de_a}{dt}\right|_{\text{diss}} = \sum_b D_{ab} v_{\text{sig}} (e_a - e_b), \tag{2.29}$$

where C_{ab} and D_{ab} are factors to be determined, and v_{sig} is the maximum signal speed.

(A more in-depth discussion of this in the context of relativistic hydrodynamics is in Section 3.4, thus for the discussion here we merely state the dissipative terms for reference).

In PHANTOM (Price et al., 2018), we use

$$\left.\frac{d\mathbf{v}_a}{dt}\right|_{\rm diss} = -\sum_b m_b \left[\frac{q^a_{ab}}{\Omega_a\rho_a^2}\frac{\partial W_{ab}(h_a)}{\partial \mathbf{r}_a} + \frac{q^b_{ab}}{\Omega_b\rho_b^2}\frac{\partial W_{ab}(h_b)}{\partial \mathbf{r}_a}\right], \tag{2.30}$$

$$\left.\frac{du_a}{dt}\right|_{\rm diss} = -\frac{1}{\Omega_a\rho_a}\sum_b m_b v_{{\rm sig},a}\frac{1}{2}(\mathbf{v}_{ab}\cdot\hat{\mathbf{r}}_{ab})^2 F_{ab}(h_a) + \sum_b m_b \alpha_u v^u_{\rm sig}(u_a-u_b)\frac{1}{2}\left[\frac{F_{ab}(h_a)}{\Omega_a\rho_a} + \frac{F_{ab}(h_b)}{\Omega_b\rho_b}\right], \tag{2.31}$$

which can be shown to reduce to forms similar to Equations 2.28 and 2.29. Here, $\mathbf{v}_{ab} \equiv \mathbf{v}_a - \mathbf{v}_b$, $\hat{\mathbf{r}}_{ab} \equiv (\mathbf{r}_a - \mathbf{r}_b)/|\mathbf{r}_a - \mathbf{r}_b|$ is the unit vector along the line of sight between the particles, and $F_{ab}(h) \equiv \hat{\mathbf{r}}_{ab}\cdot\partial W_{ab}(h)/\partial\mathbf{r}_a$ is the scalar part of the kernel gradient. We set

$$q^a_{ab} = \begin{cases} -\frac{1}{2}\rho_a v_{{\rm sig},a}\mathbf{v}_{ab}\cdot\hat{\mathbf{r}}_{ab}, & \mathbf{v}_{ab}\cdot\hat{\mathbf{r}}_{ab} < 0 \\ 0, & \text{otherwise.}\end{cases} \tag{2.32}$$

That is, artificial viscosity only applies to approaching particles. The maximum signal speed is

$$v_{{\rm sig},a} = \alpha^{\rm AV}_a c_{{\rm s},a} + \beta^{\rm AV}|\mathbf{v}_{ab}\cdot\hat{\mathbf{r}}_{ab}|, \tag{2.33}$$

where in general $\alpha^{\rm AV}_a$ and $\beta^{\rm AV}$ are numerical parameters to control the amount of dissipation. Typically $\alpha^{\rm AV} \in [0,1]$ is controlled by a switch, while $\beta^{\rm AV} = 2$ by default.

The second term in Equation 2.31 acts as thermal conduction, and is deliberately separate from the artificial viscosity. i.e. The jump in thermal energy $(u_a - u_b)$ is controlled by a different numerical parameter α_u. It also has a different signal speed, $v^u_{\rm sig}$, since artificial conductivity is mainly used to treat contact discontinuities, which travel at a different speed to the shock. In PHANTOM, we use two versions of $v^u_{\rm sig}$, depending on the physics involved (cf. Price, 2008, 2012). For problems that do not involve self-gravity or external forces we use

$$v^u_{\rm sig} = \sqrt{\frac{P_a - P_b}{\rho_{ab}}}, \tag{2.34}$$

where $\rho_{ab} \equiv (\rho_a + \rho_b)/2$, and we use

$$v^u_{\rm sig} = |\mathbf{v}_{ab}\cdot\hat{\mathbf{r}}_{ab}|, \tag{2.35}$$

for problems that do.

Early SPH shock capturing formulations were not constructed by analogy to Riemann solvers, and thus did not include a conductivity term. This meant that they had difficulty treating problems involving a contact discontinuity (Price, 2008) (such as the Kelvin-Helmholtz instability). The issue with contact discontinuities is demonstrated in Figures 2.3 and 2.4, which show 1D SPH simulations of the Sod-shock tube both with and without artificial conductivity ($\alpha_u = 1.0$ and $\alpha_u = 0$, respectively). Without conductivity, there is a characteristic blip in the pressure and thermal energy at the contact discontinuity. When artificial conductivity is included in the simulation the blip is smoothed out.

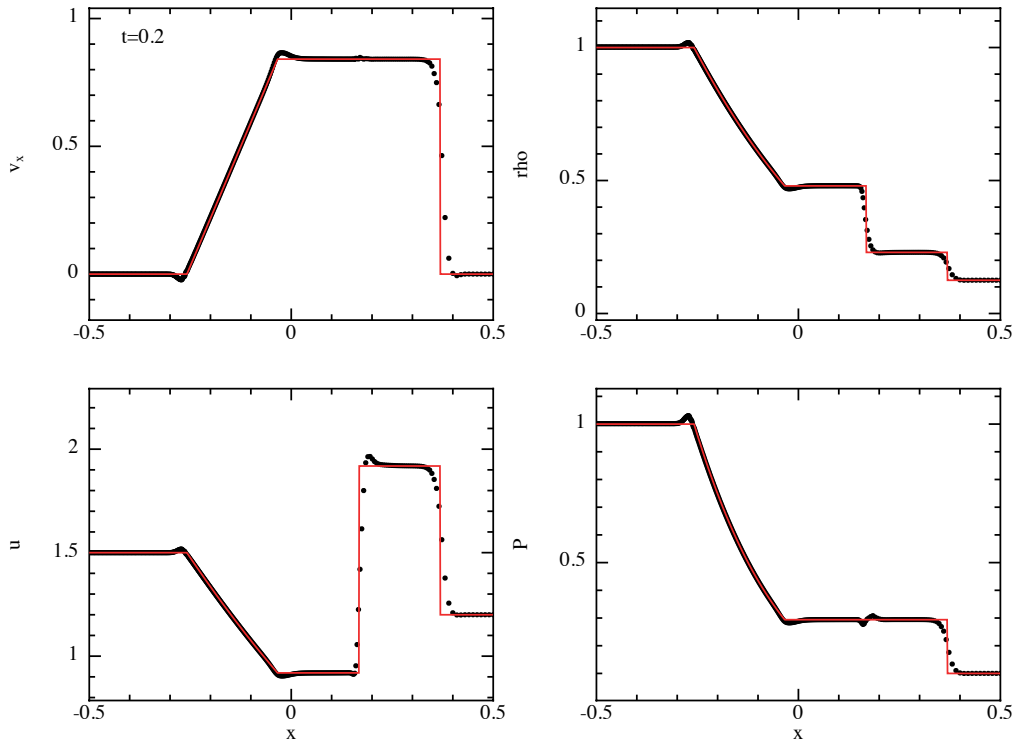

Figure 2.3: Results of the Sod-shock tube test in 1D with both artificial viscosity and conductivity. Black circles correspond to SPH particles, while the red line is the exact solution. Artificial dissipation smooths each discontinuity over a few h.

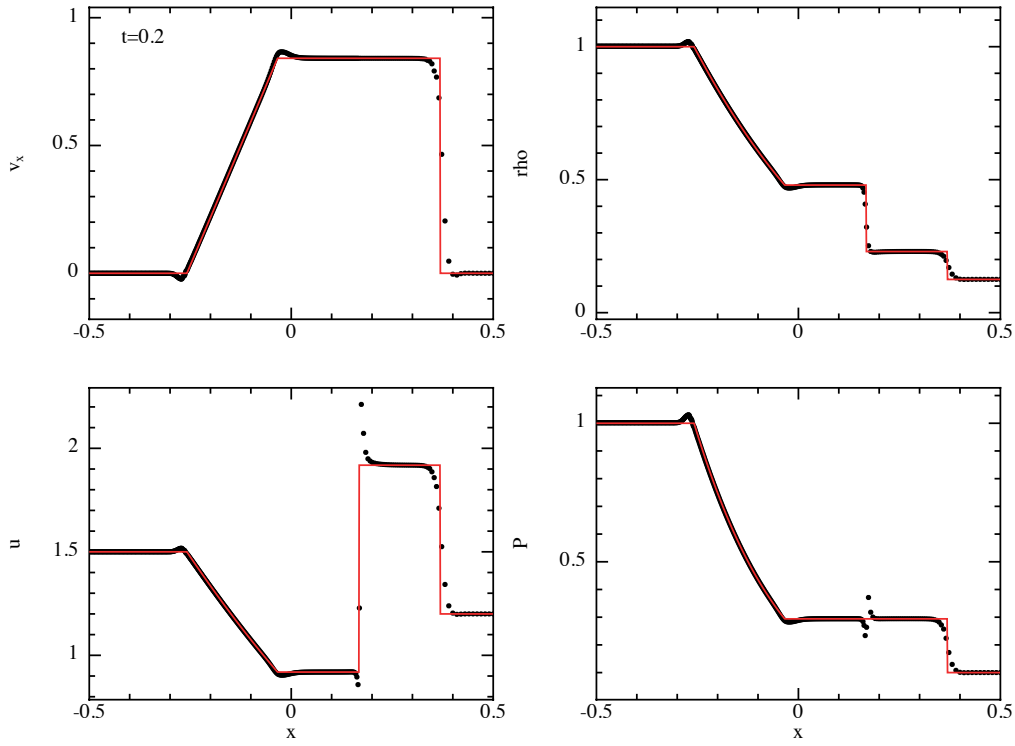

Figure 2.4: As in Figure 2.3 but with no artificial conductivity (i.e. $\alpha_u = 0$). A sharp spike (or 'blip') is present in the thermal energy and pressure at the contact discontinuity ($x \approx 1.8$).

2.1.6 Evolving entropy

It is sometimes useful to evolve an entropy variable instead of e or u (Springel and Hernquist, 2002). Assuming an ideal gas equation of state $P = K(s)\rho^\gamma$, where γ is the adiabatic index and K is a function that depends on entropy, we can derive the very simple entropy evolution equation

$$\frac{dK}{dt} = \frac{\gamma - 1}{\rho^{\gamma-1}}\left(\frac{du}{dt} - \frac{P}{\rho^2}\frac{d\rho}{dt}\right), \tag{2.36}$$

$$= 0. \tag{2.37}$$

From the first law of thermodynamics (Eq. 2.15) K is related to the specific entropy s via

$$T\frac{ds}{dt} = \frac{\rho^{\gamma-1}}{\gamma - 1}\frac{dK}{dt}, \tag{2.38}$$

where T is the gas temperature. In the absence of dissipation the discrete form is also zero ($dK_a/dt = 0$), since the discrete term in brackets cancel exactly. i.e.

$$\frac{du_a}{dt} - \frac{P_a}{\rho_a}\frac{d\rho_a}{dt} = 0. \tag{2.39}$$

With dissipation however, the discrete entropy equation is

$$\frac{dK_a}{dt} = \frac{\gamma - 1}{\rho_a^{\gamma-1}}\left.\frac{du_a}{dt}\right|_{\rm diss}. \tag{2.40}$$

Note that the dissipative term is designed such that the total entropy S always increases. In other words

$$\frac{dS}{dt} = \sum_a m_a \frac{ds_a}{dt} \geq 0. \tag{2.41}$$

2.1.7 Time integration – Leapfrog

Since the SPH equations conserve energy and momentum it is desirable to use a time integration scheme when evolving Equations 2.17 and 2.23 that also conserves energy and momentum.

The Leapfrog integrator in 'velocity-Verlet' form (Verlet, 1967) is used by numerous astrophysical SPH codes (e.g. Wadsley et al., 2004; Springel, 2005; Price et al., 2018), because it is symplectic (conserves angular momentum) and is time-reversible (has no drift in the energy error). This makes it particularly useful in ensuring the long term stability of orbital dynamics, which other common integrators (such as Runge-Kutta) do not guarantee (see Figure 2.5).

The implementation in PHANTOM is given by

$$\mathbf{r}^{n+1} = \mathbf{r}^n + \Delta t\mathbf{v}^n + \frac{1}{2}\Delta t\mathbf{a}^n \tag{2.42}$$

$$\mathbf{v}^* = \mathbf{v}^n + \Delta t\mathbf{a}^n \tag{2.43}$$

$$\mathbf{a}^{n+1} = \mathbf{a}(\mathbf{r}^{n+1}, \mathbf{v}^*) \tag{2.44}$$

$$\mathbf{v}^{n+1} = \mathbf{v}^* + \frac{1}{2}\Delta t\left[\mathbf{a}^{n+1} - \mathbf{a}^n\right], \tag{2.45}$$

where the index n refers to the time step number and $\mathbf{a} \equiv d\mathbf{v}/dt$. Different to the standard Leapfrog 'velocity-Verlet' integrator, the implementation above has a predictor and corrector step

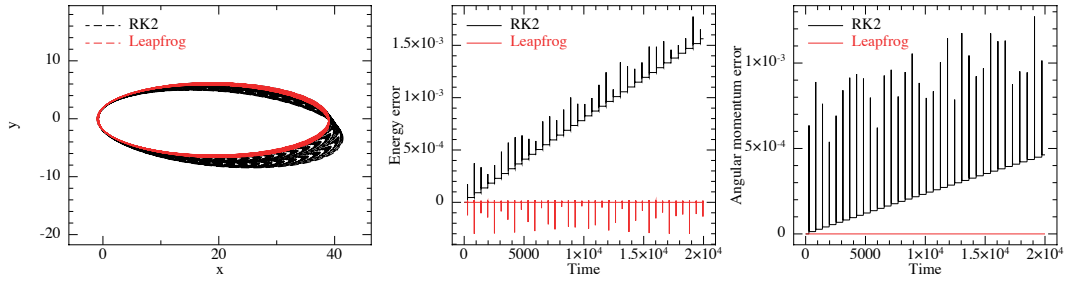

Figure 2.5: Comparison of the long term stability of Leapfrog and RK2 when integrating a highly eccentric orbit in a point mass potential. The orbit is shown on the *left*, the energy conservation in the *middle* and the angular momentum conservation on the *right*. With Leapfrog there is no long term drift in the energy, and angular momentum is conserved to machine precision. RK2 has a drift in both the energy and angular momentum.

(Eq. 2.43 and 2.45). This is to account for the fact that the acceleration has a velocity dependence from the artificial viscosity terms.

In practice, the error in the predictor step is checked after each time step according to

$$\frac{|\mathbf{v}^{n+1} - \mathbf{v}^*|}{|\mathbf{v}^{\rm mag}|} < 10^{-2}, \tag{2.46}$$

where $\mathbf{v}^{\rm mag}$ is the mean velocity on the particles, and the iteration is repeated if this condition is not met.

2.2 Relativistic fluid dynamics

Much of the above (Section 2.1) is also relevant to relativistic SPH. We leave a detailed discussion to Chapter 3 and simply introduce the relevant equations here for reference, and for comparison with their non-relativistic counterparts. A detailed derivation can also be found in Monaghan and Price (2001). We follow the Einstein summation convention, where repeated indices are assumed to be summed over, except for a and b, which are reserved for particle labels. Greek indices range from 0 through 3, while Latin indices range from 1 through 3.

In relativity, fluid elements move through a curved spacetime that is characterised by the metric tensor $g_{\mu\nu}$. The motion of each fluid element is described by its four velocity

$$U^\mu \equiv \frac{{\rm d}x^\mu}{{\rm d}\tau}, \tag{2.47}$$

where x^μ is the spacetime coordinate of the fluid element, and τ is its proper time. The local conservation of energy-momentum is given by

$$(T^{\mu\nu})_{;\mu} = 0, \tag{2.48}$$

where the semi-colon represents a covariant derivative, and

$$T^{\mu\nu} = (\rho + \rho u + P)U^\mu U^\nu + P g^{\mu\nu}, \tag{2.49}$$

is the stress-energy tensor for an ideal fluid. The conservation of rest mass corresponds to

$$(\rho U^\mu)_{;\mu} = 0. \tag{2.50}$$

2.2.1 Continuum equations

Together, Equations 2.48 and 2.50 are a compact representation of the relativistic fluid equations, which can be expanded into Lagrangian form to give

$$\frac{\mathrm{d}\rho^*}{\mathrm{d}t} = -\rho^* \frac{\partial v^i}{\partial x^i}, \tag{2.51}$$

$$\frac{\mathrm{d}p_i}{\mathrm{d}t} = -\frac{1}{\rho^*}\frac{\partial(\sqrt{-g}P)}{\partial x^i} + \frac{\sqrt{-g}\,T^{\mu\nu}}{2\rho^*}\frac{\partial g_{\mu\nu}}{\partial x^i}, \tag{2.52}$$

$$\frac{\mathrm{d}e}{\mathrm{d}t} = -\frac{1}{\rho^*}\frac{\partial(\sqrt{-g}Pv^i)}{\partial x^i} - \frac{\sqrt{-g}\,T^{\mu\nu}}{2\rho^*}\frac{\partial g_{\mu\nu}}{\partial t}. \tag{2.53}$$

Here, ρ^*, p_i and e are the conserved density, conserved momentum and conserved specific energy, respectively, and are given by

$$\rho^* = \sqrt{-g}\rho\, U^0, \tag{2.54}$$

$$p_i = U^0\left(1 + u + \frac{P}{\rho}\right) g_{i\mu}v^\mu, \tag{2.55}$$

$$e = U^0\left[\left(1 + u + \frac{P}{\rho}\right) g_{i\mu}v^\mu v^i - (1+u)g_{\mu\nu}v^\mu v^\nu\right], \tag{2.56}$$

where g is the determinant of the metric tensor and $U^0 = (-g_{\mu\nu}v^\mu v^\nu)^{-1/2}$ is the temporal component of the four velocity (see Chapter 3).

The form of Equations 2.51, 2.52 and 2.53 are very similar to their non-relativistic counterparts in Equations 2.1, 2.2 and 2.3. The main differences are the new conserved variables on the left hand side, the spatial derivatives involving the determinant of the metric, and most importantly, the additional terms in the momentum and energy equations involving derivatives of the metric. These terms can be thought of as 'external forces' arising from the curvature of spacetime.

2.2.2 Computing density

Following the same logic as in Section 2.1.2, we can also write the relativistic equivalent of the SPH density as

$$\rho^*_a = \sum_b m_b W_{ab}(h_b). \tag{2.57}$$

Note however that the left hand side is ρ^* and not ρ, because the former is the conserved variable, i.e. $\int \rho^* dV = M_{\rm tot}$.

2.2.3 Equations of motion

Equations 2.51, 2.52 and 2.53 can also be derived from a Lagrangian using the Euler-Lagrange equations. The Lagrangian for a perfect fluid in relativity is given by (Fock, 1964)

$$L = -\int T^{\mu\nu}U_\mu U_\nu \sqrt{-g}dV, \tag{2.58}$$

which for a perfect fluid becomes

$$L = -\int \rho\,(1+u)\sqrt{-g}dV, \tag{2.59}$$

$$= -\int \frac{\rho^*}{U^0}(1+u)dV. \tag{2.60}$$

Note that $\rho^* = \sqrt{-g}\rho U^0$ is a function of both position and velocity, while u is a function of ρ, which is only a function of position.

To obtain the discrete counterparts of the continuum equations (Equations 2.51, 2.52 and 2.53), we discretise Equation 2.60 by mass (i.e. a constant number of baryons per SPH particle):

$$L = -\sum_b \frac{m_b}{U_b^0}(1+u_b). \tag{2.61}$$

From the Euler-Lagrange equations

$$\frac{d}{dt}\left(\frac{\partial L}{\partial v^i}\right) - \frac{\partial L}{\partial x^i} = 0, \tag{2.62}$$

we can identify the canonical momentum per unit mass

$$p_i^a = \frac{1}{m_a}\frac{\partial L}{\partial v_a^i} = \left[U^0\left(1+u+\frac{P}{\rho}\right)g_{i\mu}v^\mu)\right]_a, \tag{2.63}$$

and can arrive at the discrete momentum equation given by

$$\frac{\mathrm{d}p_i^a}{\mathrm{d}t} = -\sum_b m_b\left[\frac{\sqrt{-g_a}P_a}{\Omega_a\rho_a^{*2}}\frac{\partial W_{ab}(h_a)}{\partial x^i} + \frac{\sqrt{-g_b}P_b}{\Omega_b\rho_b^{*2}}\frac{\partial W_{ab}(h_b)}{\partial x^i}\right] + \left[\frac{\sqrt{-g}\,T^{\mu\nu}}{2\rho^*}\frac{\partial g_{\mu\nu}}{\partial x^i}\right]_a. \tag{2.64}$$

2.2.4 Conservation properties and energy equation

As in Section 2.1.4, we can again construct the Hamiltonian

$$H = \sum_a v_a^i\frac{\partial L}{\partial v_a^i} - L, \tag{2.65}$$

$$= \sum_a m_a U_a^0\left[\left(1+u_a+\frac{P_a}{\rho_a}\right)g_{i\mu}v^iv^\mu + \frac{1+u_a}{U_a^0}\right] \tag{2.66}$$

which allows us to derive the energy equation

$$\frac{\mathrm{d}e_a}{\mathrm{d}t} = -\sum_b m_b\left[\frac{\sqrt{-g_a}P_av_b^i}{\Omega_a\rho_a^{*2}}\frac{\partial W_{ab}(h_a)}{\partial x^i} + \frac{\sqrt{-g_b}P_bv_a^i}{\Omega_b\rho_b^{*2}}\frac{\partial W_{ab}(h_b)}{\partial x^i}\right] - \left[\frac{\sqrt{-g}\,T^{\mu\nu}}{2\rho^*}\frac{\partial g_{\mu\nu}}{\partial t}\right]_a, \tag{2.67}$$

since $H = E = \sum_a m_a e_a$. Note that the Hamiltonian above (Eq. 2.66) is non-separable; it cannot be separated into kinetic and potential components. This is important when considering Hamiltonian integrators for evolving the discrete relativistic fluid equations (see Section 3.6).

As in non-relativistic SPH, the conservation properties depend on symmetries in the Lagrangian (Section 2.1.4), which in this case depends on the metric tensor and whether or not its response to the motion of matter is taken into account (i.e. back-reaction). In the case of a flat spacetime, the derivatives of the metric vanish, and Equation 2.64 and 2.67 are effectively the same as their non-relativistic counterparts (Eq. 2.27 and 2.17). It can then readily be shown, in the same manner as in non-relativistic SPH, that energy, linear momentum and angular momentum are conserved.

In the case of the Schwarzschild and Kerr metric (the spacetime surrounding non-rotating and rotating black holes), the time derivative of the metric is zero, which means that energy is conserved as previously. The Schwarzschild metric also conserves angular momentum, and the Kerr metric conserves the component of angular momentum in the direction of the black hole's spin. However, since the spatial derivatives of the metric are non-zero in both cases, linear momentum is not necessarily conserved. If the metric is kept fixed, then the black hole's centre of mass cannot move in response to the motion of matter around it, meaning that linear momentum will not be conserved. Accounting for this requires more complicated techniques, such as numerical relativity, which is beyond the scope of this work.

Chapter 3

General Relativistic Smoothed Particle Hydrodynamics

We present a method for general relativistic smoothed particle hydrodynamics (GRSPH), based on an entropy-conservative form of the general relativistic hydrodynamic equations for a perfect fluid. We aim to replace approximate treatments of general relativity in current SPH simulations of tidal disruption events and accretion discs. We develop an improved shock capturing formulation that distinguishes between shock viscosity and conductivity in relativity. We also describe a new Hamiltonian time integration algorithm for relativistic orbital dynamics and GRSPH. Our method correctly captures both Einstein and spin-induced precession around black holes. We benchmark our scheme in 1D and 3D against mildly and ultra-relativistic shock tubes, exact solutions for epicyclic and vertical oscillation frequencies, and Bondi accretion. We assume fixed background metrics (Minkowski, Schwarzschild and Kerr in Cartesian Boyer-Lindquist coordinates) but the method lays the foundation for future direct coupling with numerical relativity.

3.1 Introduction

Urgent motivation for relativistic hydrodynamics simulations arises from the coincident detection of an electromagnetic afterglow (Abbott et al., 2017b) alongside the first detection of gravitational waves from a binary neutron star merger (Abbott et al., 2017a). The coming decade should bring hundreds more such events as the Advanced Laser Interferometer Gravitational-Wave Observatory (LIGO) reaches design sensitivity (Abbott et al., 2017a).

Smoothed particle hydrodynamics (SPH) (Gingold and Monaghan, 1977; Lucy, 1977; Rosswog, 2009; Price, 2012) is perfectly suited for neutron star merger simulations because there is no preferred geometry, resolution follows mass, and it avoids the limitations imposed by a background density floor (e.g. Oechslin et al., 2002). The main limitation of SPH in relativistic hydrodynamics to date is the approximate treatment of general relativity (Metzger, 2017).

Further motivation for a public GRSPH code comes from i) the race to find electromagnetic counterparts to binary black hole mergers detected by Advanced LIGO and the forthcoming Laser Interferometer Space Antenna (e.g. Armitage and Natarajan, 2002; Milosavljević and Phinney, 2005; Cerioli et al., 2016); ii) disc formation in tidal disruption events (e.g. Hayasaki et al., 2013, 2016; Bonnerot et al., 2016; Tejeda et al., 2017); iii) the recently discovered phenomena of 'tearing' in warped discs around spinning black holes (e.g. Nixon et al., 2012; Nealon et al., 2015)

and the possible relation to state transitions and quasi periodic oscillations (Nixon and Salvesen, 2014); iv) forthcoming observations from the Event Horizon Telescope (Akiyama et al., 2017); and v) the need for relativistic SPH simulations of pulsar winds (Okazaki et al., 2011).

Kheyfets et al. (1990) were the first to derive relativistic SPH equations, followed by Mann (1991) and Laguna et al. (1993). However, their formulations were not in conservative form and had difficulty handling shocks in even mildly relativistic flows. Conservative forms of the relativistic SPH equations were derived by Chow and Monaghan (1997) (hereafter CM97); Siegler and Riffert (2000); Monaghan and Price (2001); Rosswog (2010a) and Rosswog (2010b) for both special and general relativity, but their applications to date have been limited to special relativity. Other recent studies have instead used post-Newtonian approximations within standard SPH codes to account for relativistic effects in fluid flows around black holes (e.g. Tejeda and Rosswog, 2013; Nealon et al., 2015; Bonnerot et al., 2016; Hayasaki et al., 2016). SPH applications to fluid flows in strong self-gravity assume conformal flatness (e.g. Oechslin et al., 2002; Faber et al., 2004; Bauswein et al., 2010) but these papers do not include standardised tests in fixed metrics. Most recently, Tejeda et al. (2017) applied GRSPH to tidal disruption events, but also showed only limited standardised tests of their method.

Our goal in this paper is to present a detailed description of a fully general relativistic SPH code, able to perform hydrodynamic simulations in any given fixed background metric, with the potential to be applied to dynamically evolving metrics. Our requirements for a modern GRSPH code include being able to capture relativistic shocks, a precise and accurate treatment of orbital dynamics, and the ability to work in Kerr geometry. To this end, we derive an improved shock capturing method and a new Hamiltonian time integration algorithm suitable for GRSPH and relativistic orbital dynamics. We describe our complete method and its implementation in depth, before showing the results of various benchmark tests. We implement our method in PHANTOM (Price et al., 2018), a publicly available SPH code.

3.2 Relativistic hydrodynamics

We follow Monaghan and Price (2001) who obtained the equations of general relativistic smoothed particle hydrodynamics from a Lagrangian. In the following, Greek indices are summed over (0,1,2,3) while Latin indices are summed over (1,2,3). The subscripts a and b are reserved for particle labels.

3.2.1 Definitions

The four velocity of a fluid at a given spacetime coordinate x^μ is given by

$$U^\mu = \frac{\mathrm{d}x^\mu}{\mathrm{d}\tau}, \tag{3.1}$$

where τ is the proper time, and $x^\mu \equiv (t, x^i)$. The coordinate velocity v^μ is defined with respect to the coordinate time t such that

$$v^\mu \equiv \frac{\mathrm{d}x^\mu}{\mathrm{d}t} = \frac{U^\mu}{U^0}, \tag{3.2}$$

where from the normalisation condition $U^\mu U_\mu = -1$ we have

$$U^0 \equiv \frac{\mathrm{d}t}{\mathrm{d}\tau} = \frac{1}{\sqrt{-g_{\mu\nu}v^\mu v^\nu}}. \tag{3.3}$$

We assume standard relativistic units where $c = G = 1$ and a metric signature (−,+,+,+).

3.2.2 Conserved variables

The conserved density, momentum and energy are respectively

$$\rho^* = \sqrt{-g}\rho U^0, \tag{3.4}$$
$$p_i = U^0 w g_{i\mu} v^\mu, \tag{3.5}$$
$$e = U^0 \left[w g_{i\mu} v^\mu v^i - (1+u) g_{\mu\nu} v^\mu v^\nu \right], \tag{3.6}$$

where g is the determinant of the covariant metric $g_{\mu\nu}$ and we use w to denote the specific enthalpy

$$w = 1 + u + \frac{P}{\rho}. \tag{3.7}$$

The specific internal energy, pressure, and density in the rest frame of the fluid are denoted by u, P and ρ, respectively. Equivalently, given a $3+1$ decomposition of the metric (Arnowitt et al., 2008) we can express the conserved quantities as

$$\rho^* = \sqrt{\gamma}\,\Gamma\rho, \tag{3.8}$$
$$p_i = w\Gamma V_i, \tag{3.9}$$
$$e = p_i v^i + \frac{\alpha(1+u)}{\Gamma}, \tag{3.10}$$

where $\Gamma = \left(1 - V^i V_i\right)^{-1/2}$ is the generalised Lorentz factor, and $V^i = \left(v^i + \beta^i\right)/\alpha$ is the fluid velocity in the frame of a local Eulerian observer. The lapse function, shift vector, and spatial three-metric (α, β_i, γ_{ij}) are related to the four-metric $ds^2 = g_{\mu\nu}\mathrm{d}x^\mu \mathrm{d}x^\nu$ via

$$ds^2 = -\alpha^2 \mathrm{d}t^2 + \gamma_{ij}(\mathrm{d}x^i + \beta^i \mathrm{d}t)(\mathrm{d}x^j + \beta^j \mathrm{d}t). \tag{3.11}$$

Spatial vectors can then have their indices raised and lowered by the three-metric, e.g. $v^i v_i = \gamma_{ij} v^i v^j = \gamma^{ij} v_i v_j$. We note that γ is the determinant of γ_{ij}, and that Equation 3.10 can be written alternatively in terms of the enthalpy and pressure as

$$e = w\Gamma\left(\alpha - V^i \beta_i\right) - \frac{\alpha P}{\Gamma\rho}. \tag{3.12}$$

3.2.3 Equations of relativistic hydrodynamics

From Monaghan and Price (2001), the equations of relativistic hydrodynamics in Lagrangian conservative form, assuming an ideal fluid, are given by

$$\frac{\mathrm{d}\rho^*}{\mathrm{d}t} = -\rho^* \frac{\partial v^i}{\partial x^i}, \tag{3.13}$$
$$\frac{\mathrm{d}p_i}{\mathrm{d}t} = -\frac{1}{\rho^*}\frac{\partial(\sqrt{-g}P)}{\partial x^i} + f_i, \tag{3.14}$$
$$\frac{\mathrm{d}e}{\mathrm{d}t} = -\frac{1}{\rho^*}\frac{\partial(\sqrt{-g}Pv^i)}{\partial x^i} + \Lambda, \tag{3.15}$$

where the source terms containing derivatives of the metric are defined according to

$$f_i \equiv \frac{\sqrt{-g}}{2\rho^*}\left(T^{\mu\nu}\frac{\partial g_{\mu\nu}}{\partial x^i}\right), \tag{3.16}$$

$$\Lambda \equiv -\frac{\sqrt{-g}}{2\rho^*}\left(T^{\mu\nu}\frac{\partial g_{\mu\nu}}{\partial t}\right). \tag{3.17}$$

For an ideal fluid the stress-energy tensor is given by

$$T^{\mu\nu} = (\rho + \rho u + P)U^\mu U^\nu + P g^{\mu\nu}, \tag{3.18}$$

$$= \rho w (U^0)^2 v^\mu v^\nu + P g^{\mu\nu}. \tag{3.19}$$

Thus, the term required to compute the source terms is

$$\frac{\sqrt{-g}\,T^{\mu\nu}}{2\rho^*} = \frac{1}{2}\left[wU^0 v^\mu v^\nu + \frac{P g^{\mu\nu}}{\rho\, U^0}\right]. \tag{3.20}$$

We close the equation set with the ideal gas equation of state

$$P = (\gamma_{\rm ad} - 1)\,\rho u, \tag{3.21}$$

where $\gamma_{\rm ad}$ is the adiabatic index. For our calculations we assume an ideal atomic gas, $\gamma_{\rm ad} = 5/3$. The internal energy u can be related to the gas temperature T through the ideal gas law

$$P = \frac{\rho k_{\rm B} T}{\mu m_{\rm H}}, \tag{3.22}$$

where $k_{\rm B}$ is Boltzmann's constant, μ is the mean molecular weight, and $m_{\rm H}$ is the mass of a Hydrogen atom.

3.3 SPH Equations of relativistic hydrodynamics

The discrete form of Equations 3.13, 3.14, and 3.15 in the absence of dissipation, are given respectively by (e.g. Siegler and Riffert, 2000; Monaghan and Price, 2001; Rosswog, 2010a)

$$\frac{{\rm d}\rho_a^*}{{\rm d}t} = \frac{1}{\Omega_a}\sum_b m_b (v_a^i - v_b^i)\frac{\partial W_{ab}(h_a)}{\partial x^i}, \tag{3.23}$$

$$\frac{{\rm d}p_i^a}{{\rm d}t} = -\sum_b m_b \left[\frac{\sqrt{-g_a}P_a}{\Omega_a \rho_a^{*2}}\frac{\partial W_{ab}(h_a)}{\partial x^i} + \frac{\sqrt{-g_b}P_b}{\Omega_b \rho_b^{*2}}\frac{\partial W_{ab}(h_b)}{\partial x^i}\right] + f_i^a, \tag{3.24}$$

$$\frac{{\rm d}e_a}{{\rm d}t} = -\sum_b m_b \left[\frac{\sqrt{-g_a}P_a v_b^i}{\Omega_a \rho_a^{*2}}\frac{\partial W_{ab}(h_a)}{\partial x^i} + \frac{\sqrt{-g_b}P_b v_a^i}{\Omega_b \rho_b^{*2}}\frac{\partial W_{ab}(h_b)}{\partial x^i}\right] + \Lambda_a, \tag{3.25}$$

where W_{ab} is the interpolating kernel, h_a is the smoothing length, and Ω_a is a term related to the gradient of the smoothing length given by (Monaghan, 2002; Springel and Hernquist, 2002)

$$\Omega_a = 1 - \frac{\partial h_a}{\partial \rho_a^*}\sum_b m_b \frac{\partial W_{ab}(h_a)}{\partial h_a}. \tag{3.26}$$

The conserved density can also be computed directly via

$$\rho_a^* = \sum_b m_b W_{ab}(h_a). \tag{3.27}$$

We choose to compute ρ^* by summation, rather than by integration of Equation 3.23. Given equal mass particles, the smoothing length is adapted by simultaneously solving 3.27 and

$$h_a = h_{\rm fac}\left(\frac{m_a}{\rho_a^*}\right)^{1/d}, \tag{3.28}$$

where d is the number of dimensions, and $h_{\rm fac}$ is a numerical parameter specifying the smoothing length in terms of the mean particle spacing. The term required in 3.26 is then

$$\frac{\partial h_a}{\partial \rho_a^*} = -\frac{1}{d}\frac{h_a}{\rho_a^*}. \tag{3.29}$$

For details on solving 3.27 and 3.28 simultaneously we refer the reader to Price and Monaghan (2007).

3.3.1 Interpolating kernel

We use a kernel in the form

$$W_{ab}(h_a) = W(h_a, L_{ab}) \equiv \frac{C_{\rm norm}}{{h_a}^d} f(q), \tag{3.30}$$

where L_{ab} is the inter-particle spacing, $C_{\rm norm}$ is a normalisation constant, and $q = L_{ab}/h_a$. The standard choice for the dimensionless function $f(q)$ in SPH is the cubic spline. With $h_{\rm fac} = 1.2$ this results in 57.9 neighbours per particle on average in 3D. In general, more accurate results can be obtained by using a smoother spline such as the quintic, given by

$$f(q) = \begin{cases} (3-q)^5 - 6(2-q)^5 + 15(1-q)^5, & 0 \le q < 1, \\ (3-q)^5 - 6(2-q)^5, & 1 \le q < 2, \\ (3-q)^5, & 2 \le q < 3, \\ 0, & q \ge 3, \end{cases} \tag{3.31}$$

for which $C_{\rm norm} = [1/120, 1/(120\pi)]$ in 1D and 3D. This comes at the cost of a greater number of neighbours per particle; 113 on average in 3D when $h_{\rm fac} = 1$. For consistency, we choose to use the quintic spline everywhere, however the cubic spline gives satisfactory results also. The neighbour finding procedure in more than one dimension is non trivial. We employ a kd-tree for this process, the details of which can be found in the PHANTOM paper, Price et al. (2018) (see their section 2.1.7).

For the inter-particle spacing L_{ab} we assume local flatness and thus use the Euclidean distance. We define this distance in Cartesian coordinates as

$$L_{ab} \equiv \sqrt{\eta_{ij} r_{ab}^i r_{ab}^j}, \tag{3.32}$$

where η_{ij} is the spatial part of the Minkowski metric, and $r_{ab}^i \equiv x_a^i - x_b^i$ is the line of sight vector pointing from particle a to particle b also in Cartesian coordinates. Computing the kernel

and its derivative is then identical to what is done in standard non-relativistic SPH. In Cartesian coordinates, since η_{ij} is a constant, we can write the kernel derivative as

$$\frac{\partial W_{ab}(h_a)}{\partial x^i} = N_i \, F_{ab}(h_a), \tag{3.33}$$

where $F_{ab} \leq 0$ is the scalar part of the kernel gradient. We define the line of sight projection operator,

$$N_i \equiv \eta_{ij} \hat{r}^j_{ab}, \tag{3.34}$$

where,

$$\hat{r}^i_{ab} = \frac{r^i_{ab}}{L_{ab}}, \tag{3.35}$$

is the line of sight unit vector.

We emphasise that the choice between using the Euclidean distance norm and proper lengths for neighbour distances is arbitrary. Using a different distance metric would simply require a different particle placement to obtain the same conserved density. So this choice reflects how one wishes to place particles to resolve features in the spacetime. We argue that the Euclidean norm is the most natural choice because the particle placement is independent of the metric. For example, a uniformly spaced lattice of particles produces a constant ρ^*. Using the proper length for neighbour distances would require stretching or squeezing the initial particle arrangement to compensate for the determinant of the metric in the volume element. It would also require computing a path integral in the given metric between all neighbouring particles.

One possible advantage to using the proper distance would be that smoothing spheres would never cross the event horizon. That is, neighbours close to the event horizon would become infinitely distant. However, it is no longer obvious how to set up the particles to achieve a particular ρ^* in this case, and using different metrics would require different particle setups. We demonstrate in Section 3.8.4 that using the Euclidean distance norm indeed produces the correct conserved densities close to the black hole so long as the horizon is sufficiently well resolved.

3.4 Shock capturing

It is necessary to introduce dissipative terms in order to capture shocks. As in CM97 and Monaghan (1997) the construction of the dissipative terms is motivated by approximate Riemann solvers used by finite volume codes (Martí et al., 1991). To demonstrate this, consider the equation set written in conservative form and in one spatial dimension (for simplicity)

$$\frac{\partial \mathbf{u}}{\partial t} + \frac{\partial \mathbf{F}}{\partial x} = 0, \tag{3.36}$$

where $\mathbf{u} = (\rho^*, p_i, e)$ is the vector of conservative variables and $\mathbf{F}(\mathbf{u})$ is the flux. Finite volume schemes require computing the numerical flux between adjacent states $\mathbf{u}_\mathrm{L}, \mathbf{u}_\mathrm{R}$. The simplest approach utilises the 'local Lax-Friedrichs' or 'Rusanov' flux given by

$$\mathbf{F}(\mathbf{u}_\mathrm{L}, \mathbf{u}_\mathrm{R}) = \frac{1}{2}\left[\mathbf{F}(\mathbf{u}_\mathrm{L}) + \mathbf{F}(\mathbf{u}_\mathrm{R})\right] - \frac{v_\mathrm{sig}}{2}\left(\mathbf{u}_\mathrm{R} - \mathbf{u}_\mathrm{L}\right) \tag{3.37}$$

where v_sig is the maximum characteristic speed. Importantly, the dissipative term (proportional to v_sig) acts on jumps in the conservative variables.

Although the exact relationship between the dissipation introduced in approximate Riemann solvers and physical dissipation terms is unclear in relativity, since the correct way to formulate viscosity and heat conduction in relativistic hydrodynamics is not well understood (e.g. Andersson and Comer, 2007), the approach used above is standard in GRMHD codes (e.g. Martí et al., 1991; Gammie et al., 2003; Zhang and MacFadyen, 2006).

Our SPH shock capturing formulation is based on approximate Riemann solvers, following CM97. If one considers adjacent particles in SPH as left and right states, an appropriate form of the dissipative terms requires a jump in the conservative variables and a maximum signal speed $v_{\rm sig}$ between the particles. CM97 proposed corresponding terms in the momentum and energy equations in SPH given by

$$\left.\frac{\mathrm{d}p_i^a}{\mathrm{d}t}\right|_{\rm diss} = \alpha_{\rm AV} \sum_b \frac{m_b}{\bar{\rho}^*_{ab}} v_{\rm sig} \left(p^*_a - p^*_b\right) \frac{\partial W_{ab}(h_a)}{\partial x^i}, \tag{3.38}$$

$$\left.\frac{\mathrm{d}e_a}{\mathrm{d}t}\right|_{\rm diss} = \alpha_{\rm AV} \sum_b \frac{m_b}{\bar{\rho}^*_{ab}} v_{\rm sig} \left(e^*_a - e^*_b\right) F_{ab}(h_a), \tag{3.39}$$

where p^* and e^* are computed using only velocities along the line of sight (v^*), $\bar{\rho}^*_{ab} = (\rho^*_a + \rho^*_b)/2$, and $\alpha_{\rm AV} \simeq 1$ is a numerical parameter to control the amount of dissipation.

The problem with the formulation given by CM97 is that, while they proved that the entropy increase was positive definite for cold gas ($w = 1$), we found this to no longer be the case when the enthalpy differs from unity. To remedy this, we adapted their formulation to *not* use the full jump in momentum or total energy

$$p^*_a - p^*_b = w_a \Gamma^*_a V^*_a - w_b \Gamma^*_b V^*_b, \tag{3.40}$$

$$e^*_a - e^*_b = p^*_a v^*_a - p^*_b v^*_b + \frac{\alpha_a(1+u_a)}{\Gamma^*_a} - \frac{\alpha_b(1+u_b)}{\Gamma^*_b}, \tag{3.41}$$

where starred quantities again denote the use of the line of sight velocity v^*. Instead, in order to have a positive definite change in entropy we use a jump only in the 'kinetic terms', $\Gamma^*_a V^*_a - \Gamma^*_b V^*_b$. For the momentum equation we multiply the corresponding term by an average enthalpy, and for the energy equation we multiply by an average of the term wv, in order to recover the correct dimensions. That is, we define

$$p^*_a - p^*_b \equiv \overline{w}_{ab} \left(\Gamma^*_a V^*_a - \Gamma^*_b V^*_b\right), \tag{3.42}$$

where $\overline{w}_{ab}$ denotes a suitable average of w over particles a and b.

A second problem with the CM97 formulation was that it does not distinguish between viscosity and conductivity. This leads to over-smoothing of contact discontinuities (see Section 3.8.1). Showing how to split the dissipation into viscosity and conductivity in relativity is non-trivial. We demonstrate in Section 3.8.1 and Appendix A.1.1 that the relevant splitting can be achieved by defining the energy jump in two parts as follows

$$e^*_a - e^*_b \equiv \underbrace{\overline{w}_{ab} \bar{v}^*_{ab} \left(\Gamma^*_a V^*_a - \Gamma^*_b V^*_b\right)}_{\text{viscosity}} + \underbrace{\left(\frac{\alpha_a u_a}{\Gamma_a} - \frac{\alpha_b u_b}{\Gamma_b}\right)}_{\text{conductivity}}, \tag{3.43}$$

where $\bar{v}^*_{ab}$ denotes an average of v^* over particles a and b (see below). This is equivalent to defining a relativistic thermal energy

$$\tilde{u} \equiv \frac{\alpha u}{\Gamma}. \tag{3.44}$$

Our third change is more cosmetic. Rather than using separate averages for $\overline{w}_{ab}$ and $\bar{v}^*_{ab}$, we average them along with the density, signal speed and kernel derivative in the manner of Price and Federrath (2010) following the non-relativistic terms in PHANTOM (Price et al., 2018). That is, we write the viscosity as a $P + q$ term in the momentum and energy equations.

3.4.1 Artificial viscosity

Equations 3.24 and 3.25 with our dissipation become

$$\frac{\mathrm{d}p^a_i}{\mathrm{d}t} = -\sum_b m_b \left[\frac{(P_a + q_a)}{\rho^{*2}_a} D^a_i + \frac{(P_b + q_b)}{\rho^{*2}_b} D^b_i\right] + f^a_i, \tag{3.45}$$

$$\frac{\mathrm{d}e_a}{\mathrm{d}t} = -\sum_b m_b \left[\frac{(P_a + q_a)}{\rho^{*2}_a} v^i_b D^a_i + \frac{(P_b + q_b)}{\rho^{*2}_b} v^i_a D^b_i\right] + \Pi^a_{\mathrm{cond}} + \Lambda_a, \tag{3.46}$$

where q_a and q_b encapsulate the artificial viscosity, and Π^a_{cond} the artificial conductivity. For added simplicity in notation, we have defined

$$D^a_i \equiv \frac{\sqrt{-g_a}}{\Omega_a} \frac{\partial W_{ab}(h_a)}{\partial x^i}, \tag{3.47}$$

$$D^b_i \equiv \frac{\sqrt{-g_b}}{\Omega_b} \frac{\partial W_{ab}(h_b)}{\partial x^i}. \tag{3.48}$$

Our artificial viscosity terms are

$$q_a = -\frac{1}{2}\alpha_{\mathrm{AV}} \rho^*_a v_{\mathrm{sig},a} w_a \left(\Gamma^*_a V^*_a - \Gamma^*_b V^*_b\right), \tag{3.49}$$

$$q_b = -\frac{1}{2}\alpha_{\mathrm{AV}} \rho^*_b v_{\mathrm{sig},b} w_b \left(\Gamma^*_a V^*_a - \Gamma^*_b V^*_b\right), \tag{3.50}$$

and involve a fluid velocity that is along the line of sight between particles, similar to CM97, i.e.

$$V^*_a = N_i V^i_a, \tag{3.51}$$

$$\Gamma^*_a = \frac{1}{\sqrt{1 - V^{*2}_a}}. \tag{3.52}$$

If the particles are separating, $N_i(v^i_a - v^i_b) \geq 0$, we set $q_a = q_b = 0$.

3.4.2 Artificial conductivity

Our artificial conductivity term is given by

$$\Pi_{\mathrm{cond}} = \frac{\alpha_u}{2} \sum_b m_b \left(\tilde{u}_a - \tilde{u}_b\right) \left(\frac{v^u_{\mathrm{sig},a} G_a}{\rho^*_a} + \frac{v^u_{\mathrm{sig},b} G_b}{\rho^*_b}\right), \tag{3.53}$$

where again for simplicity we define

$$G_a \equiv \frac{\sqrt{-g_a}}{\Omega_a} \frac{\partial W_{ab}(h_a)}{\partial x^i} \hat{r}^i_{ab} = D^a_i \hat{r}^i_{ab}, \tag{3.54}$$

which in Cartesian coordinates is

$$G_a = \frac{\sqrt{-g_a}}{\Omega_a} F_{ab}(h_a). \tag{3.55}$$

Note that the terms $\alpha_{\rm AV}$ and α_u allow us to control the amount of artificial viscosity and conductivity, respectively. These should not be confused with α_a and α_b which are the lapse functions at the positions of particles a and b.

3.4.3 Signal speed — viscosity

When constructing an approximation for the maximum signal speed in the artificial viscosity, $v_{\rm sig}$, we impose two requirements. First, the signal speed must not exceed the speed of light. Second, the signal speed should reduce to the form used in standard SPH codes in the non-relativistic limit, namely

$$v_{{\rm sig},a} = \alpha_{\rm AV} c_{{\rm s},a} + \beta_{\rm AV} \left| \mathbf{v}_{ab} \cdot \hat{\mathbf{r}}_{ab} \right| , \tag{3.56}$$

where $c_{\rm s}$ is the sound speed, $\mathbf{v}_{ab} = \mathbf{v}_a - \mathbf{v}_b$ is the relative velocity, and $\hat{\mathbf{r}}_{ab}$ is the unit vector along the line of sight. The numerical parameters $[\alpha_{\rm AV}, \beta_{\rm AV}]$ control the amount of dissipation. Most importantly, the signal speed should involve a relative velocity between the particles to avoid excessive dissipation when there is a bulk velocity and individual particle speeds are high.

Because of these requirements, we do not use the signal speeds proposed by CM97, since in some of their formulations the maximum signal speed may exceed the speed of light. We also do not use the signal speed proposed by Rosswog (2010a), based on the eigenvalues of the Euler equations. Their formulation, although limited by the speed of light, involves the absolute velocity of the SPH particles. This means their viscosity term is no longer Galilean invariant. We therefore require a signal speed that uses only the relative velocity between particles. To this end, we propose a signal speed given by

$$v_{{\rm sig},a} = \frac{c_{{\rm s},a} + |V^*_{ab}|}{1 + c_{{\rm s},a} \left| V^*_{ab} \right|}, \tag{3.57}$$

where the relative velocity between particles, considered along the line of sight, is defined as

$$V^*_{ab} \equiv \frac{V^*_a - V^*_b}{1 - V^*_a V^*_b}, \tag{3.58}$$

and the relativistic sound speed is given by

$$c_{\rm s} = \sqrt{\frac{P \gamma_{\rm ad}}{\rho w}}. \tag{3.59}$$

We use the velocities in the frame of the local Eulerian observer V^i rather than the coordinate velocities v^i, since only V^i is a physical velocity that is limited by the speed of light, that is $|V_i V^i| \leq 1$. The coordinate velocity, on the other hand, is not strictly under the same restriction.

3.4.4 Signal speed — conductivity

For simplicity one may assume the same signal speed for both viscosity and conductivity. That is, $v^u_{\rm sig} = v_{\rm sig}$. In general however, one should use different speeds since the conductivity is

mainly required at contact discontinuities which travel at a different speed to the shock. Price (2008) proposed using a signal speed based on the relative pressure jump, designed to eliminate the pressure blip at contact discontinuities. We generalise this to the relativistic case using

$$v^u_{\rm sig} = \min\left(1, \sqrt{\frac{|P_a - P_b|}{\overline{w}\overline{\rho}_{ab}}}\right). \tag{3.60}$$

For cases where equilibrium pressure gradients exist due to other physics (e.g. gravity) it is better to simply use the relative speeds (Price, 2008; Wadsley et al., 2008), giving

$$v^u_{\rm sig} = |V^*_{ab}|, \tag{3.61}$$

when generalised to the relativistic case. In the non-relativistic limit, both eq. 3.60 and 3.61 reduce to the non-relativistic implementation in PHANTOM (Price et al., 2018), where the choice is based on whether or not gravity and/or external forces are used.

The main advantage of the above signal speeds is that conductivity becomes $\mathcal{O}(h^2)$ in the numerical code, rather than first order. For most of the tests in this paper, we simply use $v^u_{\rm sig} = v_{\rm sig}$ with a reduced value of α_u. In section 3.8.1 we demonstrate the benefit of using Eq. 3.61 in the case of a self-gravitating, oscillating polytrope.

3.5 Evolving entropy

Instead of the total specific energy e, we evolve an entropy variable (cf. Springel and Hernquist 2002) in order to guarantee positivity of the thermal energy. We define

$$K \equiv \frac{P}{\rho^{\gamma_{\rm ad}}}. \tag{3.62}$$

Taking the time derivative and using Equation 3.21 we find

$$\frac{{\rm d}K}{{\rm d}t} = (\gamma_{\rm ad} - 1)\,\rho^{1-\gamma_{\rm ad}}\left(\frac{{\rm d}u}{{\rm d}t} - \frac{P}{\rho^2}\frac{{\rm d}\rho}{{\rm d}t}\right), \tag{3.63}$$

$$= \frac{K}{u}\left(\frac{{\rm d}u}{{\rm d}t} - \frac{P}{\rho^2}\frac{{\rm d}\rho}{{\rm d}t}\right). \tag{3.64}$$

Comparing this to the second law of thermodynamics

$$T\frac{{\rm d}s}{{\rm d}t} = \frac{{\rm d}u}{{\rm d}t} - \frac{P}{\rho^2}\frac{{\rm d}\rho}{{\rm d}t}, \tag{3.65}$$

we see that in the absence of dissipation

$$\frac{{\rm d}K}{{\rm d}t} = 0. \tag{3.66}$$

Furthermore, using Equation 3.22, K can be related to the specific entropy s

$$\frac{1}{K}\frac{{\rm d}K}{{\rm d}t} = (\gamma_{\rm ad} - 1)\,\frac{\mu m_{\rm H}}{k_{\rm B}}\frac{{\rm d}s}{{\rm d}t}. \tag{3.67}$$

More generally, we can rewrite Equation 3.64 in terms of time derivatives of the conserved variables (ρ^*, p_i, e), giving

$$\frac{{\rm d}K}{{\rm d}t} = \frac{U^0 K}{u}\left[\left(\frac{{\rm d}e}{{\rm d}t} - \Lambda\right) - v^i\left(\frac{{\rm d}p_i}{{\rm d}t} - f_i\right) - \frac{P\sqrt{-g}}{\rho^{*2}}\frac{{\rm d}\rho^*}{{\rm d}t}\right], \tag{3.68}$$

which, after substituting Equations 3.23, 3.45, and 3.46, gives

$$\frac{\mathrm{d}K_a}{\mathrm{d}t} = \frac{U_a^0 K_a}{u_a}\left(\Pi^a_{\mathrm{cond}} + \sum_b m_b \frac{q_a\left(v_a^i - v_b^i\right)}{\rho_a^{*2}} D_i^a\right). \tag{3.69}$$

Thus, the evolution of K is governed purely by the dissipative terms. An important distinction between SPH and finite-volume schemes is that when evolving K, energy remains exactly conserved (to the accuracy of the time integration algorithm), since Eq 3.68 holds to round-off error. In Appendix A.1 we demonstrate that Eq. 3.69 is always positive (for special relativity) thus ensuring that entropy always increases.

3.6 Time Integration

Relativistic hydrodynamics, in the absence of dissipation, forms a Hamiltonian system where the canonical variables are the positions x^i and momenta p_i. Ideally therefore one should use a geometric integrator that preserves the Hamiltonian properties. The main complication is that the Hamiltonian is non-separable — it cannot be separated into kinetic, thermal, and potential energy terms.

3.6.1 Generalised leapfrog method

Leimkuhler and Reich (2005) suggest the 'generalised leapfrog method' for the symplectic integration of Hamilton's equations with a non-separable Hamiltonian. With p_i and x^i as the conjugate variables, their scheme is given by

$$p_i^{n+\frac{1}{2}} = p_i^n + \frac{\Delta t}{2}\frac{\mathrm{d}p_i}{\mathrm{d}t}(p_i^{n+\frac{1}{2}}, x^{i,n}), \tag{3.70}$$

$$x^{i,n+1} = x^{i,n} + \frac{\Delta t}{2}\left[\frac{\mathrm{d}x^i}{\mathrm{d}t}(p_i^{n+\frac{1}{2}}, x^{i,n}) + \frac{\mathrm{d}x^i}{\mathrm{d}t}(p_i^{n+\frac{1}{2}}, x^{i,n+1})\right], \tag{3.71}$$

$$p_i^{n+1} = p_i^{n+\frac{1}{2}} + \frac{\Delta t}{2}\frac{\mathrm{d}p_i}{\mathrm{d}t}(p_i^{n+\frac{1}{2}}, x^{i,n+1}), \tag{3.72}$$

where the superscripts $n+m$ refer to quantities evaluated at times $t^{n+m} = t^n + m\Delta t$. It may be seen that this reduces to the standard Kick-Drift-Kick leapfrog scheme when $v^i \equiv p_i$ and when the acceleration $\mathrm{d}p_i/\mathrm{d}t$ depends only on position. It is also time-reversible and symplectic. However, a general property of geometric integrators for non-separable Hamiltonians is that they are implicit in one or more of the steps (e.g. Yoshida, 1993). In the above integrator this occurs in the first 'Kick' step, where the momentum at the half step appears on both sides of the equation, and in the 'Drift' step where the position at the full step appears on both sides.

3.6.2 Alternative generalised leapfrog method

For GRSPH, evaluating $\mathrm{d}p_i/\mathrm{d}t(p_i, x^i)$ means performing a sum over particles, while evaluation of $\mathrm{d}x^i/\mathrm{d}t(p_i, x^i)$ means performing a primitive variable solve (see Section 3.7) which can be performed independently for each particle. Hence the previous integrator would require two calls to the summation routines, since $\mathrm{d}p_i/\mathrm{d}t$ used in the second Kick step is different from the one required for the subsequent first Kick step at the start of the next timestep. For this reason we

propose a similar integrator where the symmetrisation occurs in the drift step. Our alternative integrator is given by

$$p_i^{n+\frac{1}{2}} = p_i^n + \frac{\Delta t}{2}\frac{\mathrm{d}p_i}{\mathrm{d}t}(p_i^n, x^{i,n}), \tag{3.73}$$

$$x^{i,n+1} = x^{i,n} + \frac{\Delta t}{2}\left[\frac{\mathrm{d}x^i}{\mathrm{d}t}(p_i^{n+\frac{1}{2}}, x^{i,n}) + \frac{\mathrm{d}x^i}{\mathrm{d}t}(p_i^{n+\frac{1}{2}}, x^{i,n+1})\right], \tag{3.74}$$

$$p_i^{n+1} = p_i^{n+\frac{1}{2}} + \frac{\Delta t}{2}\frac{\mathrm{d}p_i}{\mathrm{d}t}(p_i^{n+1}, x^{i,n+1}). \tag{3.75}$$

This integrator retains the time symmetry of the previous integrator, however it does not exactly conserve angular momentum. The difference is that the implicit steps are now in the Drift step, as previously, and in the second Kick step. Importantly, the derivative of the momentum used in the second Kick step is the same as that used at the beginning of the subsequent step, meaning that it can be re-used. The integrator is also easier to start, because it merely requires an evaluation of the momentum derivative involving position and momentum from the initial conditions.

The implicit solve in the Drift step (in the position derivative) involves only the primitive variable solver, so is independent for each particle. The implicit nature of the second Kick step (in the momentum derivative) in principle involves multiple loops over neighbouring particles, but this is similar to our existing approach to dealing with viscosity and other velocity-dependent terms in non-relativistic SPH (see below). With a good prediction of p_i^{n+1}, only one call to the summation routines is required.

3.6.3 Hybrid leapfrog, and implementation in GRSPH

Since our modified integrator does not exactly conserve angular momentum, we implement a hybrid of the two algorithms in order to retain the benefits of both. Taking an operator splitting approach similar to that of the reversible reference system propagator algorithm (RESPA) derived by Tuckerman et al. (1992) we split the acceleration into 'long range' and 'short range' forces (see Price et al. 2018 for an implementation in SPH). In our case, the 'long range' forces are the SPH forces, while the 'short range' forces are the external forces arising from the curvature of the spacetime. These correspond to the pressure gradient term and f_i in the momentum equation, respectively. i.e.

$$f_i^{\mathrm{sph}} \equiv -\frac{1}{\rho^*}\frac{\partial(\sqrt{-g}P)}{\partial x^i}, \tag{3.76}$$

$$f_i^{\mathrm{ext}} \equiv f_i. \tag{3.77}$$

We use the 'long range' forces f_i^{sph} to update the momentum of each particle and use the 'short range' forces f_i^{ext} in updating their positions. Our complete hybrid algorithm is therefore

$$p_i \to p_i + \frac{\Delta t_{\mathrm{sph}}}{2} f_i^{\mathrm{sph}}(p_i, x^i), \tag{3.78}$$

$$\text{substeps}\begin{cases}\tilde{p}_i = p_i + \dfrac{\Delta t_{\text{ext}}}{2} f_i^{\text{ext}}(\tilde{p}_i, x^i), & (3.79)\\ p_i \to \tilde{p}_i, & (3.80)\\ \tilde{x}^i = x^i + \dfrac{\Delta t_{\text{ext}}}{2}\left[v^i(p_i, x^i) + v^i(p_i, \tilde{x}^i)\right], & (3.81)\\ x^i \to \tilde{x}^i, & (3.82)\\ p_i \to p_i + \dfrac{\Delta t_{\text{ext}}}{2} f_i^{\text{ext}}(p_i, x^i), & (3.83)\end{cases}$$

$$\tilde{p}_i = p_i + \frac{\Delta t_{\text{sph}}}{2} f_i^{\text{sph}}(\tilde{p}_i, x^i), \tag{3.84}$$

$$p_i \to \tilde{p}_i, \tag{3.85}$$

where the position update is done over m substeps (indicated by the equations in braces), such that $m = \text{int}(\Delta t_{\text{ext}}/\Delta t_{\text{sph}} + 1)$ and is the minimum over all particles. We denote the updating of a variable by an arrow, some of which first require solving and implicit equation, namely Equations 3.79, 3.81, and 3.84.

The combination of the two algorithms ensures that one of the SPH force calculations can be reused between steps, reducing computational cost, and that angular momentum is conserved in the case where the SPH forces can be neglected. More importantly it ensures that our method is not restricted by the external force timestep, since computing f_i^{ext} is cheap whereas f_i^{sph} is expensive.

It is useful to point out that in the absence of metric gradients the hybrid method reduces to our proposed scheme in section 3.6.2, while for pressureless fluid it reduces to the method of Leimkuhler and Reich (2005) in section 3.6.1.

Evaluating implicit steps

To evaluate Equations 3.79 and 3.81, we employ two first-order predictions which we refer to as p_i^* and $x^{i,*}$. That is, for Eq 3.79 we do

$$p_i^* = p_i + \frac{\Delta t_{\text{ext}}}{2} f_i^{\text{ext}}(p_i, x^i), \tag{3.86}$$

$$\tilde{p}_i = p_i^* + \frac{\Delta t_{\text{ext}}}{2}\left[f_i^{\text{ext}}(p_i^*, x^i) - f_i^{\text{ext}}(p_i, x^i)\right], \tag{3.87}$$

and for evaluating Eq 3.81 we do

$$x^{i,*} = x^i + \Delta t_{\text{ext}} v^i(p_i, x^i), \tag{3.88}$$

$$\tilde{x}^i = x^{i,*} + \frac{\Delta t_{\text{ext}}}{2}\left[v^i(p_i, x^{i,*}) - v^i(p_i, x^i)\right]. \tag{3.89}$$

To complete the implicit step we check that

$$|\tilde{p}_i - p_i^*| < \epsilon_p, \tag{3.90}$$

$$|\tilde{x}^i - x^{i,*}| < \epsilon_x, \tag{3.91}$$

after Equations 3.87 and 3.89, respectively, where ϵ_x and ϵ_p are small tolerances. If these criteria are violated we iterate Equation 3.87 (or Eq. 3.89) by a fresh evaluation of the corresponding

derivative with the updated value, that is, simply replacing p_i^* with $\tilde{p}_i$, and p_i with p_i^* on the right hand side of Eq. 3.87 (and similarly with $x^{i,*}$ and x^i in Eq. 3.89).

Equation 3.84 is evaluated in the same manner as 3.79 but with $f_i^{\rm sph}$ and $\Delta t_{\rm sph}$ instead of $f_i^{\rm ext}$ and $\Delta t_{\rm ext}$. We use the error criterion

$$e = \frac{\max(|\Delta p|^2)}{\mathrm{rms}(|p|)} < \epsilon_p^{\rm sph}, \tag{3.92}$$

where we define $|p| \equiv \sqrt{p_i p_j \eta^{ij}}$ and $\Delta p_i \equiv \tilde{p}_i - p_i^*$, consistent with the implementation of the equivalent implicit step in PHANTOM (cf. Price et al., 2018). The maximum is taken over all the particles in the numerator, while the denominator evaluates the root mean square, also over all the particles.

In general, iterations of Equations 3.79 and 3.81 are cheap, while iterations of Equation 3.84 are expensive, so ϵ_p and ϵ_x can be set arbitrarily small while $\epsilon_p^{\rm sph}$ must allow for an efficient code. By default the tolerance is set to $\epsilon_p^{\rm sph} = 10^{-2}$ in PHANTOM. To try to prevent iterations from occurring, we constrain the timestep by

$$\Delta t = \min\left(\Delta t, \frac{\Delta t}{\sqrt{\max(e)/\epsilon_p^{\rm sph}}}\right), \tag{3.93}$$

since an iteration is as expensive as halving the timestep.

In terms of storage, we require only one position and momenta for each particle, but storage of two derivatives (current and previous) of both v^i and f_i.

3.6.4 Timestep constraint

We adopt the usual stability conditions, namely

$$\Delta t_{\rm sph}^a = \min\left(\frac{C_{\rm C}\, h_a}{\max(v_{{\rm sig},a})}, C_{\rm f}\sqrt{\frac{h_a}{\left|f_a^{\rm sph}\right|}}\right), \tag{3.94}$$

where $C_{\rm C}$ and $C_{\rm f}$ are the usual safety factors, set to 0.3 and 0.25, respectively by default in PHANTOM, the maximum $v_{\rm sig}$ is over neighbours to particle a, and $|f| \equiv \sqrt{f_i f_j \eta^{ij}}$. In our tests we use global timestepping where the global timestep $\Delta t_{\rm sph}$ is set to the minimum value of $\Delta t_a^{\rm sph}$ on the particles, although our scheme is simple to generalise to the case where particles have individual timesteps. The timestep constraint for external force substeps is similarly

$$\Delta t_a^{\rm ext} = C_{\rm f}\sqrt{\frac{h_a}{|f_a^{\rm ext}|}}, \tag{3.95}$$

and the global $\Delta t_{\rm ext}$ is the minimum of $\Delta t_a^{\rm ext}$ on the particles.

3.7 Recovery of primitive variables

Computing the right hand side of Equations 3.23, 3.24, and 3.25 explicitly requires the primitive variables (ρ, u, v^i, P). We must therefore invert the set of equations describing the conserved variables (Eq. 3.8, 3.9, and 3.10) at every timestep. To do this we use the recovery scheme given by Tejeda (2012).

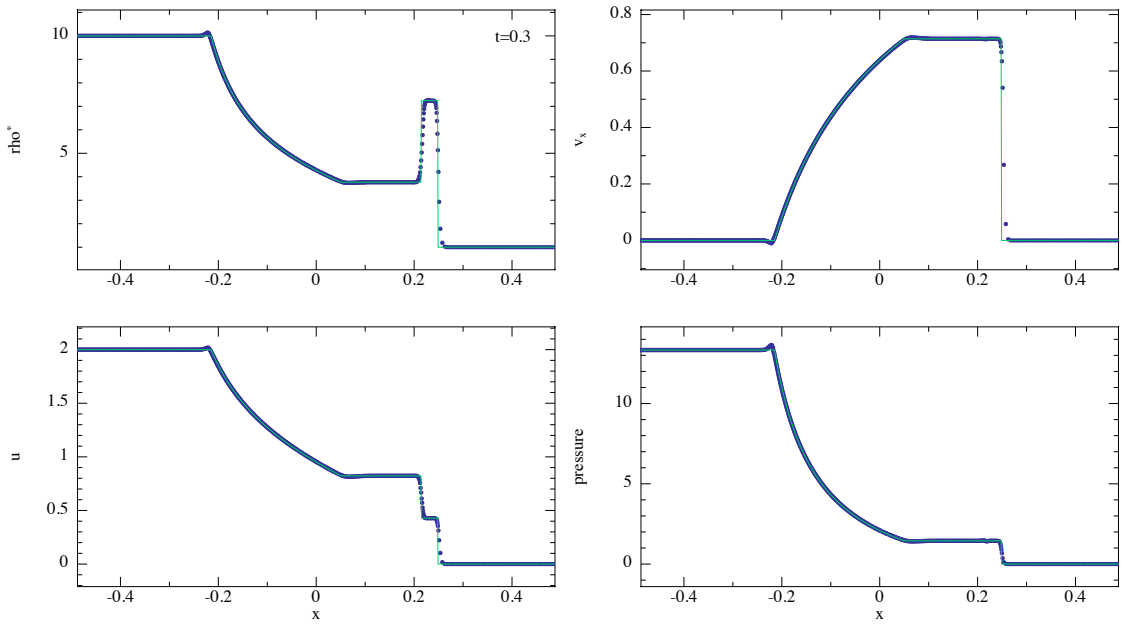

Figure 3.1: Mildly relativistic shock performed in 1D, with artificial conductivity. Blue circles show SPH particles, while green line shows the analytic solution from Martí and Müller (1994). The initial particle spacing to the left of the interface is 0.0005.

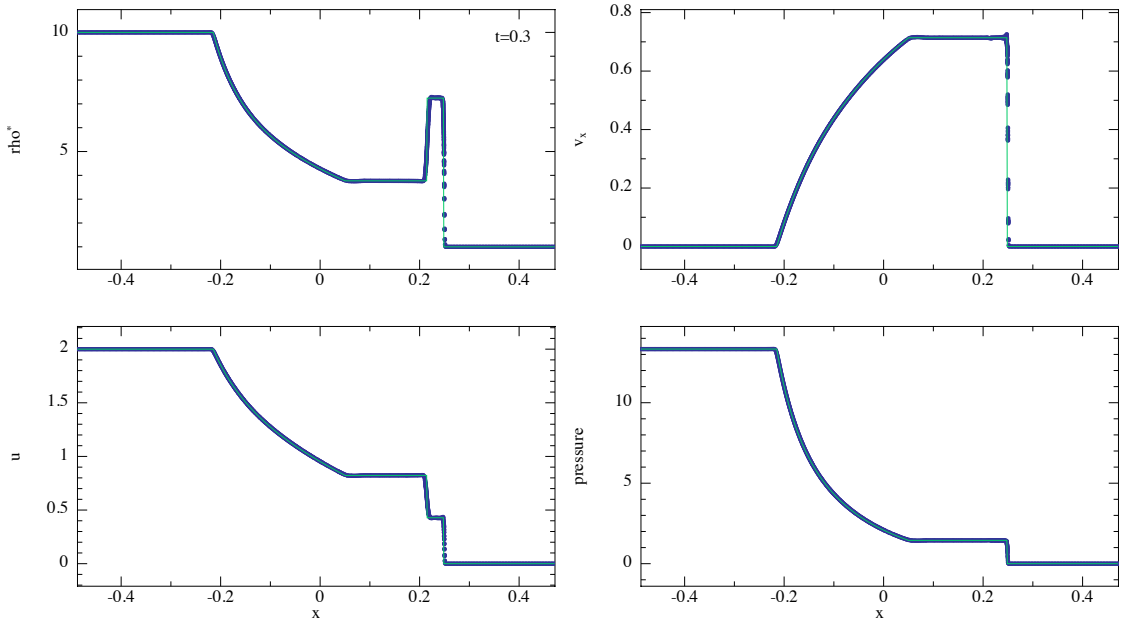

Figure 3.2: As in Figure 3.1 but in 3D. The initial particle spacing to the left of the interface is 0.0005. The solution is similar to that obtained with our 1D code.

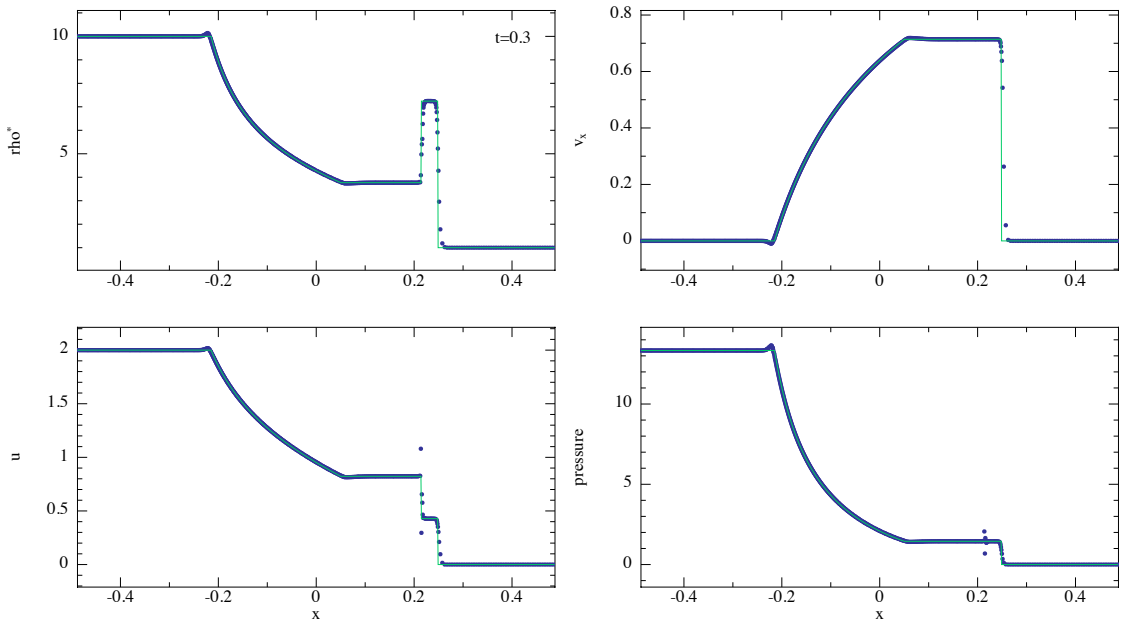

Figure 3.3: Mildly relativistic shock performed in 1D, without artificial conductivity ($\alpha_u = 0$). Blue circles show SPH particles, while green line shows the analytic solution from Martí and Müller (1994). The initial particle spacing to the left of the interface is 0.0005. A 'blip' in the pressure and thermal energy is visible at the contact discontinuity.

1. Use the equation of state to solve for the enthalpy as a function of density and pressure only,
$$w = w(\rho, P). \tag{3.96}$$

2. Express ρ, P and v^i as functions of only w and the conserved variables,
$$\rho(w) = \frac{\rho^*}{\sqrt{\gamma}\,\Gamma(w)}, \tag{3.97}$$
$$P(w) = \frac{\rho^*}{\alpha\sqrt{\gamma}}\left(w\,\Gamma(w)\alpha - e - p_i\beta^i\right), \tag{3.98}$$
$$v_i(w) = \frac{\alpha\, p_i}{w\,\Gamma(w)} - \beta_i, \tag{3.99}$$
where $v_i = \gamma_{ij}\, v^j$, and $\Gamma(w)$ can be calculated from Eq. 3.9 as,
$$\Gamma(w) = \sqrt{1 + \frac{p^i p_i}{w^2}}. \tag{3.100}$$

3. Given Equations 3.97 and 3.98, solve Equation 3.96 for the enthalpy using a standard root-finding algorithm. (See Appendix A.2 for more detail).

4. Compute v_i using Equation 3.99, and raise the index using the three-metric $v^i = \gamma^{ij} v_j$.

3.8 Numerical tests

We split the testing of our numerical method into three stages.

1. First, we developed a dedicated 1D special relativistic SPH code to test the shock capturing terms in section 3.4, and the conservative-to-primitive algorithm in section 3.7. For the time integration in this code we used the standard 2nd order Runge-Kutta method (RK2), with time steps constrained by Equation 3.94). We use RK2 instead of the algorithm described in section 3.6 to show that the particular timestepping algorithm used is not important for shock tube tests.

2. Next, we developed a 3D N-body code to test the force terms involving the metric derivatives f_i. This involved integrating Equation 3.14 with $P = 0$, i.e.

$$\frac{\mathrm{d}p_i}{\mathrm{d}t} = f_i \quad \text{and} \quad \frac{\mathrm{d}x^i}{\mathrm{d}t} = v^i. \tag{3.101}$$

   Although this is equivalent to solving the geodesic equation, it allowed us to test our time integration scheme (section 3.6.3), as well as the conservative-to-primitive algorithm, again, but with more complicated metrics than the Minkowski metric. We implemented the Schwarzschild metric in both spherical and Cartesian coordinates, along with the Kerr metric in Boyer-Lindquist coordinates (both spherical and Cartesian). For this code we used a fixed time step.

3. Finally, after testing individual aspects of our method in the previous two codes, we incorporated them all into PHANTOM, a fully 3-dimensional SPH code (Price et al., 2018). In this code, we implemented the full, hybrid-Leapfrog method for the time integration, as described in section 3.6.3. The timestep is constrained according to Equations 3.93, 3.94, & 3.95.

For SPH simulations we always use equal mass particles, and assume an adiabatic gas with $\gamma_{\rm ad} = 5/3$. For the artificial dissipation we use $\alpha_{\rm AV} = 1$ and $\alpha_u = 0.1$, unless otherwise stated.

We quantify the error in our simulations with the dimensionless L_2 error

$$L_2 = \sqrt{\frac{1}{N \max(y_{\rm exact})} \sum_{i=1}^{N} |y_i - y_{\rm exact}|^2}, \tag{3.102}$$

where N is the number of points and $y_{\rm exact}$ is the exact solution at point i.

3.8.1 Special Relativity

Mildly relativistic shock

In Figures 3.1 & 3.2 we show the results for a mildly relativistic shock in both 1D and 3D, respectively. This is 'Problem 1' in Martí and Müller (2003) with a maximum fluid Lorentz factor of $\Gamma = 1.38$. For the initial conditions, we set

$$[\rho, P] = \begin{cases} [10, \frac{40}{3}] & \text{for } x < 0, \\ [1, 10^{-6}] & \text{for } x > 0. \end{cases} \tag{3.103}$$

The particle spacing to the left of the interface is 0.0005, and 0.005 to the right. For the initial particle arrangement in 3D, we follow Price et al. (2018). We employ a uniform close-packed lattice of $1000 \times 26 \times 26$ particles for $x \in [-0.5, 0]$ and $434 \times 12 \times 12$ particles for $x \in [0, 0.5]$,

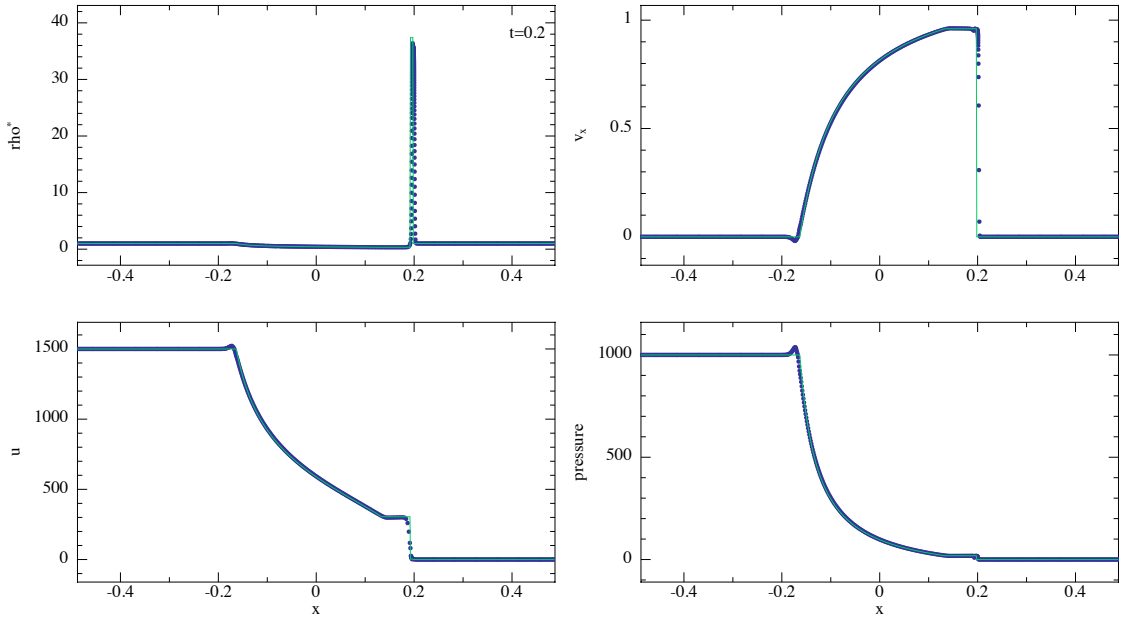

Figure 3.4: Results of the blast wave performed in 1D. Blue circles show SPH particles, while green lines show the analytic solution from Martí and Müller (1994). The initial particle spacing on both sides of the interface is 0.001.

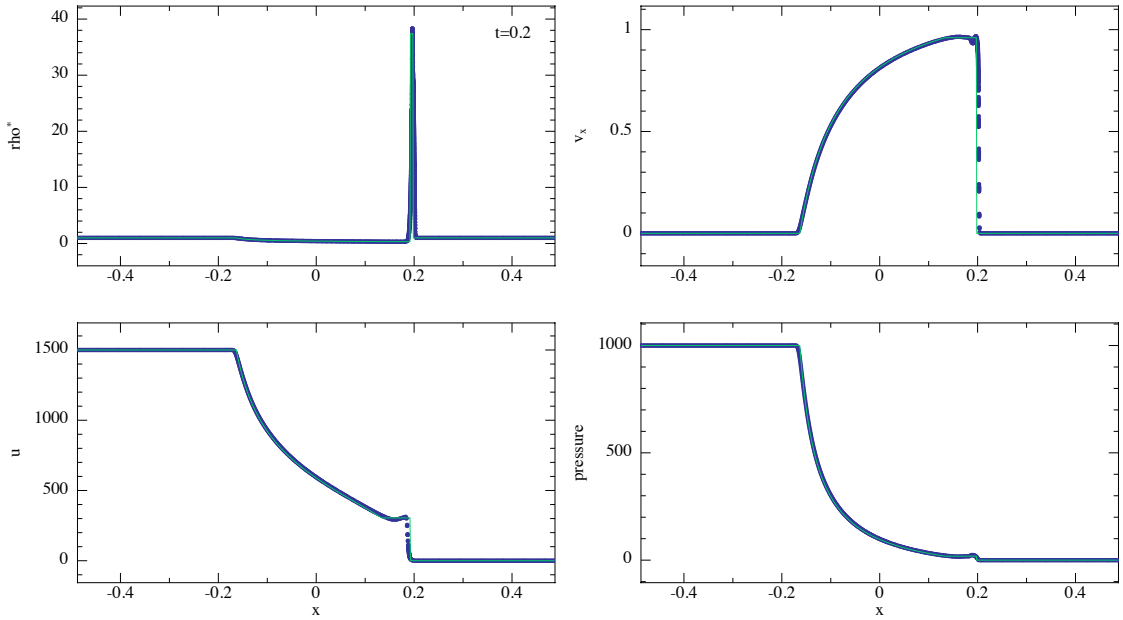

Figure 3.5: As in Figure 3.4 but in 3D. Initial particle spacing is 0.001. According to Martí and Müller (2003) this problem 'is still a challenge for state-of-the-art codes today'. Our use of an entropy variable and positive definite dissipation means our code remains robust and accurate for this problem.

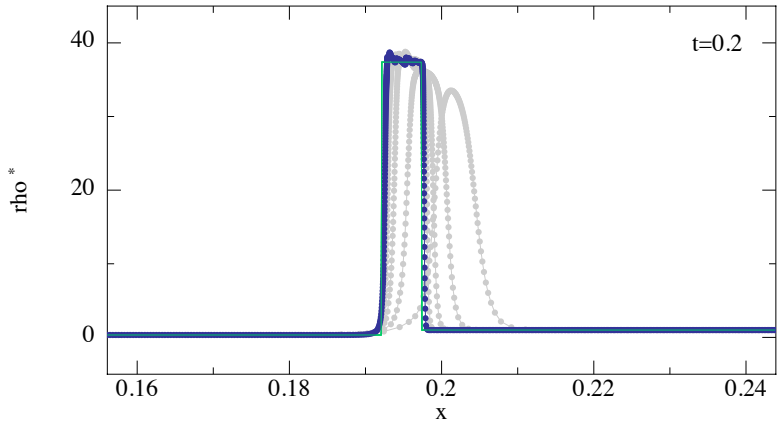

Figure 3.6: Details of the density spike at different resolutions for the blast wave problem in 1D. We show the results of 500, 1000, 2000, 4000, and 8000 particle simulations, going from right to left, beginning with the rightmost peak. This corresponds to initial particle spacings of $2 \times 10^{-3}, 10^{-3}, 5 \times 10^{-4}, 2.5 \times 10^{-4}$, and 1.25×10^{-4}, respectively.

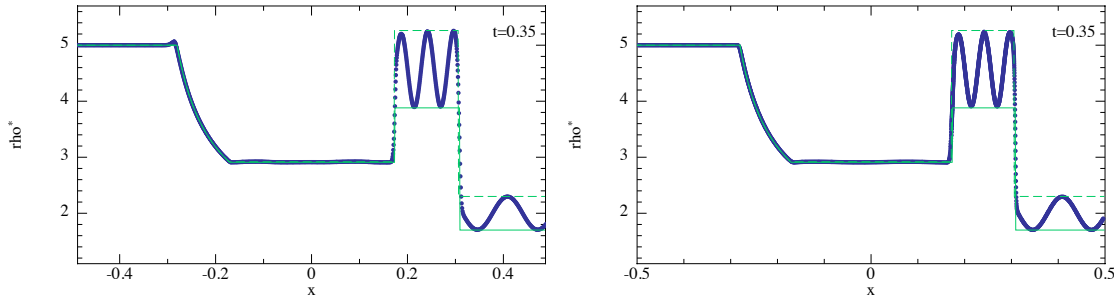

Figure 3.7: Results of the sine wave shocktube performed in 1D (left) and 3D (right). Blue circles show SPH particles, while green lines show the analytic solution for the two density extremes in the sine wave. The initial particle spacing to the left of the interface is 0.0004. The sine wave is accurately advected across the shock front, with no noticeable loss in accuracy.

with periodic boundaries in the y and z directions. Of the four hydrodynamic variables plotted (ρ^*, v^x, u, P), the error is largest in v^x with $L_2 = 4.0 \times 10^{-2}$ in 1D, and $L_2 = 3.2 \times 10^{-2}$ in 3D.

The most noticeable difference between the 1D and 3D simulations is the slight overshoot at the left end of the rarefaction fan $x \approx -0.2$. This is caused by the lack of dissipation applied to the small discontinuity at the end of the rarefaction fan. It can be eliminated in 1D by applying the viscosity term for both approaching and receding particles. In 3D, even with viscosity applied only to approaching particles there is some dissipation applied at this location because the velocity differences are computed more isotropically. The small excess velocity at $x \approx 0.25$ seen in 3D is caused by particles rearranging behind the shock front.

Figure 3.3 shows the same shock but with $\alpha_u = 0$. Without artificial conductivity we find a 'blip' in the pressure profile at the contact discontinuity. The same feature is discussed by Price (2008) and Price (2012) in the context of non-relativistic SPH simulations. In both cases, the 'blip' can be smoothed out by including artificial conductivity. Simulations by CM97 do not contain such a 'blip', but instead display excessive thermal diffusion at the contact discontinuity, since artificial conductivity is included implicitly within their dissipation terms (compare our results to figures 9 and 10 in their paper).

Strong blast

In Figures 3.4 & 3.5 we show the results for a strong blast wave in both 1D and 3D, respectively. This is 'Problem 2' in Martí and Müller (2003) with a maximum fluid Lorentz factor of $\Gamma = 3.6$. We follow the same setup as for the mildly-relativistic shock but with differing initial conditions

$$[\rho, P] = \begin{cases} [1, 1000] & \text{for } x < 0, \\ [1, 10^{-2}] & \text{for } x > 0. \end{cases} \tag{3.104}$$

The particle spacing is 0.001 on both sides of the interface, with $1000 \times 12 \times 12$ particles for the whole domain in 3D. Importantly, we use unsmoothed initial conditions, unlike in CM97 and Rosswog (2010a). We found this was only possible when we evolved the entropy rather than total energy as the conserved variable, otherwise negative pressures could result in the absence of smoothing. The error is again largest in v^x for both cases, with $L_2 = 2.5 \times 10^{-1}$ in 1D and $L_2 = 3.1 \times 10^{-1}$ in 3D. The peak of the density spike is also within 2.7% of the exact solution in both the 1D and 3D simulations. The same differences between 1D and 3D simulations occur as in the previous test, and for the same reasons.

Figure 3.6 shows the details of the density spike at different resolutions. At low resolutions the shock speed is overestimated, consistent with the results of CM97. With 500 particles the centre of the spike is ahead of the exact solution by approximately one spike width. As the resolution is increased, our simulations approach the exact solution.

Sinusoidally perturbed shock

In Figure 3.7 we show the results in 1D and 3D for a shock tube with a sinusoidally perturbed right density state (e.g. Del Zanna and Bucciantini, 2002; Rosswog, 2010a) where the fluid reaches a maximum Lorentz factor of $\Gamma = 1.15$. The initial conditions for this setup are

$$[\rho, P] = \begin{cases} [5,\ 50] & \text{for } x < 0, \\ [2 + 0.3\sin(50x),\ 5] & \text{for } x > 0. \end{cases} \tag{3.105}$$

The particle spacing is 0.0004 on the left side of the interface, and on the right such that the particle masses are the same as on the left. We find that the sine wave perturbation is easily transported across the shock front in both cases, with no noticeable loss in accuracy. The peaks of the propagated sine wave reach the correct levels of the two limiting solutions; to within 1.2% in 1D, and within 1.3% in 3D. The left end of the rarefaction fan in 1D displays an overshoot in the density, for the same reasons as discussed in the previous tests.

Shocks with transverse velocity

We consider two problems where the shock contains a non-zero transverse velocity to the main flow. This is important in relativistic flows since the magnitude of the flow speed is limited by the speed of light, and the transverse velocity is coupled to the evolution of the other hydrodynamic variables through the Lorentz factor.

Figure 3.8 shows our results in 1D for a shocktube with initial conditions given by

$$[\rho, P, v^x, v^y] = \begin{cases} [1, 1000, 0, 0] & \text{for } x < 0, \\ [1, 10^{-2}, 0, 0.99] & \text{for } x > 0. \end{cases} \tag{3.106}$$

The initial particle spacing is 0.0001 on the left side of the interface. Of the four hydrodynamic variables plotted (ρ, v^x, v^y, P), the error is greatest in ρ with $L_2 = 3.7 \times 10^{-2}$, and a 5% overshoot at the contact discontinuity. The fluid has a maximum Lorentz factor of $\Gamma = 7.09$.

A much more challenging test is the shocktube with initial conditions given by

$$[\rho, P, v^x, v^y] = \begin{cases} [1, 1000, 0, 0.9] & \text{for } x < 0, \\ [1, 10^{-2}, 0, 0.9] & \text{for } x > 0. \end{cases} \tag{3.107}$$

As pointed out by Zhang and MacFadyen (2006) this tests requires a 'very high resolution to resolve the complicated structure of the transverse velocity'. Figure 3.9 shows the results for this problem in 1D. We find that this test is particularly challenging since the transverse velocity changes rapidly, requiring very high spatial resolution. The most obvious artefact is a spike in v^y at $x \approx 0.2$. This is also observed in Zhang and MacFadyen (2006) but is worse in SPH since this feature occurs in a low density part of the simulation, where the resolution is lowest. The largest error is in ρ with $L_2 = 4.0 \times 10^{-1}$. The fluid reaches a maximum Lorentz factor of $\Gamma = 44.5$.

3D spherical blast wave

In Figure 3.10 we show the results of a spherically symmetric relativistic blast in 3D, analogous to the non-relativistic Sedov-Taylor blast wave. This is the same problem as done by Del Zanna and Bucciantini (2002) and Zhang and MacFadyen (2006) (see their Figures 8 and 17, respectively).

For the initial conditions we set $640 \times 740 \times 784$ particles on a closepacked lattice within a uniform periodic box $x, y, z \in [-1, 1]$. The density is initially set to $\rho^* = \rho = 1$ everywhere. We inject a sphere of uniform pressure $P_{\text{in}} = 1000$ at the origin with radius $r_0 = 0.4$, and set the pressure outside the sphere to $P_{\text{out}} = 0$. Our setup and resolution is equivalent to Zhang and MacFadyen (2006), however we simulate the whole box $x, y, z \in [-1, 1]$, instead of just the quadrant $x, y, z \in [0, 1]$ which is only possible in spherical symmetry.

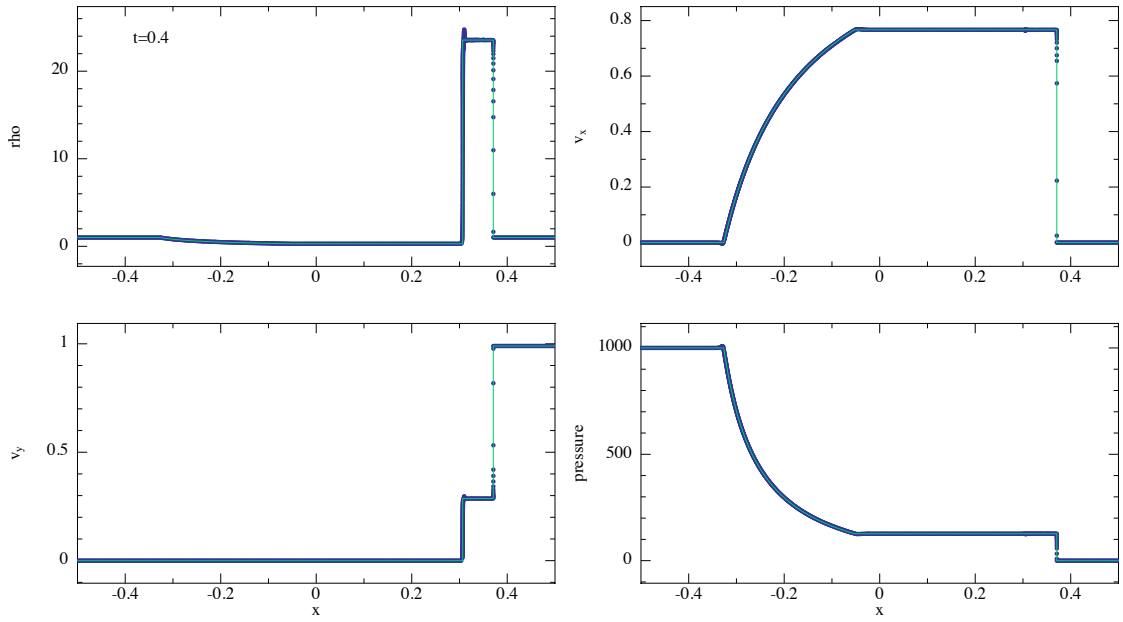

Figure 3.8: Results of the 1D shocktube with initial transverse velocity on the right side of the interface. The initial particle spacing is 0.0001 on the left side of the interface. We find a small overshoot in the density at the contact discontinuity.

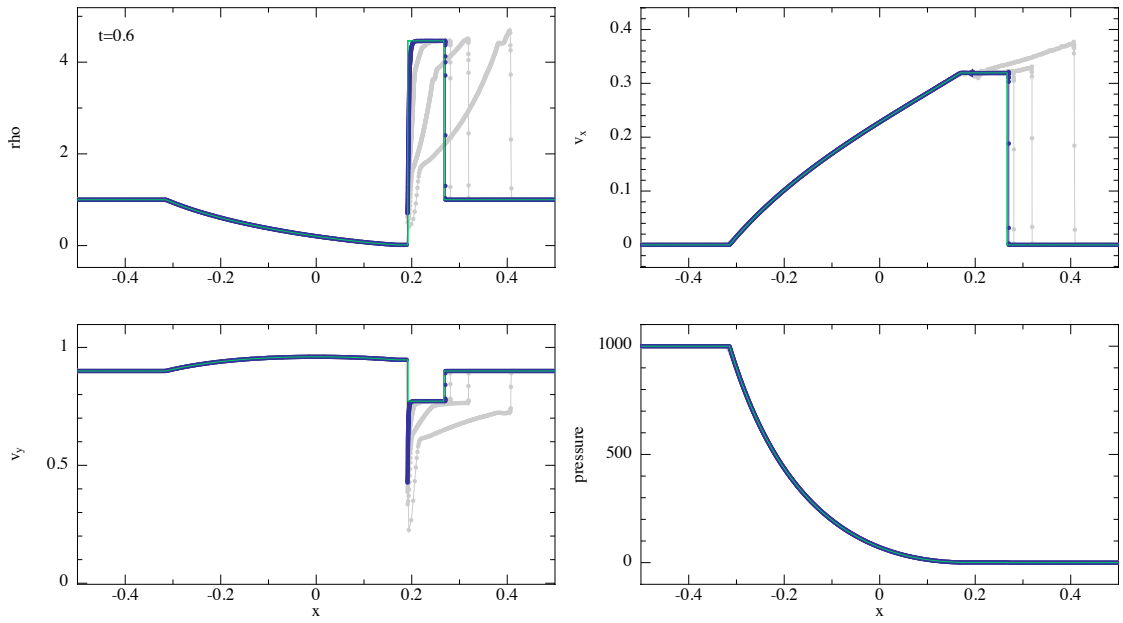

Figure 3.9: Results of the 1D shocktube with initial transverse velocity on both sides of the interface. Simulations with 1000, 4000, and 16000, particles are shown in grey for reference, and the highest resolution simulation of 64000 particles is shown in blue. These resolutions corresponds to initial particle spacings of $1 \times 10^{-3}, 2.5 \times 10^{-4}, 6.25 \times 10^{-5}$, and 1.5625×10^{-5}, respectively. The exact solution given by Giacomazzo and Rezzolla (2006); Martí and Müller (2015) is shown in green. We find a large spike in v^y at the contact discontinuity with even the highest resolution.

Following Chow and Monaghan (1997) and Rosswog (2010a) we slightly smoothed the initial discontinuity in the pressure using

$$P(r) = \frac{P_{\rm in} - P_{\rm out}}{1 + \exp(\frac{r-r_0}{\Delta r})} - P_{\rm out}, \tag{3.108}$$

where for the characteristic transition length Δr we used half the initial particle spacing.

We compare our results to the 1D high resolution results of Zhang and MacFadyen (2006). Our solution shows qualitative agreement with theirs, with the most notable difference being an $\sim 8\%$ increase in the speed of our shock front. There is also a small amount of smoothing at the left end of the rarefaction fan ($x \approx 0.05$), which is present in the 3D simulations of Del Zanna and Bucciantini (2002) and Zhang and MacFadyen (2006). Figure 3.11 shows the (primitive) density slice through the $z = 0$ plane, demonstrating our code's ability to preserve radial symmetry and resolve the structure of the thin shell. The fluid reaches a maximum Lorentz factor of $\Gamma = 19.56$.

Oscillating polytrope

A concern with artificial conductivity (expressed by the referee of this paper) is that it may introduce unwanted side effects. For example, spuriously applied conductivity may seriously disrupt a stellar equilibrium state. To address this concern, Figure 3.12 shows the results of a 3D oscillating polytropic star with Newtonian self-gravity (see Appendix B.2) in the Minkowski metric. The initial conditions are a relaxed star consisting of 65752 $\left(\approx 4\pi 25^3/3\right)$ particles and polytropic equation of state $P(r) = K\rho(r)^{(n+1)/n}$ with $K = 10^{-10}$ and $n = 1.5$ (i.e. $\gamma_{\rm ad} = 5/3$).

To relax the star we apply an additional force to the particles in the momentum equation which depends on the particle velocity (Gingold and Monaghan, 1977)

$$f^i_{\rm damp} = -0.03\, v^i, \tag{3.109}$$

and turn off all dissipative terms. That is, we set $\alpha_{\rm AV} = 0$ and $\alpha_u = 0$. We integrate until $t = 20000$ when all particle motions have been sufficiently damped.

To induce radial oscillations in the star, we perturb the relaxed star profile with a small velocity perturbation

$$v^i(r) = 10^{-4} x^i(r). \tag{3.110}$$

Figure 3.12 compares the results of three different simulations, one with no dissipation, a second with conductivity turned on using $v^u_{\rm sig} = v_{\rm sig}$, and a third using conductivity with $v^u_{\rm sig}$ as in Eq. 3.61.

With no dissipation the amplitude of the stellar oscillation does not decay with time since energy is conserved exactly (black line in both panels). However with $v^u_{\rm sig} = v_{\rm sig}$, the stellar profile slowly becomes disturbed, and the central density increases. The results of the third simulation demonstrate a way to remedy this issue. The signal speed in Eq. 3.61 gives conductivity of $\mathcal{O}(h^2)$, and which vanishes when the star is in hydrostatic equilibrium. This allows us to reproduce the same undamped oscillations as in the dissipation-free simulation.

3.8.2 Orbital dynamics — Schwarzschild Metric

In order to test our ability to perform orbital dynamics accurately, we use the Schwarzschild metric in spherical Schwarzschild coordinates. We confirmed that the same results can be reproduced using the equivalent Cartesian representation (see Appendix A.3.1). We use a black hole mass of $M = 1$ in all simulations.

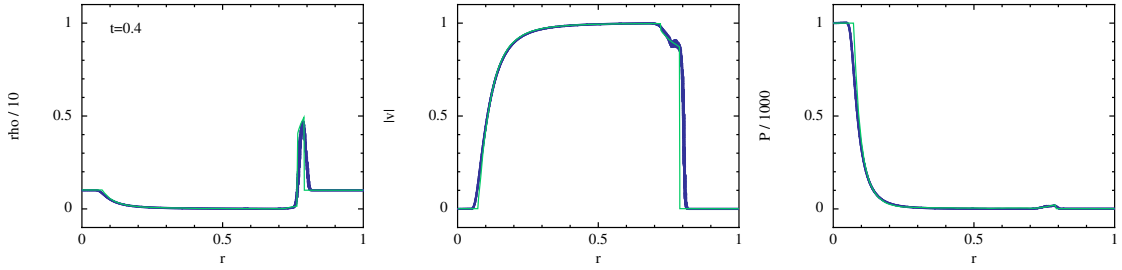

Figure 3.10: Results of the spherical blast wave in 3D with $640 \times 740 \times 784$ particles (blue circles). We compare to the high resolution 1D results of Zhang and MacFadyen (2006) (green line).

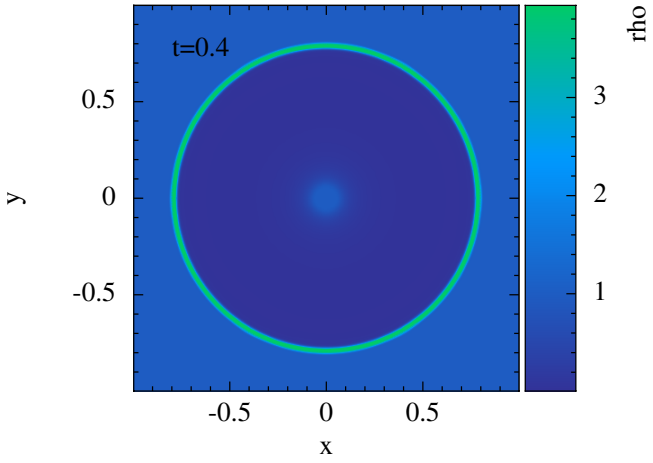

Figure 3.11: Slice through the spherical blast wave in 3D showing the primitive density ρ.

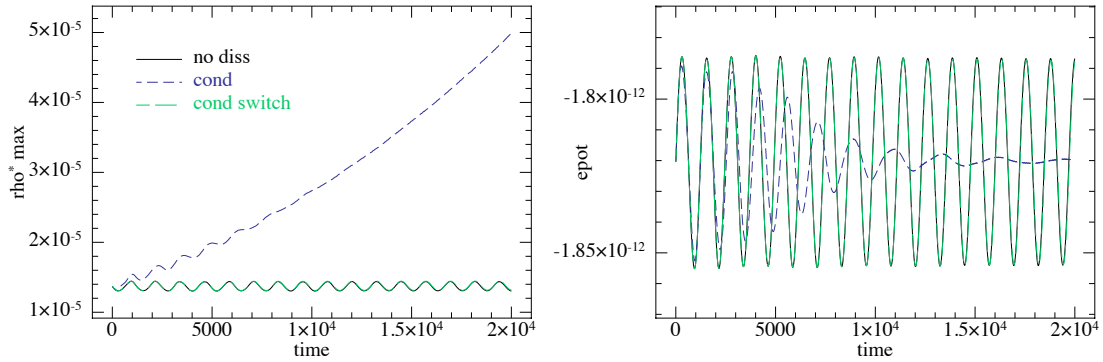

Figure 3.12: Maximum (central) density ρ^* (left) and total gravitational potential energy (right) for the oscillating polytrope. With no dissipation the polytrope oscillates indefinitely about its equilibrium state (black solid line). Using artificial conductivity with the same signal speed as artificial viscosity results in a disturbed stellar profile (blue dot-dashed line). This is remedied by using the signal speed in Eq. 3.61 which switches conductivity off where it is not needed (green dashed line).

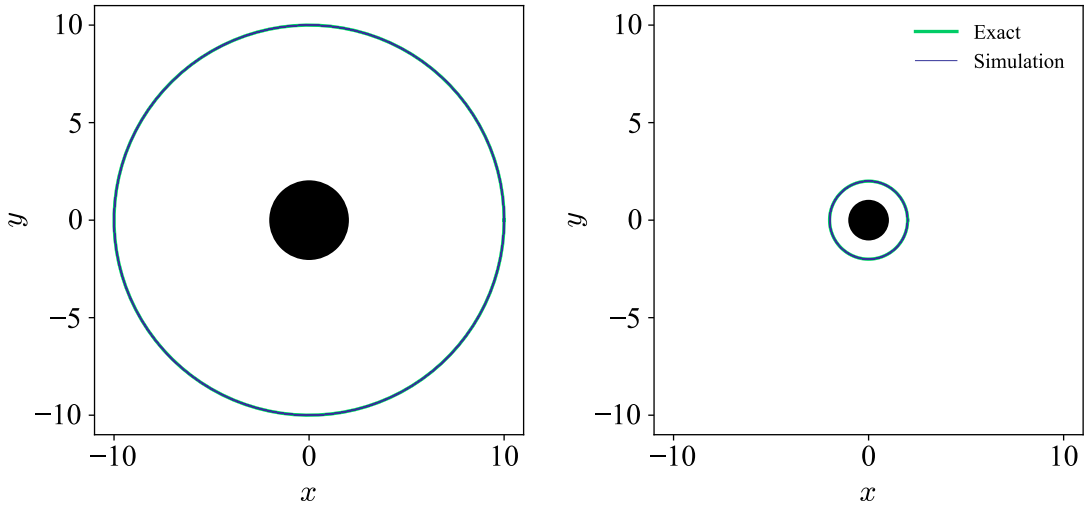

Figure 3.13: Circular orbits computed in the Schwarzschild (left) and Kerr (right) metrics at $r = 10M$ and $r = 2M$, respectively, with central mass $M = 1$. The orbit in the Kerr metric was computed with maximal spin, $a/M = 1$. Orbits are indicated by the blue line, while green lines show the exact orbit. The black holes are represented by the solid black circles i.e. the region interior to the event horizon $r_{\rm h}$. For the Schwarzschild metric, $r_{\rm h} = 2M$, while for the Kerr metric $r_{\rm h} = 1M$ when $a/M = 1$.

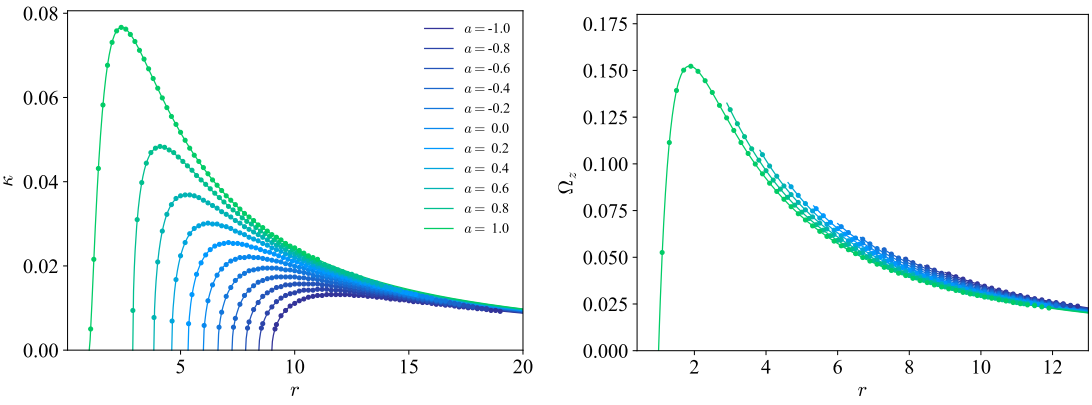

Figure 3.14: Epicyclic frequency (left) and vertical oscillation frequency (right) as a function of radius for $a/M \in [-1, 1]$ shown in steps of 0.2 (spin increasing right to left), showing numerical solution from test particle orbits (points), compared to the exact solution (lines). Central mass is $M = 1$.

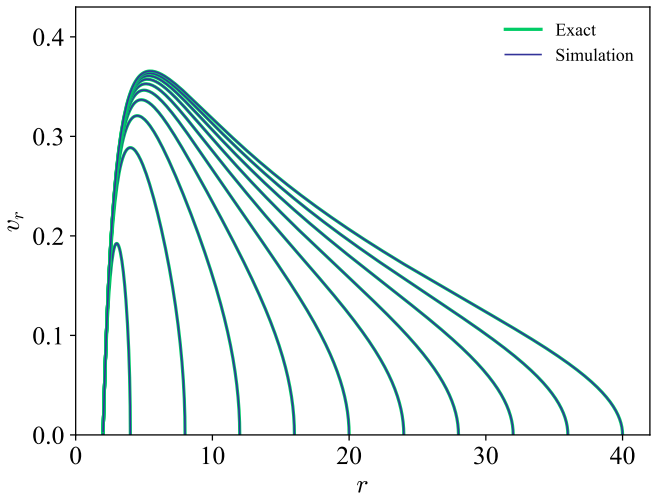

Figure 3.15: Velocity as a function of radius for radial geodesics computed from the infall of test particles (blue) starting at rest. The initial radii are spaced evenly for $r_0/M \in [4, 40]$, and the corresponding exact solutions are shown in green. Central mass is $M = 1$.

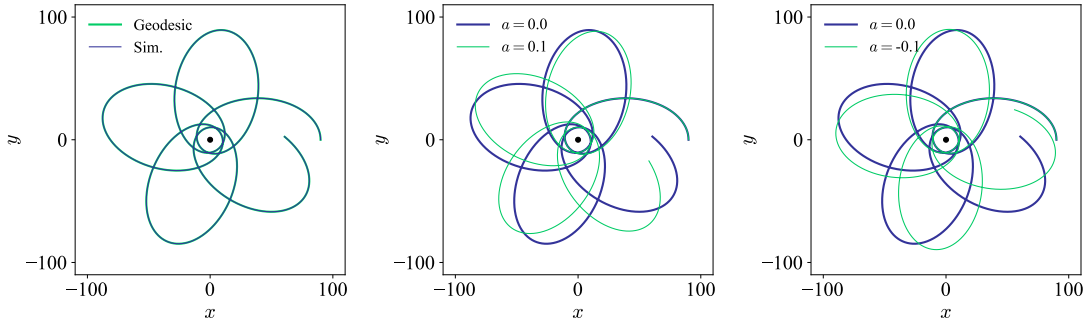

Figure 3.16: Precession in the Schwarzschild (left) and Kerr metrics (middle and right) with $M = 1$. The orbit in the Schwarzschild metric matches the same orbit as computed from a direct integration of the geodesic equation. With $a/M = 0$ in the Kerr metric we reproduce the Schwarzschild orbit as expected. With non-zero a/M in the Kerr metric, the angle of apsidal advance is decreased for the prograde orbit ($a/M = 0.1$) and increased for the retrograde orbit ($a/M = -0.1$). Large values of spin are also possible, however in those cases the direction of orbital advance becomes difficult to distinguish in a figure.

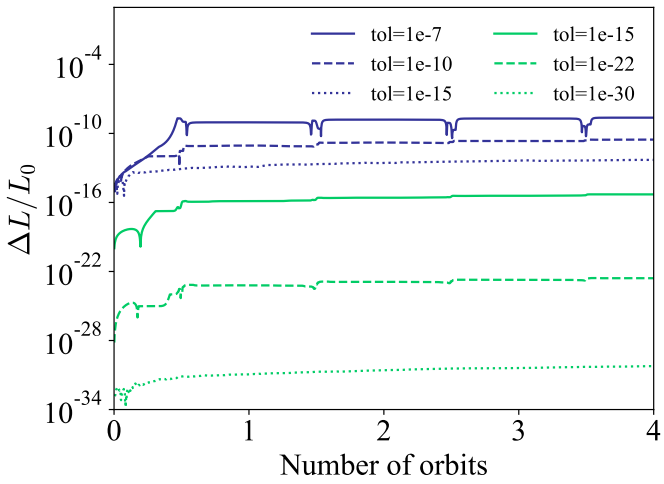

Figure 3.17: Fractional error in angular momentum (L) throughout the precessing orbit in the Schwarzschild metric, described in Section 3.8.2. Calculations are computed in double precision (blue) and quad precision (green) with 10^4 steps per orbit and varying values of $\epsilon_x = \epsilon_p = \mathrm{tol}$. Angular momentum is conserved to round off error with $\mathrm{tol} = 10^{-15}$ and $\mathrm{tol} = 10^{-30}$ for double and quad precision calculations, respectively.

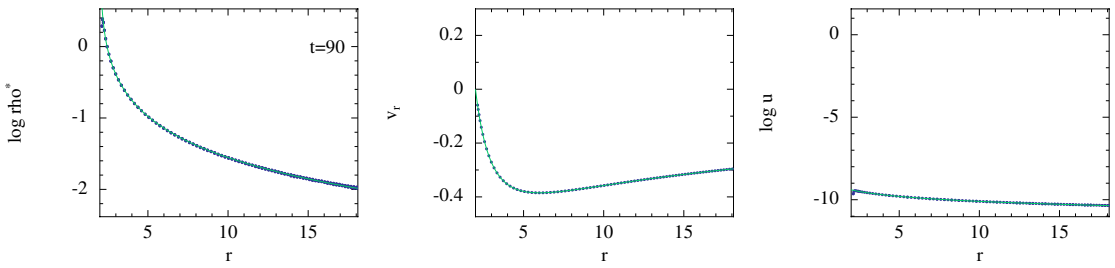

Figure 3.18: Results of spherically symmetric 'geodesic' Bondi accretion in the Schwarzschild metric with $M = 1$ and $\alpha_{\mathrm{AV}} = 0$. Blue dots show SPH particles while green lines show the exact solution. This demonstrates that the time evolution of the energy equation is correct.

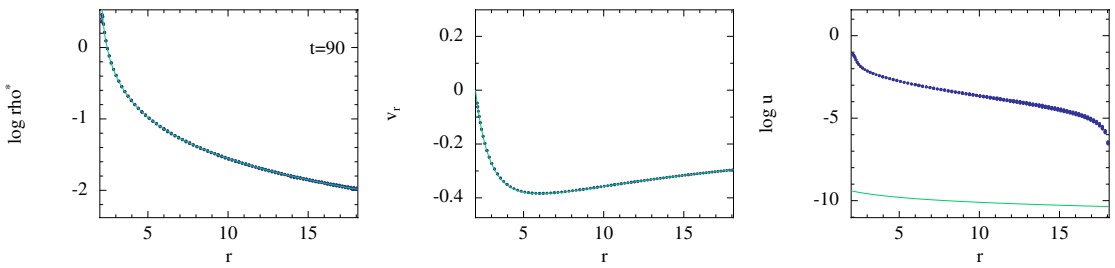

Figure 3.19: As in Fig. 3.18 but artificial viscosity turned on as normal i.e. $\alpha_{\mathrm{AV}} = 1$. This produces excessive viscous heating, evident in the thermal energy profile (right).

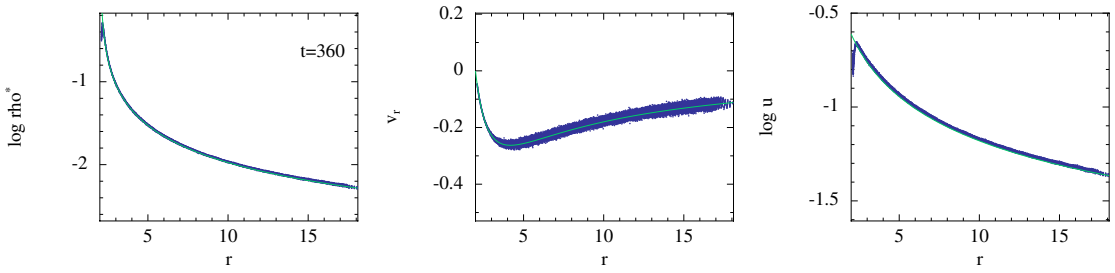

Figure 3.20: Results of spherically symmetric 'sonic point' Bondi accretion in the Schwarzschild metric with $M = 1$ and $\alpha_{\rm AV} = 0.1$. Blue dots show SPH particles while green lines show the exact solution. The match between the numerical and analytic solutions demonstrates that our implementation of hydrodynamics in strong-field gravity is correct.

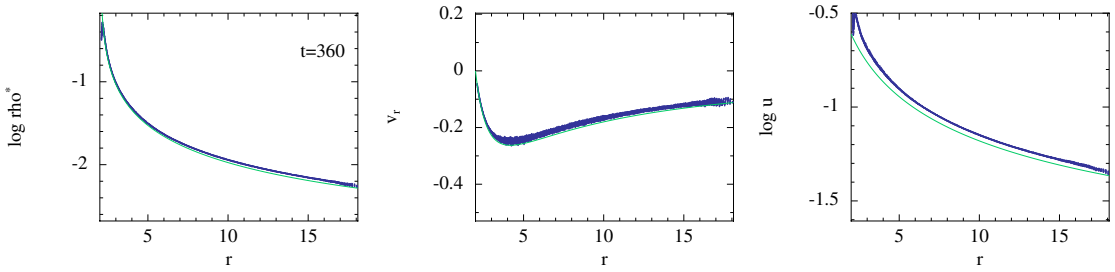

Figure 3.21: As in Fig. 3.20 but with $\alpha_{\rm AV} = 1$. This produces excessive viscous heating (right), as in the geodesic case, however it does reduce particle noise in the velocity profile (middle).

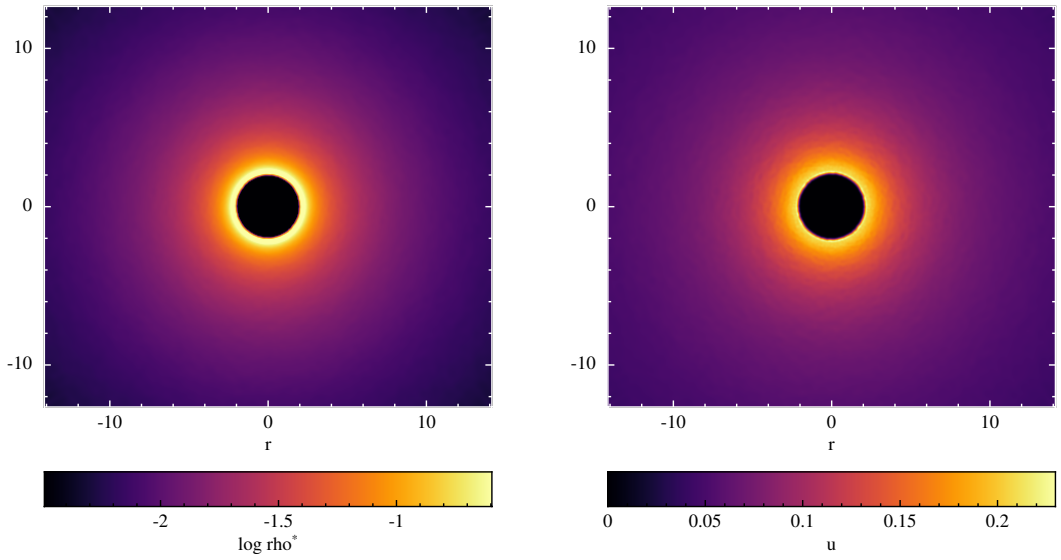

Figure 3.22: Rendered slices of spherically symmetric 'sonic point' Bondi accretion as in Fig. 3.20, showing conserved density ρ^* (left) and specific thermal energy u (right). Slice is taken through the $z = 0$ plane. The density and thermal energy gradients are correctly captured at the inner boundary so long as the event horizon is well resolved.

Circular orbits

The orbital frequency Ω of a circular geodesic in the Schwarzschild metric is identical to the frequency of a Newtonian orbit

$$\Omega^2 = \left(\frac{\mathrm{d}\phi}{\mathrm{d}t}\right)^2 = \frac{M}{r^3}. \tag{3.111}$$

Figure 3.13 (left) shows a test particle orbit with initial position $(r, \theta, \phi) = (10M, \pi/2, 0)$ and initial velocity $(v^r, v^\theta, v^\phi) = (0, 0, \Omega)$, simulated for 15 orbital periods with constant time step $\Delta t = 0.01M$ throughout. Energy and angular momentum (e, p_ϕ) are conserved to machine precision ($\Delta E/E \approx 10^{-15}$), and the radius also remains constant to machine precision.

Radial geodesics

The velocity of a radially in-falling particle beginning at rest in the Schwarzschild metric is given by

$$v^r(r) = \frac{1 - \frac{2M}{r}}{\sqrt{1 - \frac{2M}{r_0}}} \sqrt{2M\left(\frac{1}{r} - \frac{1}{r_0}\right)}, \tag{3.112}$$

where r_0 is the starting radius. Figure 3.15 shows our calculations of radially in-falling test particles from several radii, compared to the exact solution. We integrate with constant time step $\Delta t = 0.01M$ until the particles reach $r = 2.001M$. The largest L_2 error out of the 10 simulations occurs for the $r_0 = 4M$ case, with $L_2 = 6.7 \times 10^{-8}$ when using data points every 31 time steps. This confirms that radial infall is accurately captured by our code.

Apsidal advance

Figure 3.16 (left) shows the trajectory of a precessing orbit. The orbit begins at $r_0 = 90M$ with tangential velocity $v_\mathrm{t} = 0.0521157$ such that the pericentre distance is $\approx 10M$, i.e.

$$(r, \theta, \phi) = \left(r_0, \frac{\pi}{2}, 0\right), \tag{3.113}$$

$$(v^r, v^\theta, v^\phi) = \left(0, 0, \frac{v_t}{r_0}\right). \tag{3.114}$$

The trajectory of our simulation follows the trajectory as computed from a direct integration of the geodesic equation with coordinate time derivatives (see e.g. Equation 4.2 of Tejeda et al. 2017). We find a change in azimuthal angle of approximately $82.3°$ between the first apocentre and the starting position. This is consistent with the exact value of $82.4°$ (see e.g. Equation 2 of Wegg 2012) to within measurement error. A more accurate value can be obtained with higher temporal resolution at the apocentre. This confirms that the apsidal advance is as expected from theory.

3.8.3 Orbital dynamics — Kerr Metric

We perform further tests of orbital dynamics using the Kerr metric in spherical Boyer-Lindquist coordinates, however the same results can be reproduced using the equivalent Cartesian representation (see Appendix A.3.2). We again use a black hole mass of $M = 1$ in all simulations.

Circular orbits

Circular geodesics are allowed in the Kerr metric when the plane of orbit is perpendicular to the spin axis of the black hole (i.e. $\theta = \pi/2$ in Boyer-Lindquist coordinates). The orbital frequency for a circular orbit in the Kerr metric is given by (Abramowicz et al., 1978)

$$\Omega = \frac{M^{1/2}}{r^{3/2} + aM^{1/2}}, \tag{3.115}$$

for orbits going in the positive ϕ direction, where $|a| \leq M$ is the angular momentum parameter of the black hole. Prograde orbits correspond to $a > 0$, whilst retrograde orbits are when $a < 0$. Figure 3.13 (right) shows a circular orbit at a radius of $2M$ for a maximally rotating black hole ($a/M = 1$), evolved for 15 orbital periods with constant $\Delta t = 0.01M$ and compared to the exact orbit. Again, energy and angular momentum (e, p_ϕ) are conserved to machine precision, and the radius also remains constant to machine precision.

Epicyclic motion

An otherwise circular orbit given a small, linear, radial perturbation, will undergo epicyclic motion in the Kerr metric. The epicyclic frequency κ is given by (Kato, 1990; Lubow et al., 2002)

$$\kappa^2 = \Omega^2 \left(1 - \left[\frac{6M}{r} - \frac{8aM^{1/2}}{r^{3/2}} + \frac{3a^2}{r^2}\right]\right). \tag{3.116}$$

We compute κ for a range of values of a, by setting a series of test particles on epicyclic orbits at different radii. To induce the epicyclic motion we set the initial angular velocity to be $v_\phi = 1.00001\Omega$ (i.e. a 0.001% increase from the circular velocity). For simplicity and because test particles do not interact, simulations with the same a were computed simultaneously. Each simulation was run for $t = 30000M$ to ensure that epicycles with the lowest frequency completed at least 20 cycles. We then measure the frequency, as described in Appendix A.4. Figure 3.14 (left) shows the results of all simulations for $a \in [-1, 1]$ and $M = 1$. The radii at which $\kappa = 0$ correspond to the innermost stable circular orbit (ISCO). The typical errors are of order $\Delta\kappa/\kappa \approx 10^{-3}$. However, the errors can be made arbitrarily small by taking a longer time series, since the smallest frequency measurement possible with a Fourier transform is $\delta\Omega = 2\pi/t_{\max}$.

Vertical-oscillation frequency

A circular orbit given a small, linear, vertical perturbation, will undergo vertical oscillations in the Kerr metric. The vertical oscillation frequency Ω_z is given by (Kato, 1990; Lubow et al., 2002)

$$\Omega_z^2 = \Omega^2 \left(1 - \left[\frac{4aM^{1/2}}{r^{3/2}} + \frac{3a^2}{r^2}\right]\right). \tag{3.117}$$

Figure 3.14 (right) shows our calculations of the vertical oscillation frequency, following a similar setup as above (see Section 3.8.3). To induce vertical oscillations we perturb test particles up out of the $\theta = \pi/2$ plane by 0.001% (i.e. $\theta = (1 - 0.00001)\,\pi/2$). The exact solutions for each value of a are truncated at the radius corresponding to the ISCO. Typical errors are similar to those for the epicyclic frequency ($\Delta\Omega_z/\Omega_z \approx 10^{-3}$), and can again be made smaller by taking a longer time series.

Apsidal advance

Figure 3.16 (middle & right) demonstrates the effect of black hole spin on apsidal advance. We use similar initial conditions as in Section 3.8.2 however with $a/M = \{-0.1, 0, 0.1\}$ in the Kerr metric and performed these calculations in Cartesian-like coordinates. We chose relatively small values of spin in order to distinguish the direction of orbital advance, however there is no limit on the values of spin that the code can handle. The initial conditions for this orbit are such that in the x–y plane the initial starting position and velocity is the same for all three orbits since $r^2 \neq x^2 + y^2 + z^2$ in Boyer-Lindquist coordinates, i.e.

$$(x, y, z) = (r_0, 0, 0), \tag{3.118}$$

$$(v^x, v^y, v^z) = (0, v_{\rm tan}, 0). \tag{3.119}$$

where again we use $r_0 = 90M$ and $v_{\rm tan} = 0.0521157$. The angle of precession decreases for prograde orbits, and increases for retrograde orbits, as expected. Combined with the high accuracy of our epicyclic frequency measurements, this confirms that we capture Kerr orbital dynamics accurately.

Conservation of angular momentum

Figure 3.17 shows the conservation of angular momentum in our timestepping algorithm described in Section 3.6.3. We compute the precessing orbit in the Schwarzschild metric in Cartesian coordinates (Section 3.8.2) using both double (64 bit) and quad (128 bit) precision, whilst varying the number of steps per orbit (step size), and the tolerance (ϵ_x, ϵ_p) of the implicit solve. The conserved angular momentum in the Schwarzschild metric is

$$L = r^2 \frac{{\rm d}\phi}{{\rm d}t} U^0. \tag{3.120}$$

We define the orbital period for this trajectory to be the time between consecutive apocentres ($t_{\rm orbit} \approx 2390M$ with our setup). With 10^4 steps per orbit, we find that we conserve angular momentum to round off error provided ϵ_p and ϵ_x are sufficiently small. Using tolerances of 10^{-15} (double precision) and 10^{-30} (quad precision) angular momentum is conserved to round-off error. Therefore in our 3D code, which is double precision, we set $\epsilon_p = \epsilon_x = 10^{-15}$ by default.

3.8.4 General relativity — Bondi accretion

To test our ability to perform hydrodynamics in a curved spacetime and not just special relativity, we consider spherically symmetric flow in the Schwarzschild metric. Hawley et al. (1984a) give the analytic solution, which is a generalisation of non-relativistic Parker-Bondi flow. To simulate the accretion solution, we inject shells (geodesic spheres) of SPH particles from a particular radius at discrete, regular intervals. The particles are given density, velocity and thermal energy corresponding to the exact solution at the radius which they are injected. For details of the algorithm we refer the reader to the publicly available subroutine in PHANTOM used in applications of stellar winds (Toupin et al. 2015a,b; Siess et al. in prep).

Geodesic flow

The solution for marginally bound, spherically symmetric, radial flow of 'pressure-less' gas is given by (Hawley et al., 1984a)[1]

$$v^r(r) = \sqrt{\frac{2M}{r}}\left(1 - \frac{2M}{r}\right), \tag{3.121}$$

$$\rho = \frac{\rho_0}{r^2}\sqrt{\frac{r}{2M}}, \tag{3.122}$$

$$u(r) = u_0\left(r^2\sqrt{\frac{2M}{r}}\right)^{1-\gamma_{\rm ad}}, \tag{3.123}$$

where ρ_0 and u_0 are normalisation constants. The solution assumes that $u \ll 1$ everywhere, hence we must use $u_0 \ll 1$ to be consistent. The solution is also the same for inflow and outflow, aside from the sign of v^r. For our simulations we use normalisation constants $u_0 = 1 \times 10^{-9}$ and $\rho_0 = 1$.

Following Hawley et al. (1984b), we inject fluid radially in toward the black hole from a radius of $r_{\rm in} = 18.1M$. To have a smooth boundary condition at $r_{\rm in}$, we keep 10 shells of particles, uniformly spaced in time, outside of the injection radius at all times. The hydrodynamic quantities v^r, ρ and u are fixed to the exact solution while the shells remain outside the injection radius. As each shell moves inward and crosses $r_{\rm in}$, it is 'released' and left to evolve on its own. Once a shell is released, a new boundary shell is added to the outside of the remaining boundary shells in order to maintain a constant number of boundary shells. For the inner boundary, we simply remove particles from the simulation when they cross $r = 2.1M$.

Figures 3.18 & 3.19 show our results for geodesic Bondi accretion with 8412 particles per shell, a time spacing of $\delta t = 0.602M$ between consecutive shells, and individual particle masses of $m_a = 9 \times 10^{-4}M$. We find that we achieve best results with artificial viscosity turned off i.e. $\alpha_{\rm AV} = 0$ (Fig. 3.18). After evolving the simulation to $t = 90M$ the L_2 errors are 5.4×10^{-2}, 1.8×10^{-4} and 4.4×10^{-2} for ρ^*, v^r and u, respectively.

Figure 3.19 shows the same simulation but with the standard dissipation parameter $\alpha_{\rm AV} = 1$ for comparison. Although there are no shocks present, viscous heating leads to excess thermal energy (third panel of Figure 3.19). The excess heating is small but easily overwhelms the negligible thermal energy assumed in the test problem. To reduce viscous heating away from shocks, the standard approach in non-relativistic SPH is to implement shock detection switches. The most widely used is the switch proposed by (Cullen and Dehnen, 2010), however this is non-trivial to generalise to relativity. We experimented with a modified form of the older Morris and Monaghan (1997) switch but found it ineffective for the Bondi problem since it relies on $(-\partial v^i/\partial x^i)$ as the shock detector, which does not switch off for adiabatic contraction.

There is a small turnover in density at the inner boundary in both cases. This is merely a consequence of our inner boundary condition and does not reflect the accuracy of our density calculation in a strong field regime. The drop off occurs because particles close to the accretion radius have fewer neighbours and thus a lower density. This effect is not unique to GRSPH and would occur wherever the inner boundary was chosen to be.

[1] Note that equation (67b) of Hawley et al. (1984a) is written incorrectly

Sonic point flow

Dropping the assumption $u \ll 1$ means that the pressure between fluid elements is no longer negligible. The solution for this flow (Michel, 1972; Hawley et al., 1984a) can be written in terms of a temperature variable $T \equiv P/\rho = (\gamma_{\rm ad} - 1)u$, not to be confused with the gas temperature as defined in equation 3.22,

$$U^r(r) = \frac{C_1}{r^2 T^n}, \tag{3.124}$$

$$\rho(r) = K_0 T^n, \tag{3.125}$$

$$u(r) = n\,T, \tag{3.126}$$

where $n \equiv 1/(\gamma_{\rm ad} - 1)$ is the polytropic index and K_0 is an entropy normalisation constant. $T(r)$ is determined by the implicit equation

$$C_2 = (1 + (n+1)T)^2 \left(1 - \frac{2M}{r} + \frac{{C_1}^2}{r^4 T^{2n}}\right). \tag{3.127}$$

The constants C_1 and C_2 can be both uniquely determined through the choice of a critical point r_c,

$$C_1 = U_c\, {r_c}^2\, {T_c}^n, \tag{3.128}$$

$$C_2 = (1 + (1+n)T_c)^2 \left(1 - \frac{2M}{r_c} + \frac{{C_1}^2}{{r_c}^4 {T_c}^{2n}}\right), \tag{3.129}$$

where

$$U_c \equiv U^r(r_c) = \sqrt{\frac{M}{2r_c}}, \tag{3.130}$$

$$T_c \equiv T(r_c) = \frac{v_c^2 n}{(1+n)(1 - n v_c^2)}, \tag{3.131}$$

$$v_c \equiv v^r(r_c) = \frac{U_c}{\sqrt{1 - 3U_c^2}}. \tag{3.132}$$

To write the solution in terms of $v^r(r)$ and $\rho^*(r)$, we use equations 3.2 & 3.4 along with

$$U^0 = \frac{\sqrt{1 - 2M/r + (U^r)^2}}{1 - 2M/r}, \tag{3.133}$$

as determined by equation 3.3 for the Schwarzschild metric. For $\gamma_{\rm ad} = 5/3$, equation 3.127 yields two real solutions, one for inflow and the other for outflow (Michel, 1972). For our simulation we take care to choose the correct branch, corresponding to an inflow. We choose a critical value $r_c = 8M$ and normalise the entropy to $K_0 = 1$.

Figures 3.20 & 3.21 show the results of our simulation. We follow the same procedure as for the geodesic flow simulation, injecting shells of particles from $r_{\rm in} = 18.1M$, however this time we fill the domain all the way to the accretion radius at $r = 2.1M$ before beginning the simulation. This reduces the time taken to reach a steady state. Each shell consists of 8412 particles, with time intervals of $\delta t = 1.404M$ between each consecutive shell, and individual particle masses of $m_a = 4 \times 10^{-4} M$.

Figure 3.20 shows our results with a reduced artificial viscosity parameter of $\alpha_{\rm AV} = 0.1$. After evolving the simulation to $t = 360M$ in order to reach a steady state, the L_2 errors are 4.2×10^{-2}, 2.5×10^{-2} and 3.2×10^{-2} for ρ^*, v^r and u, respectively.

In Figure 3.21 we show the same simulation but with $\alpha_{\rm AV} = 1$ for comparison. As with the geodesic simulations above, we find excessive viscous heating when the standard artificial viscosity parameter is used. A small drop off in density can again be seen at the inner boundary, for the same reasons as discussed in the geodesic simulation. Figure 3.22 shows a rendered cross section of the conserved density ρ^* and the specific thermal energy u close to the inner boundary for the same simulation as Fig. 3.20. This demonstrates that the boundary condition is not a serious concern, so long as the event horizon is well resolved.

3.9 Conclusions

We have developed and benchmarked a 3D GRSPH code for hydrodynamics in strong field gravity. The novel aspects are:

1. Shock capturing: We demonstrated how to split viscous and thermal conduction components of the shock dissipation terms in relativistic SPH. This is important for accurate treatment of contact discontinuities (Price, 2008).

2. Entropy: We show how to formulate the equations with entropy as the conserved variable. This enables us to robustly simulate strong blast waves with no smoothing of the initial conditions without the code failing due to negative pressures.

3. Timestepping: We showed how to generalise the Leapfrog time integration scheme to relativistic SPH. We combined a symplectic and reversible method for non-separable Hamiltonians from Leimkuhler and Reich (2005) with a modified algorithm that is efficient for SPH. This allows for symplectic and reversible integration of the orbital dynamics and reversible integration of the SPH equations in the absence of dissipation. Our algorithm generalises the RESPA scheme (Tuckerman et al., 1992) employed by Price et al. (2018).

4. Benchmarking: We benchmark both our algorithm and codes against a series of standardised tests in 1D and 3D. We showed results for mildly and ultra-relativistic shocks in 1D and 3D, circular and eccentric orbits, radial geodesics, vertical and epicyclic oscillation about circular orbits in Schwarzschild and Kerr metrics, 3D relativistic spherical blast, and generalised Bondi flow.

5. Public code: We implemented our algorithms into the public SPH code PHANTOM (Price et al., 2018). Our intention is to make GR PHANTOM publicly available in due course.

We showed how to use SPH, for flows in curved metrics of space. We captured the shocks, and adjusted the clocks. Our tests, they all worked in each case.

Chapter 4

Background: Tidal disruption events

In this chapter we give a brief review on the basic physics and dynamics involved during a tidal disruptions event (TDE), which will be useful for the investigations in Chapters 5 and 6.

4.1 Disruption

A TDE occurs when a star wanders too close to a black hole and the tidal force overwhelms the self-gravity of the star. The radius from the black hole at which this occurs is called the tidal radius R_T, which can be approximated by equating the star's self-gravitational acceleration with the Newtonian surface tidal acceleration:

$$\frac{GM_*}{R_*^2} = \frac{GM_{\rm BH}R_*}{R_T^3}, \tag{4.1}$$

where M_* is the mass of the star, R_* is its radius, $M_{\rm BH}$ is the mass of the black hole, and G is the gravitational constant. Rearranging for the tidal radius gives

$$R_T = R_* \left(\frac{M_{\rm BH}}{M_*}\right)^{1/3}, \tag{4.2}$$

$$\simeq 0.46 \text{ au} \left(\frac{R_*}{R_\odot}\right)\left(\frac{M_{\rm BH}}{10^6 M_\odot}\right)^{1/3}\left(\frac{M_*}{M_\odot}\right)^{-1/3}, \tag{4.3}$$

$$\simeq 47.1 R_g \left(\frac{R_*}{R_\odot}\right)\left(\frac{M_{\rm BH}}{10^6 M_\odot}\right)^{-2/3}\left(\frac{M_*}{M_\odot}\right)^{-1/3}, \tag{4.4}$$

where $R_g \equiv GM_{\rm BH}/c^2$ is the gravitational radius. For stellar orbits with pericentre distance $r_p \leq R_T$ the star is expected to be completely disrupted, while for $r_p > R_T$ the star will survive [1]. The 'strength' of the encounter is typically measured by the penetration factor,

$$\beta \equiv \frac{R_T}{r_p}, \tag{4.5}$$

where $\beta \geq 1$ would correspond to a full disruption.

From Equation 4.4, two important points become apparent:

[1] If r_p is only slightly greater than R_T, then the star may undergo a partial disruption, in which only the outer layers of the star are stripped away and the core survives. The exact threshold for partial disruptions depends on the internal structure of the star. Guillochon and Ramirez-Ruiz (2013) quantify the threshold precisely for polytropic stars, while Ryu et al. (2020) do so for more realistic stars using MESA (Modules for Experiments in Stellar Astrophysics) models.

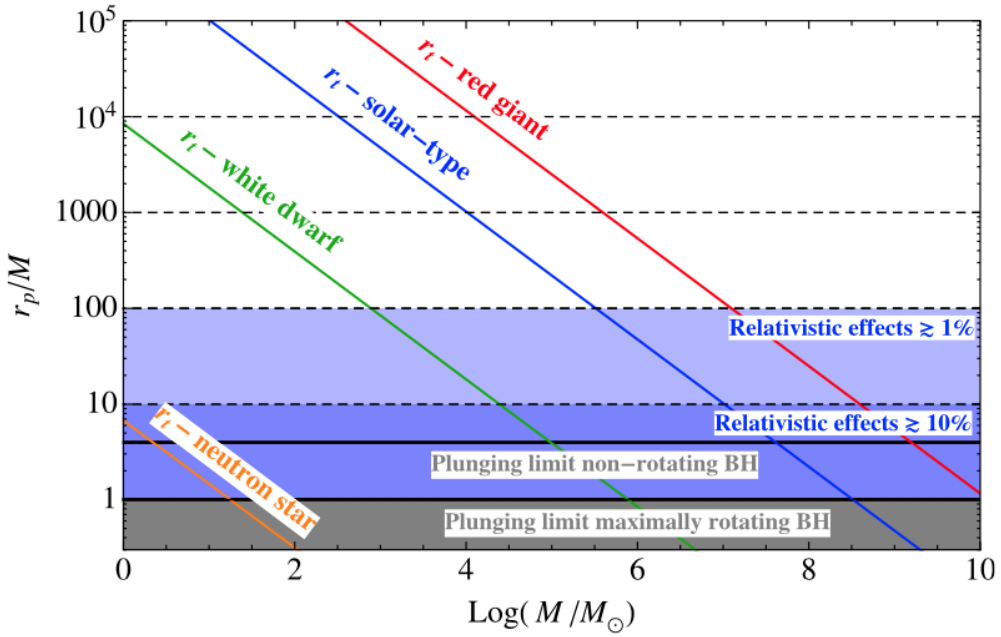

Figure 4.1: Parameter space for the tidal disruption of different types of stars (Tejeda et al., 2017). Here, the y-axis is the pericentre in units of R_g, and $M \equiv M_{\rm BH}$. For a given type of star (red giant, solar-type, white dwarf) a TDE occurs if the the pericentre distance is below the corresponding solid line (red, blue, green) i.e. $r_p/M < r_t$. The plunging regions for non-rotating and maximally rotating black holes are shown by the solid black lines, within which a TDE will not occur because the star is completely swallowed by the black hole.

1. Tidal disruptions for solar type stars and typical supermassive black hole masses of $M_{BH} \geq 10^6 M_\odot$ are inherently general relativistic, i.e. $R_T \sim R_g$. This means that general relativistic effects, such as relativistic precession, are significant.

2. There is a part of parameter space in which the tidal radius is smaller than the event horizon (Schwarzschild radius, $R_s = 2R_g$) of the black hole. For a solar type star, this occurs when the black hole mass is greater than roughly $10^8 M_\odot$, known as the 'Hills mass' (Hills, 1975).

Figure 4.1 from Tejeda et al. (2017) illustrates these regions of parameter space for different types of stars. Red giants can be disrupted by black holes with mass up to $\sim 10^9 M_\odot$. This is a rough upper limit on black holes that can host a TDE. It may be possible for tip-of-the-red-giant-branch and some AGB stars to be disrupted by even larger black holes (see figure 14 of MacLeod et al. 2012). On the other hand, neutron stars can only be disrupted by stellar-mass black holes up to $\sim 10 M_\odot$, depending on the black hole spin and neutron star equation of state (Foucart, 2012).

The origin of stars that are tidally disrupted by the central black hole of a galaxy is typically from the sphere of influence with radius (Stone et al., 2019)

$$r_h = \frac{GM_{\rm BH}}{\sigma^2} \simeq 0.43 \text{ pc} \left(\frac{M_{\rm BH}}{10^6 M_\odot}\right) \left(\frac{\sigma}{100 \text{km/s}}\right)^{-2}, \tag{4.6}$$

where σ is the velocity dispersion of the host galaxy. This distance is much greater than the tidal radius and therefore also greater than the pericentre distance (since $r_p \leq R_T$ for disruption).

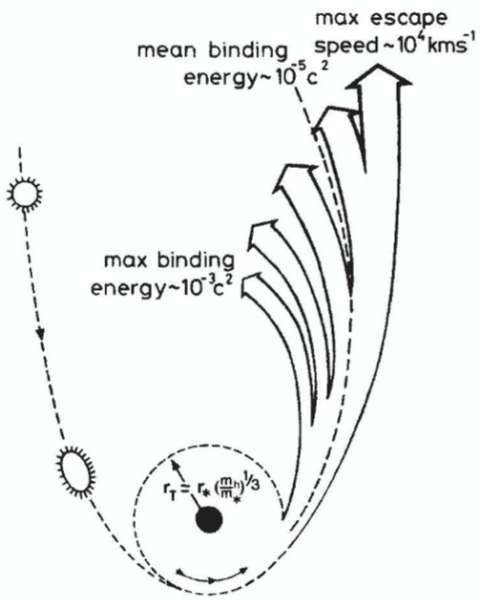

Figure 4.2: Trajectory of the star and stellar debris during a TDE (Rees, 1988).

Thus, tidally disrupted stars approach the supermassive black hole on nearly parabolic (marginally bound) orbits, with specific orbital energy close to zero. A rough schematic of a TDE and the debris trajectory is shown in Figure 4.2.

Following disruption, there is a spread in the specific orbital energy of the debris, with roughly half the debris becoming bound to the black hole and the other half becoming unbound. This spreading can be modelled analytically using a 'frozen-in' approximation: Assume that the star's disruption through pericentre happens much faster than any other process that would redistribute the kinetic of the material; in other words, assume the star has an instantaneous loss of self-gravity as it reaches the tidal radius. Thus the spread in energy $\Delta\epsilon$ is equal to the spread in gravitational potential energy across the star at the tidal radius:

$$\Delta\epsilon \approx \frac{GM_{\rm BH}}{R_T - R_*} - \frac{GM_{\rm BH}}{R_T + R_*}, \tag{4.7}$$

$$\simeq \frac{2GM_{\rm BH}R_*}{R_T^2}. \tag{4.8}$$

Figure 4.3 shows the distribution of specific energy over the course of hydrodynamic simulations performed by Lodato et al. (2009), who (along with many others) found good agreement with Equation 4.8, even though it is a rather crude approximation.

4.2 Fallback

Once disrupted, the debris moves on nearly geodesic orbits, and the half that is bound returns to the black hole at a characteristic rate given by (Rees, 1988; Phinney, 1989)

$$\dot{M}_{\rm return} = \frac{dm}{d\epsilon}\left|\frac{d\epsilon}{dt}\right| = \frac{dm}{d\epsilon}\frac{(2\pi GM_{\rm BH})^{2/3}}{3}t^{-5/3}, \tag{4.9}$$

where $\epsilon \propto r^{-1} \propto t^{-2/3}$ from Kepler's third law. As shown in Figure 4.3, the spread in specific energy can be approximated by a top-hat, meaning that $dm/d\epsilon \approx 1$. This gives the famous $\dot{M} \propto t^{-5/3}$ relation for the mass return rate, which is the relation that is often used to classify observed transients as TDEs.

As the debris falls back is must be accreted onto the black hole in order to power a light curve. Figure 4.4 shows the luminosity evolution observed from several TDEs (and super-luminous supernovae), which reach peak luminosities of $\sim 10^{10-11} L_{\odot}$. It is commonly assumed that the debris will circularise very rapidly, in which case the bolometric light curve will follow $\dot{M}_{\rm return}$. However, the exact details of debris circularisation, accretion and subsequent emission are still uncertain, and are the subject of our investigations in Chapters 5 and 6. The results of recent TDE simulations are summarised in Lodato et al. (2015), while Komossa (2015) outlines the status of observations.

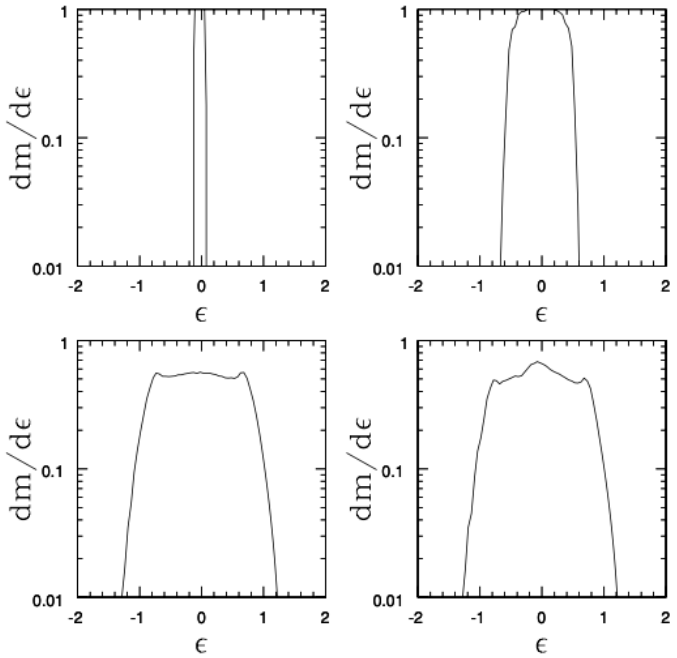

Figure 4.3: Distribution of specific energy during a TDE in hydrodynamical simulations performed by Lodato et al. (2009). Units are such that $M_{\rm BH} = G = c = 1$. *Upper left:* initial condition. *Upper right:* star at pericentre. *Lower left:* star at 4 times pericentre. *Lower right:* star at 10 times pericentre.

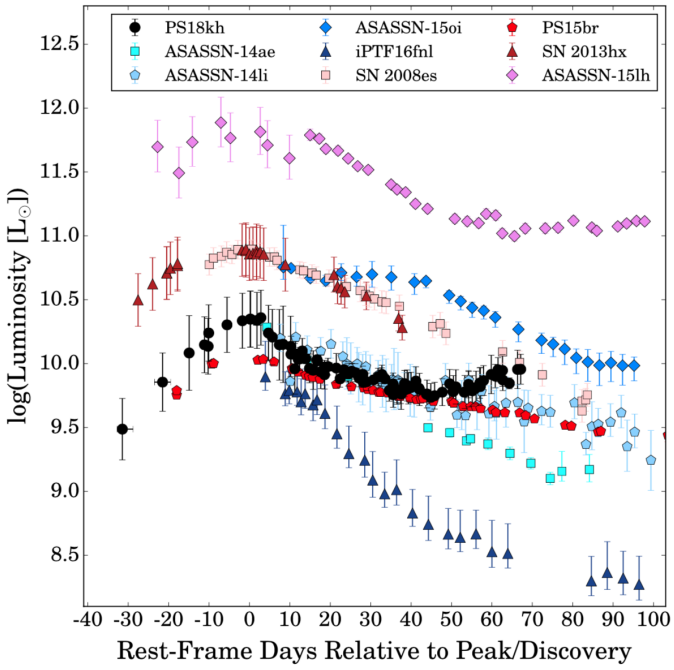

Figure 4.4: Light curves of several TDEs (blue and black markers) and super-luminous supernovae (red/pink markers), as presented in Holoien et al. (2019). The luminosity rises rapidly and decays over the course of many months.

Chapter 5

Disc formation from tidal disruption of stars on eccentric orbits by Kerr black holes using GRSPH

We perform 3D general relativistic smoothed particle hydrodynamics (GRSPH) simulations of tidal disruption events involving 1 $M_\odot$ stars and $10^6 M_\odot$ rotating supermassive black holes. We consider stars on initially elliptical orbits both in, and inclined to, the black hole equatorial plane. We confirm that stream-stream collisions caused by relativistic apsidal precession rapidly circularise the disrupted material into a disc. For inclined trajectories we find that nodal precession induced by the black hole spin (i.e. Lense-Thirring precession) inhibits stream-stream collisions only in the first orbit, merely causing a short delay in forming a disc, which is inclined to the black hole equatorial plane. We also investigate the effect of radiative cooling on the remnant disc structure. We find that with no cooling a thick, extended, slowly precessing torus is formed, with a radial extent of 5 au (for orbits with a high penetration factor). Radiatively efficient cooling produces a narrow, rapidly precessing ring close to pericentre. We plot the energy dissipation rate, which tracks the pancake shock, stream-stream collisions and viscosity. We compare this to the effective luminosity due to accretion onto the black hole. We find energy dissipation rates of $\sim 10^{45}$ erg s^{-1} for stars disrupted at the tidal radius, and up to $\sim 10^{47}$ erg s^{-1} for deep encounters.

5.1 Introduction

The tidal disruption of stars by supermassive black holes is thought to power bright electromagnetic flares (Lidskii and Ozernoi, 1979; Rees, 1988) that are observed at the centre of galaxies (see Komossa, 2015, for a review). This occurs when a star gets too close to the black hole, such that the tidal forces of the black hole exceed the self gravity of the star (Hills, 1975). The subsequent accretion of stellar material onto the black hole proves useful as a tool for probing quiescent supermassive black holes (SMBHs).

The luminosity for such tidal disruption events (TDEs) decays loosely as a power-law $\propto t^{-5/3}$ (e.g. Gezari et al., 2008, 2012; Auchettl et al., 2017), which is consistent with the predicted mass

return rate of stellar debris at late times (Rees, 1988; Phinney, 1989).[1]

After the initial disruption, the star — initially on a parabolic orbit — is torn into a long stream, with roughly half the mass being gravitationally bound to the black hole and returning on highly eccentric orbits. In order for the light curve to trace the fallback rate, the stellar debris must circularise, form an accretion disc, and accrete on a timescale much shorter than the return time of the most tightly bound debris (Stone et al., 2019) — assuming that the observed flare is powered by accretion onto the black hole and not by fallback shocks and circularisation (e.g. Lodato, 2012; Piran et al., 2015; Jiang et al., 2016). The manner in which material circularises is still uncertain, but is thought to be due to shock dissipation from the self-intersection of the debris stream, caused by relativistic apsidal precession (Rees, 1988; Cannizzo et al., 1990; Hayasaki et al., 2013; Bonnerot et al., 2016). However, the process of circularisation is further complicated by frame dragging. This causes precession of the orbital plane with each pericentre passage, which can prevent stream self-intersection (Cannizzo et al., 1990; Guillochon and Ramirez-Ruiz, 2015).

Investigating TDEs numerically presents a significant challenge, since the process involves a large range of length and time scales that need to be resolved from disruption to accretion. In the case of a $1M_\odot$ star on a parabolic orbit disrupted by a $10^6 M_\odot$ SMBH, the period of the most bound debris is $\sim 10^3$ times greater than the dynamical time of the star, while the semi-major axis of the most bound debris is $\sim 10^4$ times greater than the stellar radius (Stone et al., 2019). As a consequence, most previous numerical studies have focused on the details of the initial disruption process, and have not simulated the subsequent debris fallback and predicted disc formation (e.g. Evans and Kochanek, 1989; Laguna et al., 1993; Khokhlov et al., 1993; Frolov et al., 1994; Diener et al., 1997; Lodato et al., 2009; Guillochon et al., 2009; Guillochon and Ramirez-Ruiz, 2013; Tejeda et al., 2017; Gafton and Rosswog, 2019). The relativistic SPH calculations of Ayal et al. (2000) did follow fallback, however they were unable to resolve an accretion disc due to the small number of SPH particles employed. Guillochon et al. (2014) also followed debris fallback in their simulations, but were only able to form highly elliptic accretion flows since they had no treatment of relativistic effects, and only followed the fallback in the case of a $10^3 M_\odot$ intermediate mass black hole. Similarly, Rosswog et al. (2008) and Shiokawa et al. (2015) showed little debris circularisation, although they also restricted their calculations to a more numerically favourable choice of parameters, namely the disruption of white dwarfs by intermediate-mass black holes.

Hayasaki et al. (2013) were the first to convincingly demonstrate disc formation and debris stream self-intersection due to apsidal precession around SMBHs, using a pseudo-Newtonian gravitational potential in SPH calculations. Similar studies by Bonnerot et al. (2016) and Sadowski et al. (2016) confirmed their results, although all three studies only considered non-rotating black holes, and stars on initially bound, highly eccentric orbits. The role that black hole spin plays in circularisation has only recently been investigated numerically by Hayasaki et al. (2016). Using SPH with a post-Newtonian approximation for the Kerr metric, they showed that nodal precession for highly elliptical orbits out of the black hole spin plane can delay debris circularisation.

In this paper, we investigate debris circularisation and subsequent disc formation around rotating black holes, with particular interest in initial orbits that are out of the black hole spin plane. We use general relativistic smoothed particle hydrodynamics (GRSPH) in a fixed background

[1] It is worth noting that the exact power-law dependence varies in both optical/UV (e.g. van Velzen et al., 2019, 2020) and quasi-thermal X-ray emission (Auchettl et al., 2017). Furthermore, at late times, UV light curves tend to flatten, while some X-ray curves show an exponential decay.

Table 5.1: Parameters for each simulation

No.	e	β	a	θ	cooling
1	0.95	5	0	0°	adiabatic
2	0.95	5	0.99	0°	adiabatic
3	0.95	5	0.99	30°	adiabatic
4	0.95	5	0.99	60°	adiabatic
5	0.95	5	0.99	89°	adiabatic
6	0.95	1	0.99	60°	adiabatic
7	0.95	5	0	0°	isentropic
8	0.95	5	0.99	60°	isentropic

Kerr metric, allowing us to treat both apsidal precession and nodal precession correctly in the strong field limit. As in the studies listed above, we limit ourselves to stars on initially bound, highly eccentric orbits.

This paper is organised as follows. In Section 5.2 we describe the method and initial conditions. In Section 5.3 we present our results, investigating the effect of black hole spin and inclination, penetration factor and efficiency of radiative cooling. We discuss our results in Section 5.4 and present our conclusions in Section 5.5.

5.2 Method

We simulated the tidal disruption of solar type stars in 3D using GRSPH. We used the general relativistic implementation of PHANTOM (Price et al., 2018) as described in Liptai and Price (2019) to perform our calculations. The calculation is performed in the Kerr metric in Boyer-Lindquist coordinates (with black hole spin vector along the z-axis), which describes the spacetime around a rotating black hole for a distant observer, along with Newtonian self-gravity in order to hold the star together during the pre-disruption phase (see Appendix B.2). We set an accretion radius at $r_{\rm acc} = 5GM_{\rm BH}/c^2$ i.e. within the innermost stable circular orbit (ISCO) for a Schwarzschild black hole. Particles that fall within this radius are removed from the simulation. This prevents particles requiring very small time steps close to the horizon, which would significantly hinder code performance.

5.2.1 Setup

We consider the disruption of stars with mass $M_* = 1M_\odot$ and radius $R_* = 1R_\odot$ by a supermassive black hole with mass $M_{\rm BH} = 10^6 M_\odot$. Each star is placed on an eccentric orbit at apocenter $R_{\rm a} = R_{\rm p}(1+e)/(1-e)$, with velocity $v_{\rm a} = \sqrt{GM_{\rm BH}(1-e)/R_a}$, where e is the eccentricity and $R_{\rm p}$ is the Newtonian pericentre distance. In practice, the point of closest approach can differ from $R_{\rm p}$ by up to $\sim 2GM_{\rm BH}/c^2$ due to relativistic effects, and thus the effective penetration factor β can differ by up to ~ 1 for our most penetrating orbits.

We vary the orbital inclination θ, the black hole spin a, and the penetration factor $\beta \equiv R_{\rm t}/R_{\rm p}$, where $R_{\rm t} = R_*(M_{\rm BH}/M_*)^{1/3}$ is the tidal radius. For our choice of parameters we have

$$R_{\rm p} = 47.1R_g \left(\frac{\beta}{1}\right)^{-1} \left(\frac{R_*}{R_\odot}\right) \left(\frac{M_{\rm BH}}{10^6 M_\odot}\right)^{-2/3} \left(\frac{M_*}{M_\odot}\right)^{-1/3}, \tag{5.1}$$

where $R_g \equiv GM_{\rm BH}/c^2$. For orbits in the black hole equatorial plane, we place the star on the x-axis, while for inclined trajectories we rotate the plane of orbit up by an angle θ from the x-y plane.

We model the star as an initially polytropic sphere with polytropic index $\gamma = 5/3$, using approximately 524K particles ($\sim 4\pi 50^3/3$). We initially place the particles on a cubic lattice, and then stretch their radial positions to achieve the desired density profile, as given by the corresponding solution to the Lane-Emden equation, using the 'star' setup in PHANTOM (Price et al., 2018). We do not 'relax' the star prior to beginning the calculation. In practice, the relaxation timescale is shorter than the orbital timescale and thus the stellar structure settles by the time the star reaches pericentre.

We perform our simulations in geometric units where $G = c = M_{\rm BH} = 1$ but present results in physical units assuming a $10^6 M_\odot$ black hole. The corresponding transformations from code to physical units are given by

$$t_{\rm phys} = 4.926{\rm s} \times t_{\rm code} \left(\frac{M_{\rm BH}}{10^6 M_\odot}\right), \tag{5.2}$$

$$R_{\rm phys} = 0.0098{\rm au} \times R_{\rm code} \left(\frac{M_{\rm BH}}{10^6 M_\odot}\right). \tag{5.3}$$

Table 5.1 shows a list of our simulations presented in this paper and the parameters used for each. We initially considered a wider set of parameters, including more bound orbits similar to those computed by Bonnerot et al. (2016), but since most tidal disruptions are expected to involve stars on marginally bound orbits, we omit these calculations from our analysis in the interest of brevity.

5.2.2 Accretion luminosity and heating rate

We derive an effective luminosity from the mass accretion rate (cf. Vigneron et al., 2018)

$$L_{\rm acc} = \epsilon \dot{M} c^2, \tag{5.4}$$

where $\dot{M}$ is the mass accretion rate crossing our inner boundary, and $\epsilon = 0.2$ is the efficiency based on our inner accretion radius.

Our second estimate of the energy release comes from the irreversible dissipation of energy produced by shocks and viscous heating. This is fairly straightforward to compute in our GRSPH code since we evolve an entropy variable $K \equiv P/\rho^\gamma$ according to

$$\frac{dK}{dt} = \frac{K}{u}\left(\frac{du}{dt} - \frac{P}{\rho^2}\frac{d\rho}{dt}\right), \tag{5.5}$$

which for an individual particle, denoted by the subscript a, involves only the SPH shock heating term $\Lambda^{\rm shock}$ (cf. equation 69 of Liptai and Price, 2019)

$$\frac{dK_a}{dt} = \frac{K_a}{u_a} U_a^0 \Lambda_a^{\rm shock}. \tag{5.6}$$

Here U^0 is the temporal component of the four velocity, and ρ, P and u are the density, pressure and specific thermal energy of the gas, respectively. Thus we identify the $U_a^0 \Lambda_a^{\rm shock}$ term as the

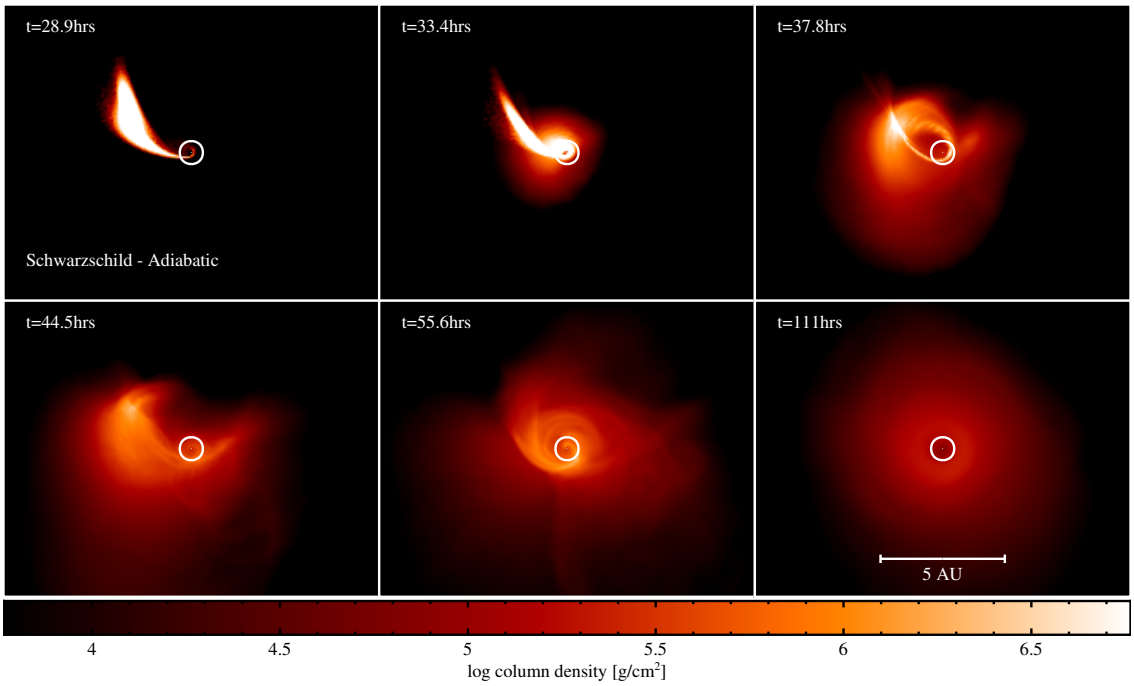

Figure 5.1: Snapshots of the debris fallback projected in the x-y plane for the $e = 0.95$, $\beta = 5$, $\theta = 0°$, $a = 0$ adiabatic simulation (Sim. 1). Starting at apocentre on the $+x$-axis, the star travels counter-clockwise coming within $< 10R_g$ of the black hole at pericentre (not shown). Apsidal precession advances the orbit by $> 90°$ (panel 1), which on the second pericentre passage (panel 2) causes the stream to self-intersect and dissipate orbital energy through shocks (panel 3). Over the next few orbital periods, the debris circularises and forms a thick torus (panel 6). White circle indicates the tidal radius R_t.

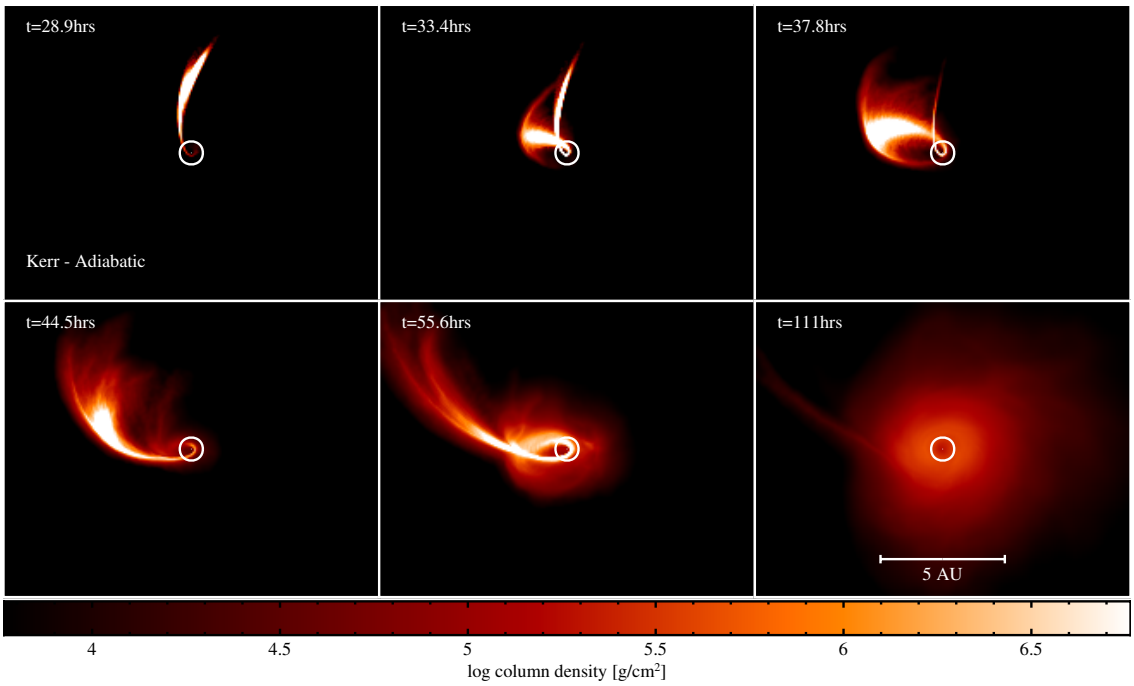

Figure 5.2: Snapshots of the debris fallback for the $e = 0.95$, $\beta = 5$, $\theta = 60°$, $a = 0.99$ adiabatic simulation (Sim. 4), projected in the initial orbital plane. Since the black hole is rotating rapidly and the initial orbit does not lie in the spin plane, nodal precession moves the star into a new orbital plane after the first pericentre passage, preventing stream self-intersection early on. However as the stream thickens, a significant portion of the stream self-intersects and a torus is formed. White circle indicates the tidal radius R_t.

specific energy generation rate per particle, and hence the total injected luminosity at a given time is

$$L_{\rm shock} = \sum_a m_a U_a^0 \Lambda_a^{\rm shock}, \tag{5.7}$$

where m_a is the particle mass. We emphasise that this does not necessarily reflect the true luminosity evolution since energy would be radiated through a photosphere in practice (see our caveats in Sec. 5.4).

5.2.3 Radiative cooling

In our standard adiabatic calculations the heat produced by shocks (and viscosity) does not escape from the gas i.e. radiative shock cooling is *inefficient*. We also perform isentropic calculations in Section 5.3.7, where the shock heating terms are discarded from the entropy evolution in Eq. 5.6 i.e. radiative shock cooling is *efficient*. We note that in reality the gas behaviour is somewhere between these two extremes, however without doing careful radiative transfer calculations, it is not obvious how the heat generated from shocks is actually reprocessed and radiated.

5.3 Results

5.3.1 Disc formation around Schwarzschild black holes

Figure 5.1 shows snapshots of Simulation 1, in which the black hole is non-rotating and the initial stellar orbit lies in the x-y plane with $e = 0.95$ and $\beta = 5$. This calculation is adiabatic.

As the star passes pericentre, relativistic apsidal precession shifts the orbit counter-clockwise by approximately $140°$. The orbital plane of the now disrupted star remains in the x-y plane. On its return to the black hole, the stellar material is stretched into a long debris stream, with the head returning to pericentre at approximately 28.9hrs (first panel in Fig. 5.1). Following this, the head of the stream intersects the tail due to relativistic apsidal precession (second panel). The intersection occurs close to pericentre since the degree of apsidal precession is large, which also means that the tangential velocity of the head is comparable to its component perpendicular to the tail. This produces a strong shock which is able to reduce a significant fraction of the stream's orbital energy, causing it to circularise and form a thick torus over the subsequent tens of hours. The torus extends to a radius of roughly $500R_g$ (approximately 5 au, or 1.4 times the initial apoapsis).

5.3.2 Disc formation around Kerr black holes

Figure 5.2 shows snapshots of the disc formation process in Simulation 4. This calculation is the same as that shown in Figure 5.1 except the black hole is now rotating with spin $a = 0.99$ and the initial stellar orbit has inclination $\theta = 60°$.

The journey to the first pericentre passage is the same as in the equivalent Schwarzschild calculation. However, after pericentre at 11.1hrs, nodal precession due to black hole spin moves the disrupted material into a different orbital plane, in addition to relativistic apsidal precession shifting the apocentre position in the prograde direction. The stellar debris after disruption is again stretched into a long stream, with the head returning to pericentre at approximately 28.9 hrs. This time nodal precession causes the stream to miss itself, shown at 33.4 hrs (second panel in

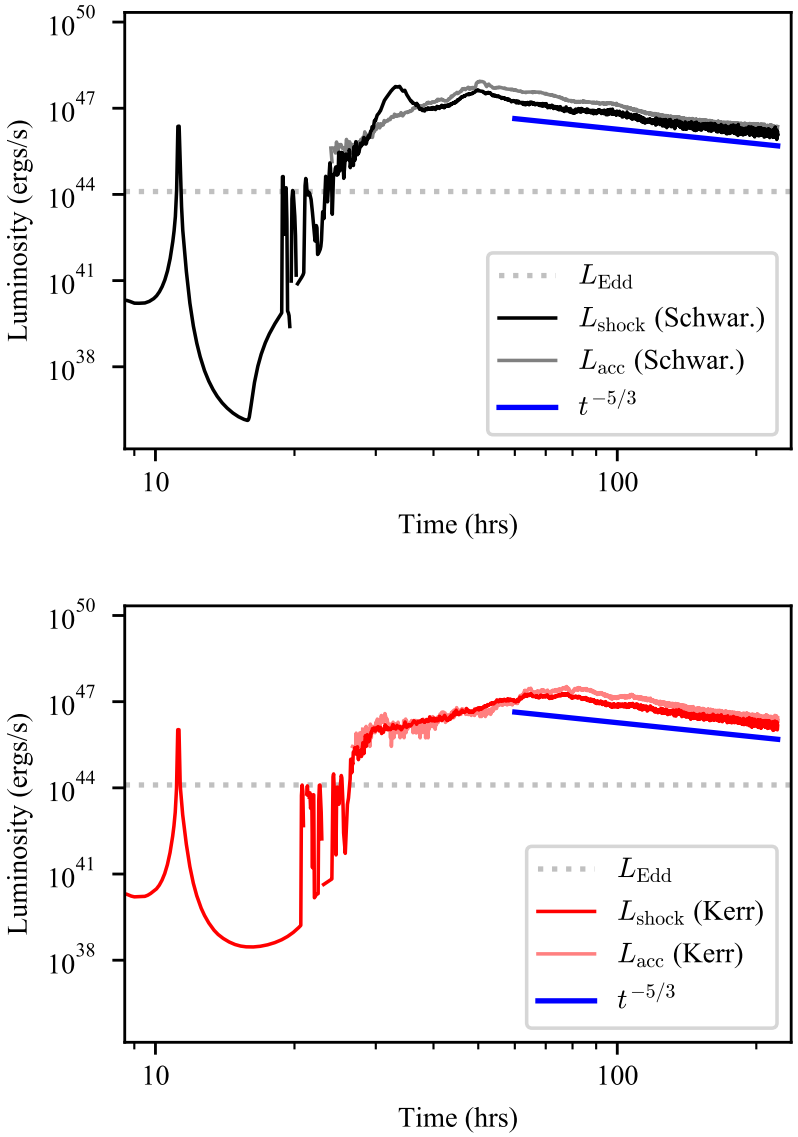

Figure 5.3: Energy injection rate ($L_{\rm shock}$) and accretion luminosity ($L_{\rm acc}$) for the adiabatic Schwarzschild (Sim. 1) and Kerr (Sim. 4) simulations shown in Figs. 5.1 and 5.2, and described in Sections 5.3.1 and 5.3.2. The spike at 11 hrs corresponds to the 'pancake' shock generated from the stellar compression during the first pericentre passage. Accretion only begins at $\sim$25–30 hrs, when material reaches pericentre a second time. $L_{\rm acc}$ roughly traces $L_{\rm shock}$ once accretion begins. The bump in $L_{\rm shock}$ for the Schwarzschild case (left) corresponds to the first stream-stream collision. We show a $t^{-5/3}$ slope for comparison, although this fallback rate is only expected for parabolic orbits. Dotted line shows the Eddington limit.

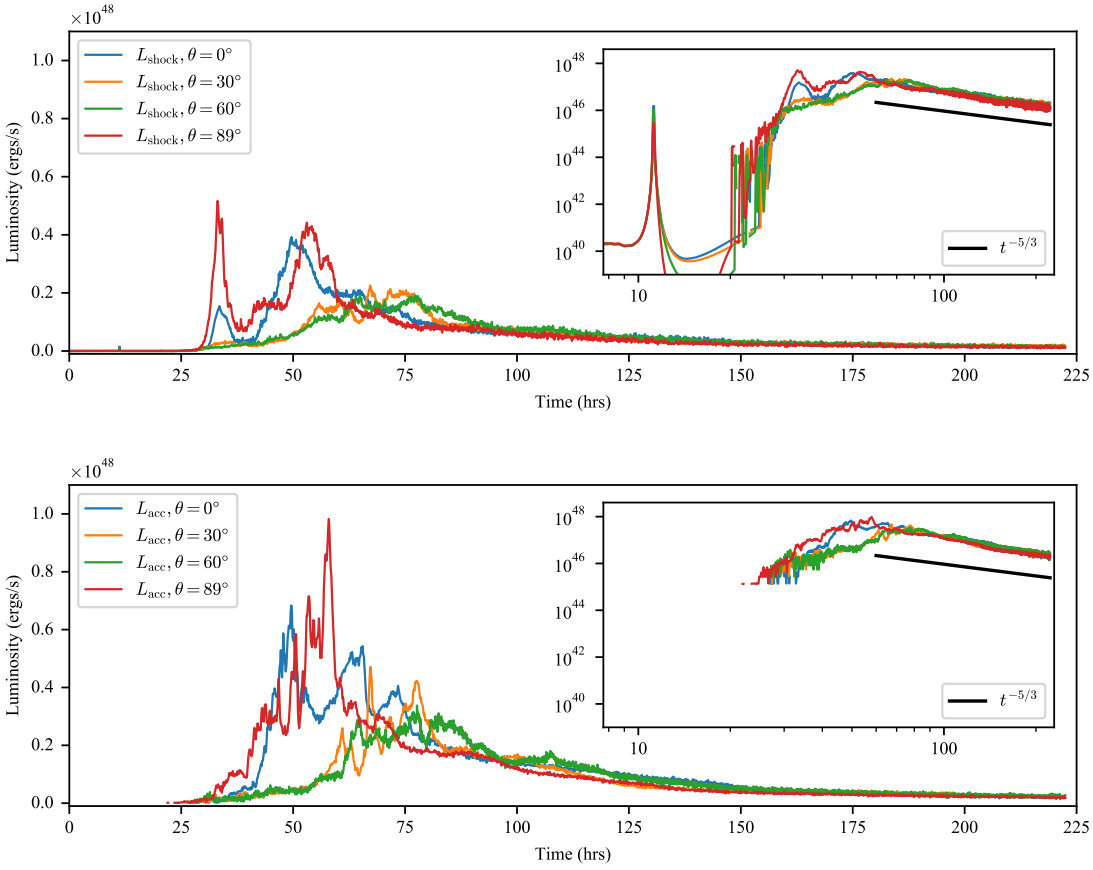

Figure 5.4: $L_{\rm acc}$ and $L_{\rm shock}$ for simulations 2, 3, 4 and 5 which differ only in their initial inclination angle. *Top:* luminosity from viscous heating and shocks. *Bottom:* luminosity from accretion. The same plots with log-log axes are shown as insets in each panel, along with a $t^{-5/3}$ slope for comparison.

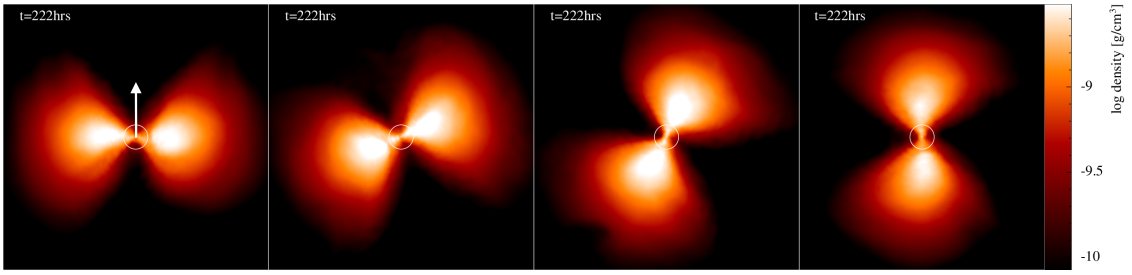

Figure 5.5: Cross sections of the final tori formed in simulations 2, 3, 4 and 5, taken through the planes defined by their total angular momentum vectors and the z-axis. Panels are 10 au $\times$ 10 au. The torus formed in each case has approximately the same inclination as the corresponding initial stellar orbit, i.e. $0°$, $30°$, $60°$ and $89°$ from left to right. We note that the angular momentum vector for the inclined calculations is 'twisted' about the z-axis due to Lense-Thirring precession by approximately $37°$, $42°$ and $43°$ for inclinations $30°$, $60°$ and $89°$ respectively. The black hole spin vector is shown by the arrow, and white circles indicates the tidal radius $R_{\rm t}$.

Fig. 5.2). However the head and tail of the stream still have a grazing encounter, since the stream has thickened with each pericentre compression, causing some material to begin circularising. During the third pericentre passage, the stream has thickened substantially and a low density cloud of material is already built up around the black hole. This causes all returning material to mildly shock and begin circularising. By 111 hrs most of the material has formed into a thick torus similar to the one formed around the Schwarzschild black hole, but inclined by approximately $60°$ to the x-y plane. Between 100 and 220 hrs, the torus precesses about the black hole spin axis by roughly $4°$, corresponding to a precession period of 450 days.

5.3.3 Energy injection rate

Figure 5.3 compares $L_{\rm acc}$ and $L_{\rm shock}$ in Simulations 1 and 4. The sharp spike of $\sim 10^{46}$ erg s^{-1} at approximately 11 hours corresponds to the heating generated by the pancake shock as the star passes through an effective nozzle at pericentre, which compresses the star in the direction perpendicular to its motion. The non-rotating case shows a steeper rise than the rotating case, with a distinct peak at 33 hours in the shock luminosity, corresponding to the stream-self intersection. This peak is absent in the rotating case because the stream does not self-intersect at that time. After 50 hours the energy injection rate reaches a maximum in the non-rotating case, then steadily declines as a power law. The maximum heating in the rotating simulation is reached slightly later at approximately 80 hours, before steadily declining. This turnover, in both cases, corresponds roughly to the disc/torus formation phase. We show the canonical $t^{-5/3}$ slope for comparison during the decay, although this trend is expected only for stars on initially parabolic orbits. Once accretion begins, $L_{\rm acc}$ roughly traces $L_{\rm shock}$ throughout the rest of the simulation. This is not altogether surprising since $L_{\rm shock}$ includes both viscous heating and shock heating due to stream-stream collisions, which are the two processes that can drive accretion. Furthermore, the contribution to $L_{\rm shock}$ is dominated by particles at the accretion radius. We discuss this further in Section 5.4.

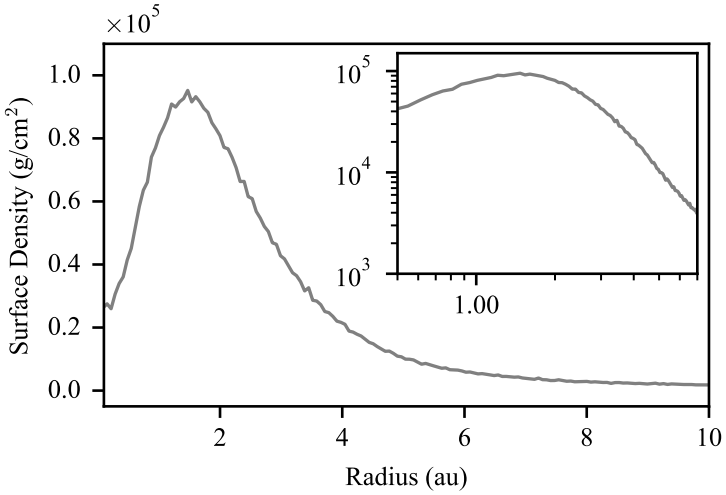

Figure 5.6: Surface density as a function of radius for Simulation 2. Inset shows the same plot with log-log axes. We measure the surface density profile to be roughly $\propto r^{-2.9}$ in the outer part of the disc.

5.3.4 Misalignment angle

Figure 5.4 compares $L_{\rm acc}$ and $L_{\rm shock}$ between simulations 2, 3, 4 and 5, which vary only in their inclinations, $0°$, $30°$, $60°$ and $89°$, respectively, around a black hole with spin $a = 0.99$. For moderate inclinations ($30°$ and $60°$) the tidal stream avoids the first self-intersection episode that occurs at ~ 33 hrs in the other two simulations, shown by the spikes in $L_{\rm shock}$ at that time. However at the largest inclination of $89°$, we find that nodal precession does not prevent this first stream-stream collision.

We also find that the $0°$ and $89°$ simulations are brighter by approximately an order of magnitude during the early stages of the calculation, and form discs at ~ 75 hrs, roughly 1 orbital period earlier than the $30°$ and $60°$ calculations.

For increasing inclinations, the stellar orbits penetrate fractionally deeper leading to a larger degree of both apsidal and nodal precession. The deeper encounters also produce stronger shocks during the pericentre compression, which output more heat and thus cause thicker debris streams. For the $89°$ inclined orbit, the combination of these effects leads to a stream self-intersection episode that is brighter than even the $0°$ case, which suggests that stream-stream collision behaviour is not a simple function of inclination.

5.3.5 Remnant disc properties

Figure 5.5 shows cross-sections of the discs/tori formed at the end of calculations 2, 3, 4 and 5. We find that each disc has approximately the same inclination as its corresponding initial stellar orbit, and that more inclined orbits have their angular momentum vectors 'twisted' about the z-axis by a larger degree due to Lense-Thirring precession.

The torus has a similar structure in each case. Since the gas cannot cool in these simulations the tori remain extended beyond the tidal radius, extending to a radius of roughly $500R_g$, or approximately 5 au, with an aspect ratio $H/R \sim 1$. Figure 5.6 shows the surface density profile

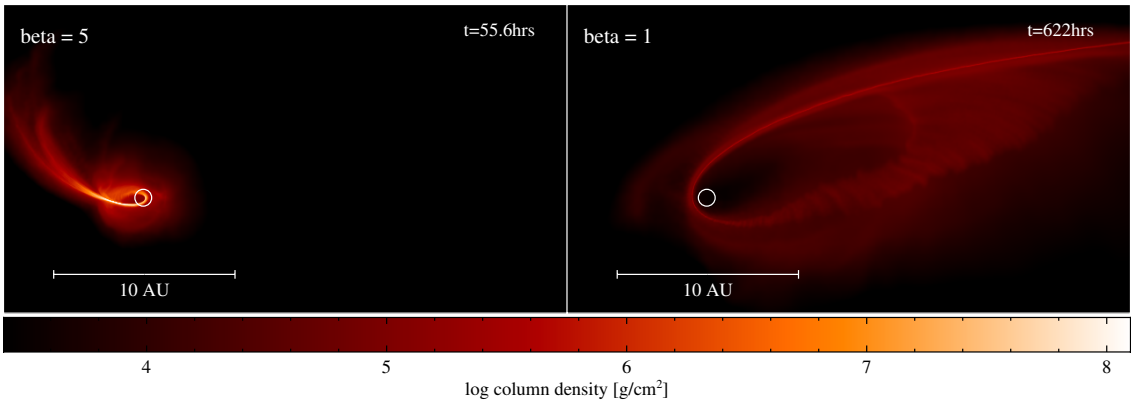

Figure 5.7: Snapshots of Simulations 4 and 6 after 2.5 orbital periods each, with penetration factors $\beta = 5$ and $\beta = 1$ (*left* and *right* panels respectively), projected in the initial orbital plane. The stream in the $\beta = 5$ simulation intersects close to the black hole, while for $\beta = 1$ it intersects at apoapsis where the stream has a low density and low velocity. White circle indicates the tidal radius $R_{\rm t}$.

of Sim. 2 at $t = 222$ hrs, computed in the manner of Lodato and Price (2010). That is, we bin particles by cylindrical radius into annuli, take the mass of each annulus and then divide by their cross-sectional area. The surface density has a peak of $\approx 9 \times 10^4$ g cm^{-2} at $r \approx 1.5$ au, and decays as a power law roughly $\propto r^{-2.9}$ in the outer part of the disc.

5.3.6 Penetration factor

Figure 5.7 compares snapshots of simulations 4 and 6 with $e = 0.95$, $a = 0.99$ and $\theta = 60°$, after 2.5 orbits each, where only the penetration factor β is varied between the two calculations. Figure 5.8 shows $L_{\rm acc}$ and $L_{\rm shock}$ as a function of the number of orbital periods. The orbital period for $\beta = 1$ is $5^{3/2} \approx 11$ times that of $\beta = 5$, thus disc formation happens much more rapidly for higher β. However, they both take approximately the same number of orbits ($\sim 4 - 5$) to circularise.

In the deep encounter, the tidal stream undergoes a higher degree of both apsidal and nodal precession. This causes the stream to have an eventual self-intersection at a few periapsis radii from the black hole, and to form a torus in a plane that is different to the initial orbital plane (but with the same inclination). The stellar debris for the $\beta = 1$ case, however, remains largely in the same orbital plane in which it started. Furthermore, it self-intersects almost at apoapsis, where the relative velocities between the head and tail are small and the debris is tenuous. As a consequence, the heating rate is 2 orders of magnitude fainter over the course of the simulations, and the final torus is ~ 5 times greater in size than the $\beta = 5$ case, extending to a radius of roughly $2500 R_g$ (approximately 25 au, or 1.4 times the initial apoapsis).

The radius of self-intersection in both cases is roughly consistent with the analytical prediction of Bonnerot et al. (2017b), but is difficult to measure accurately since the stream spreads after its periapsis passage.

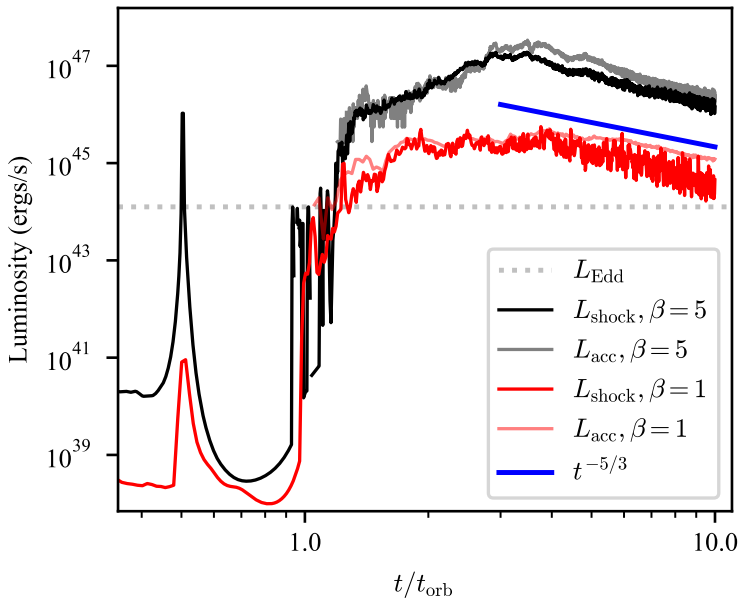

Figure 5.8: $L_{\rm acc}$ and $L_{\rm shock}$ for simulations 4 and 6 which differ only in their penetration factor β. Although the orbital period $t_{\rm orb}$ for $\beta = 1$ is approximately 11 times that of $\beta = 5$, their behaviour is similar as a function of the number of orbits. The energy injection rate is approximately 2 orders of magnitude greater for $\beta = 5$ throughout the simulation. Dotted line shows the Eddington limit.

5.3.7 Radiative efficiency

To investigate the influence of cooling on the disc formation process we repeated the simulations from Section 5.3.1 and 5.3.2 but with an isentropic approximation as described in Section 5.2.3. This corresponds to efficient radiative cooling, while still allowing for (reversible) heating due to compressive $P\mathrm{d}V$ work.

Figure 5.9 shows the evolution of Simulation 7 in which the black hole is non-rotating. Figure 5.10 shows the equivalent calculation around a Kerr black hole with spin $a = 0.99$ and initial orbital inclination $\theta = 60°$ (Simulation 8). Since the heat generated from viscosity and shocks is no longer contained within the gas, the tidal streams in the isentropic calculations remain thinner than in the adiabatic ones. They also form a small, thin ring at the end of the calculation close to the periapsis radius, in contrast to the large, thick tori produced by the adiabatic calculations. The peak energy injection and accretion luminosities produced by the isentropic calculations are also roughly 2 orders of magnitude brighter than their adiabatic counterparts, as shown in Figure 5.11.

In the Schwarzschild case there is one self-intersection, which very quickly circularises nearly all of the material into a thin ring in the x-y plane by ~ 43 hrs at a radius approximately twice the pericentre distance. This is consistent with the circularisation radius $r_{\rm c} = (1 + e)r_{\rm p}$ predicted from the conservation of angular momentum for Keplerian orbits (Bonnerot et al., 2016). At this point, the black hole enters a state of roughly constant accretion, shown by the plateau in the left panel of Figure 5.11.

In the Kerr simulation, a direct self-intersection is avoided but a grazing encounter between the head and tail still causes some material to lose orbital energy and build up close to the black

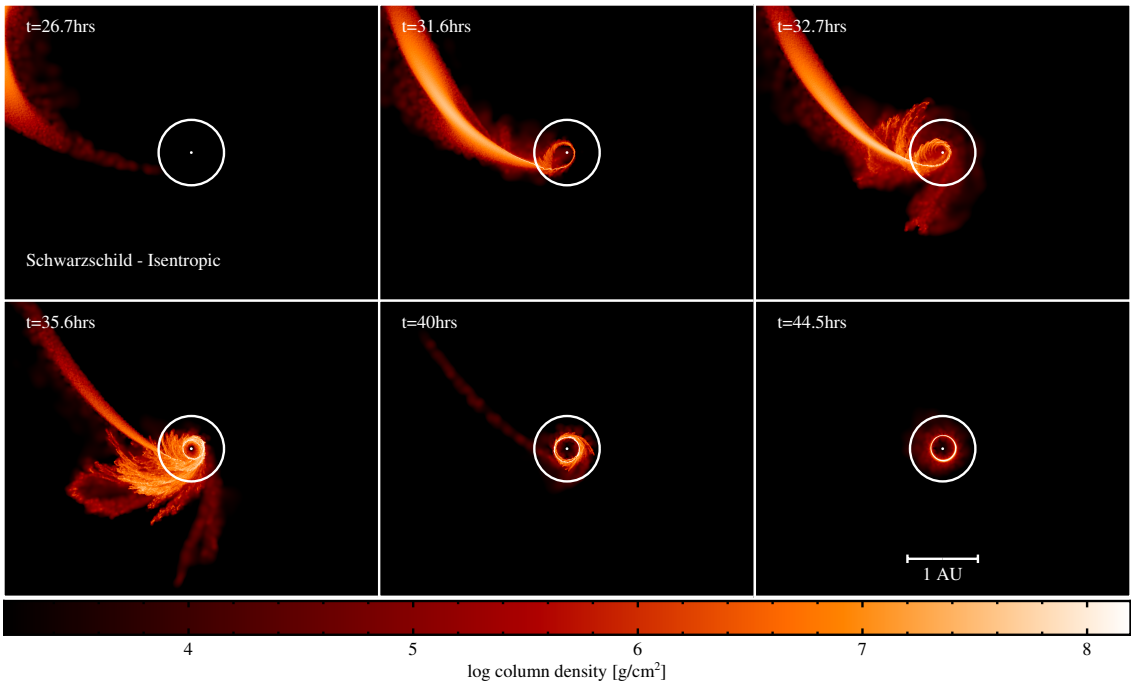

Figure 5.9: Snapshots of the debris fallback projected in the x-y plane for the $e = 0.95$, $\beta = 5$, $\theta = 0°$, $a = 0$ isentropic simulation (Sim. 7). The debris stream remains much thinner than in the corresponding adiabatic calculation (Fig. 5.1) since energy from viscous and shock heating is discarded. A very narrow ring is formed quickly after self-intersection, at twice the periapsis radius. White circle indicates the tidal radius $R_{\rm t}$.

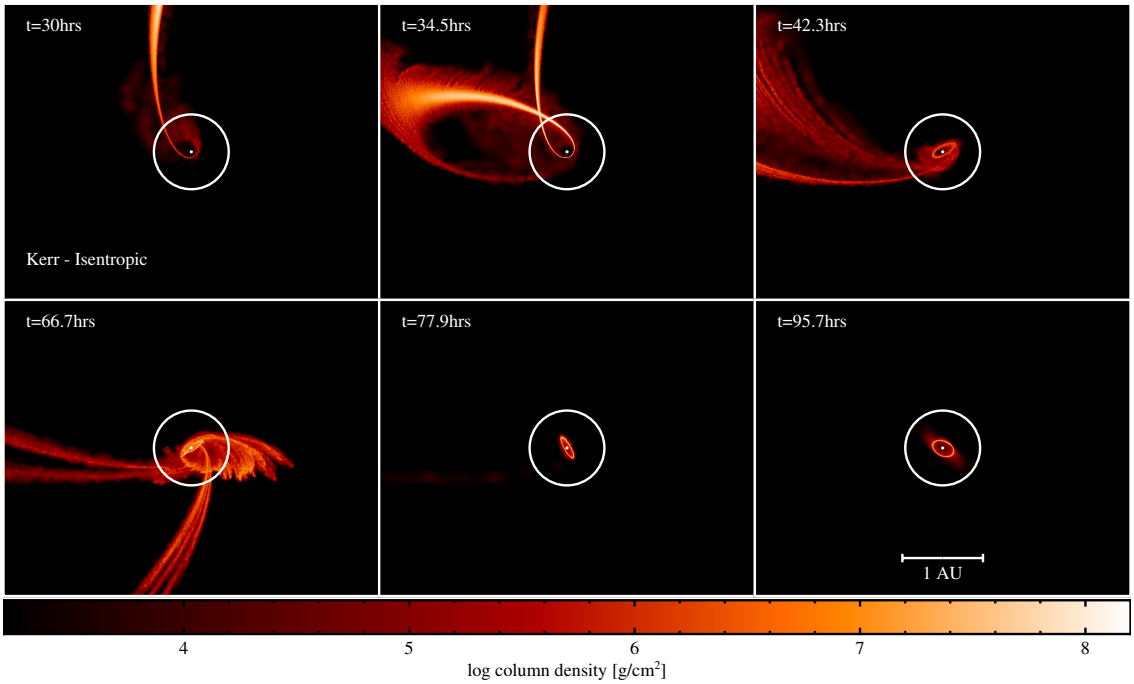

Figure 5.10: Snapshots of the debris fallback projected for the $e = 0.95$, $\beta = 5$, $\theta = 60°$, $a = 0.99$ isentropic simulation (Sim. 8), projected in the initial orbital plane. The stream avoids self-intersection after one orbit, but over subsequent orbits the stream circularises into a narrow ring at $\sim 1.6R_{\rm p}$ inclined by $\sim 50°$ to the black hole spin plane. The ring precesses about the black hole spin axis, completing ~ 4 revolutions between approximately 70 – 110 hrs, with a period of ~ 10 hours. White circle indicates the tidal radius $R_{\rm t}$.

hole, similar to the adiabatic calculations. As the rest of the stream returns to pericentre, transient rings of material are created and destroyed between ~ 40–70 hrs, approximately 8 times. This is reflected in $L_{\rm acc}$ and $L_{\rm shock}$ (Fig. 5.11 *right*) which take longer to reach a maximum than the Schwarzschild simulation and show multiple peaks between 40–70 hrs. Following this, most of the remaining material collects into a narrow ring inclined by $\sim 50^\circ$ to the black hole spin plane with a radius equal to roughly ~ 1.6 times the pericentre distance. Over the course of the next 40 hours, the ring precesses with a period of approximately 10 hours, completing 4 revolutions before being completely accreted by the black hole, shown by the final spike in $L_{\rm acc}$ and $L_{\rm shock}$ at ~ 110 hrs.

5.4 Discussion

We presented eight numerical GRSPH simulations testing the disc formation process from the tidal disruption of stars by rotating supermassive black holes. Hayasaki et al. (2013) were the first to demonstrate circularisation of the debris streams and formation of an accretion disc in numerical simulations. They showed that the main cause of circularisation is relativistic apsidal precession leading to self-intersection of the debris stream. Bonnerot et al. (2016) confirmed this using an improved pseudo-Newtonian potential, and further showed that the structure of the resultant disc depends on the cooling efficiency. Both studies performed SPH calculations in pseudo-Newtonian potentials and were not able to simulate spinning black holes. In our Schwarzschild metric calculations, using General Relativistic SPH without pseudo-Newtonian approximations, we confirm this basic picture — namely that relativistic apsidal precession leads to rapid debris circularisation.

Guillochon and Ramirez-Ruiz (2015) suggested that black hole spin would ruin this picture, since Lense-Thirring precession causes the debris stream to change plane and thereby avoid self-intersection (see also Hayasaki et al. 2016). Figure 5.2 shows that the stream indeed misses itself at the second pericentre passage (at $t = 33$ hrs), however, this is not fatal to disc formation because the stream does not miss by much. This is because nodal (spin-induced) precession is weak compared to apsidal (Schwarzschild) precession, meaning that the stream crossing occurs before nodal precession has time to move it significantly out of the plane. Hence the stream misses by only a few degrees. By the next orbit, the stream is already wide enough to successfully self-intersect and circularise, in contrast to the many dark windings of the stream implied by Guillochon and Ramirez-Ruiz (2015). The ‘dark year’ proposed by these authors is therefore bright.

We found that disc formation — at least for bound orbits — appears to be robust with regards to black hole spin and inclination. Although nodal precession of the debris stream’s orbital plane can prevent a direct self-intersection, the head and tail typically do not miss by much and still have a grazing encounter owing to their non-negligible cross-sections. As a consequence, the gas is shocked and rapidly circularises to form a thick torus as it does when the black hole is not rotating. However, the peak energy injection rate tends to be slower, and the rise time longer, than if the stream has a direct self-intersection.

As in Bonnerot et al. (2016), we found that the structure of the remnant disc depends strongly on the cooling efficiency. With no cooling (i.e. the adiabatic calculations), the debris settles into a thick and extended torus, while for radiatively efficient cooling (i.e. the isentropic calculations) a narrow ring is formed at a radius slightly greater than the pericentre distance. In both cases,

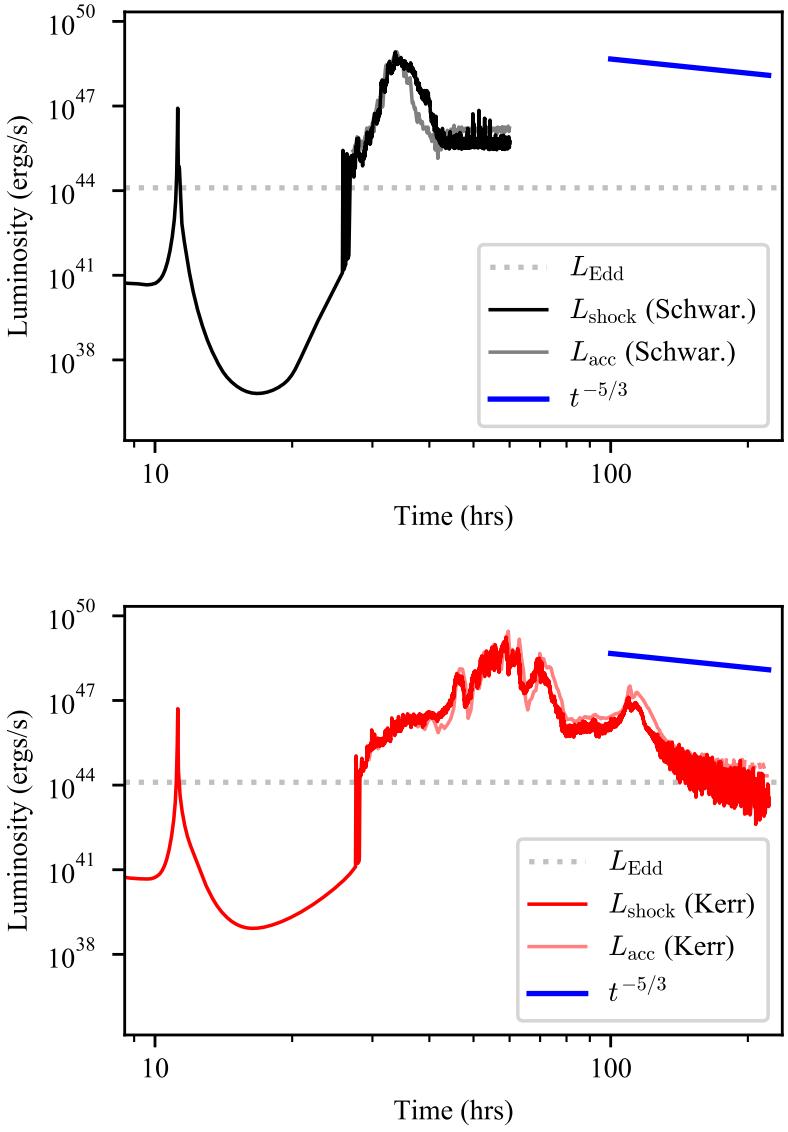

Figure 5.11: $L_{\rm acc}$ and $L_{\rm shock}$ for the isentropic Schwarzschild (Sim. 7) and Kerr (Sim. 8) simulations shown in Figs. 5.9 and 5.10, and described in Section 5.3.7. The peak luminosities are roughly 2 orders of magnitude greater than the corresponding adiabatic counterparts shown in Fig. 5.3. Dotted line shows the Eddington limit.

the remnant disc precesses about the black hole spin axis if it is misaligned. We estimated a precession period of approximately 10 hours for the ring and approximately 450 days for the torus, in the cases where $\theta = 60°$, $a = 0.99$, $\beta = 5$ and $e = 0.95$. The global precession period predicted by Franchini et al. (2016) for a rigidly precessing torus is between approximately 2 and 4 days around a $10^6 M_\odot$ black hole with spin $a = 0.99$. However, the disc properties considered by these authors differ from those of our remnant discs. Our discs extend to $\sim$ 5 au when $\beta = 5$, compared to their assumption of $R_{\rm out} = 2R_{\rm t}$ corresponding to $\approx$ 1 au. Since Lense-Thirring precession frequency scales as r^{-3}, this corresponds to a factor of $\sim$125 difference in precession timescale, which explains the discrepancy. The precession rate of the ring formed in our isentropic calculation is consistent with the Lense-Thirring rate at its radius ($\approx 15R_g$).

The peak luminosity and rise time of $L_{\rm acc}$ and $L_{\rm shock}$ depend strongly on the penetration factor β. This is because the orbital period is much shorter for orbits with high β, and the apsidal precession frequency is higher. As a consequence the stream self-intersects at a radius close to pericentre, leading to stronger shocks and faster circularisation. For deep $\beta = 5$ encounters, the typical peak luminosities are on the order of $\sim 10^{47}$ erg s^{-1}, taking several tens of hours to reach this peak after the first pericentre passage. This is roughly 3 orders of magnitude greater than the Eddington luminosity. In contrast, $L_{\rm acc}$ and $L_{\rm shock}$ in the $\beta = 1$ calculation are 2 orders of magnitude lower than with $\beta = 5$, and take $\sim$11 times longer to reach their peak. Thus the relative penetration depth may be inferrable from TDE observations.

Our remnant discs are larger than those shown in Bonnerot et al. (2016) by a factor of $\sim$2–3 ($\approx 5R_{\rm t}$ compared to their $\approx 2R_{\rm t}$, see their Fig. 8). This occurs because we consider a larger eccentricity of $e = 0.95$ compared to their calculation which used $e = 0.8$, implying greater orbital energy dissipation from the circularisation process. We confirmed that our $e = 0.8$ calculations produced similar disc sizes as those shown in Bonnerot et al. (2016). This suggests that even larger and hotter remnants would be produced in the parabolic case.

The initial pericentre passage is accompanied by a sharp spike in the energy injection rate ($L_{\rm shock}$), corresponding to the shocks produced by the 'pancaking' of the star during its periapsis compression. This has been predicted to be observable as a brief X-ray shock breakout with a peak luminosity between $\sim 10^{40}$–10^{43} erg s^{-1} (Kobayashi et al., 2004; Guillochon et al., 2009; Yalinewich et al., 2019), depending on the amount of energy lost as the shock moves out through the star. For $\beta = 5$, our calculations produce a spike of $\sim 10^{46}$ erg s^{-1}, 3–6 orders of magnitude greater than the predicted X-ray luminosity, however this is only the energy dissipation rate and not a true luminosity. Most of the thermal energy produced during pericentre compression is expected to remain trapped inside the star (Kobayashi et al., 2004) and thus would fail to radiate.

Most previous studies estimated the luminosity evolution simply from the predicted mass return rate (see studies that do not follow fallback in Section 5.1) or based on other assumptions about the dynamics of the stream's evolution (e.g. Bonnerot et al., 2017b). We computed the energy injection rate from first principles, based on either the irreversible energy dissipation rate or the accretion rate at $5R_g$ in our simulations. This approach is similar to Shiokawa et al. (2015) who estimated the heating rate by integrating the divergence of the heat flux in their calculations, however they were unable to distinguish between heating from reversible adiabatic compression and true entropy generation.

The evolution of $L_{\rm shock}$ shows features that may be identified with the energy release caused by the 'pancake shock', stream-stream collisions and viscous accretion (see Figs. 5.3, 5.4, 5.8 and 5.11). We found that the luminosity from shocks and viscous heating $L_{\rm shock}$ roughly traces the ac-

cretion luminosity $L_{\rm acc}$ in all our calculations. This is expected since $L_{\rm shock}$ does not distinguish between viscous dissipation and shock heating, which are the only two mechanisms available to reduce orbital energy and drive accretion. One might expect this to be a sign that material is being accreted ballistically (e.g. Svirski et al., 2017; Bonnerot et al., 2017b), however this is only true if the energy release is dominated by shocks at the location of stream self-intersection. In our calculations the heating rate is dominated by regions close to the accretion radius, suggesting that material is being accreted viscously.

A major caveat to our approach is that our simulations do not include radiation transport. We instead perform calculations in which the gas is either completely adiabatic or isentropic. Although these are two extreme regimes — since adiabatic calculations trap all heat while the isentropic calculations instantly remove heat produced by shocks and viscous heating — they provide upper and lower bounds to the true behaviour. Since the energy generation rate is super-Eddington, most of the energy cannot be transported as radiation and must instead be transported via mechanical outflows. This is precisely what we find in the adiabatic calculations. Our remnants in this case are likely closer to the truth, in the sense that the bulk of the energy goes into gas heating and kinematics, and the gas is not able to radiatively cool. Furthermore, any photons radiated in shocks would take a long time to diffuse out through optically thick material (e.g. Loeb and Ulmer, 1997; Roth et al., 2016), and be reprocessed into different wavelengths, possibly carrying information about the outflow geometry (e.g. Nicholl et al., 2019; Leloudas et al., 2019).

The energy injection and accretion rates we calculate are only approximations to the true light curve, particularly in the adiabatic case where $L_{\rm shock}$ represents the energy generation rate, and not the radiated luminosity. For the isentropic calculations however, discarded shock heating does genuinely reflect energy emitted from the gas. Our $L_{\rm acc}$ simply tracks the mass flux at $r = 5R_g$, which may either produce radiation or simply be advected into the black hole. Computing the true luminosity evolution is beyond the scope of this paper, since it would require the development of a General Relativistic radiation hydrodynamics scheme (e.g. Dai et al., 2018).

We also do not include magnetic fields in our calculations, which are thought to be important in the dynamics of TDEs (Bonnerot et al., 2017b,a; Svirski et al., 2017). In particular, the magneto-rotational instability (MRI) is thought to be the mechanism driving disc accretion. In our calculations disc accretion is driven by numerical viscosity, which is resolution dependent — in particular, it is higher at lower resolutions. As a consequence, the black hole accretion rate may be overestimated and thus the lifetime of the disc underestimated (see Appendix B.1).

Since the parameter space is already large for this problem, we focused on only prograde orbits. We also did not consider stellar spin (Golightly et al., 2019; Sacchi and Lodato, 2019), or stellar structure (Lodato et al., 2009), both of which have been shown to affect the fallback rate. The largest caveat of all is that we restricted our simulations to bound orbits.

5.5 Conclusion

We presented general relativistic numerical simulations of the tidal disruption of stars on bound orbits by SMBHs. Our calculations self-consistently employed relativistic hydrodynamics in the Kerr metric along with energy injection rates calculated from the irreversible dissipation in the gas and the mass accretion rate onto the black hole. Our key findings are as follows:

1. Nodal precession due to black hole spin does not prevent disc formation in TDEs, merely

causing a short delay.

2. Radiatively efficient cooling produces a narrow ring of orbiting material, while no cooling produces an extended, thick torus. Lense-Thirring precession causes the remnant disc in both cases to precess about the black hole spin axis.

3. Thick discs/tori can be formed robustly with the same inclination as the initial stellar orbit. They have an aspect ratio of ~ 1, surface density profiles roughly $\propto r^{-3}$, and extend to of order the apoapsis radius.

4. TDEs with high penetration factors are significantly more luminous and produce discs faster than those with a lower penetration factor. We find $\beta = 5$ TDEs to have energy injection rates ~ 2 orders of magnitude greater than TDEs with $\beta = 1$.

Whether or not these results extend to stars disrupted on parabolic orbits remains to be investigated.

Chapter 6

Eddington envelopes: The fate of stars on parabolic orbits tidally disrupted by supermassive black holes

Stars falling too close to massive black holes in the centres of galaxies can be torn apart by the strong tidal forces. Simulating the subsequent feeding of the black hole with disrupted material has proved challenging because of the range of timescales involved. Here we report a set of simulations that capture the relativistic disruption of the star, followed by one year of evolution of the returning debris stream. These reveal the formation of an expanding asymmetric bubble of material extending to hundreds of au — an Eddington envelope with an optically thick inner region. Such envelopes have been hypothesised to explain optical/UV emission in tidal disruption events, but never produced self-consistently. Our model broadly matches the observed light curves with low temperatures, faint luminosities, and line widths of 10,000–20,000 km/s.

6.1 Introduction

In the classical picture of tidal disruption events (TDEs), the debris from the tidal disruption of a star on a parabolic orbit by a supermassive black hole (SMBH) rapidly circularises to form an accretion disc via relativistic apsidal precession (Rees, 1988). The predicted mass return rate of debris is $\propto t^{-5/3}$ (Phinney, 1989) and the light curve is assumed to be powered by accretion and to follow the same decay.

This picture alone does not predict several properties of observed TDEs, mainly related to their puzzling optical emission (van Velzen et al., 2011; van Velzen, 2018). These properties include: i) low peak bolometric luminosities of $\sim 10^{43}$–$10^{44.5}$ ergs s^{-1} (Hung et al., 2017; van Velzen et al., 2020), ~ 1 per cent expected from radiatively efficient accretion (Piran et al., 2015; Stone and Metzger, 2016; Svirski et al., 2017); ii) low temperatures, more consistent with the solar photosphere than with that of an accretion disc at a few tens of gravitational radii ($R_g \equiv GM_{\rm BH}/c^2$) (Gezari et al., 2012; Miller, 2015), and consequently large emission radii, $\sim$10–100 au for a $10^6 M_\odot$ black hole (Guillochon et al., 2014; Metzger and Stone, 2016); and iii) spectral line widths implying gas velocities of $\sim 10^4$ km s^{-1}, much lower than expected from an accretion disc (Arcavi et al., 2014; Leloudas et al., 2019).

As a consequence, numerous authors have proposed alternative mechanisms for powering the TDE lightcurve via: i) distant shocks from tidal stream collisions during disc formation (Lodato, 2012; Piran et al., 2015; Svirski et al., 2017); ii) the reprocessing of photons through a large scale optically thick 'Eddington envelope' or 'radiation-dominated nebula', which can be either quasistatic (Loeb and Ulmer, 1997; Guillochon et al., 2014; Coughlin and Begelman, 2014; Roth et al., 2016) or outflowing (Strubbe and Quataert, 2009; Metzger and Stone, 2016; Roth and Kasen, 2018; Bonnerot and Lu, 2019); or iii) thermal winds, which mechanically transport radiation trapped by electron scattering close to the black hole to larger radii (Strubbe and Quataert, 2009; Lodato and Rossi, 2011). But without first principles calculations, it is difficult to test any of these hypotheses.

The wider problem is that no first principles calculations exist. The challenge is to evolve a main-sequence star on a parabolic orbit around a SMBH from disruption to follow the subsequent accretion of material (Metzger and Stone, 2016). The dynamic range involved when a $1M_{\odot}$ star on a parabolic orbit is tidally disrupted by a $10^6 M_{\odot}$ SMBH is greater than four orders of magnitude: the tidal disruption radius is 50 times the gravitational radius, where general relativistic effects are important, while the apoapsis of even the most bound material is another factor of 200 further away. This challenge led previous studies to consider a variety of simplifications (Stone et al., 2019): i) reducing the mass ratio e.g. by considering intermediate mass black holes (Ramirez-Ruiz and Rosswog, 2009; Guillochon et al., 2014) and/or considering the disruption of white dwarfs (Rosswog et al., 2008; Shiokawa et al., 2015; Frolov et al., 1994); ii) using a Newtonian gravitational potential (Evans and Kochanek, 1989; Rosswog et al., 2008; Lodato et al., 2009; Guillochon et al., 2009; Golightly et al., 2019) or post-Newtonian approximations (Ayal et al., 2000; Hayasaki et al., 2013, 2016); iii) simulating only the first passage of the star (Evans and Kochanek, 1989; Laguna et al., 1993; Khokhlov et al., 1993; Frolov et al., 1994; Diener et al., 1997; Kobayashi et al., 2004; Guillochon et al., 2009; Guillochon and Ramirez-Ruiz, 2013; Tejeda et al., 2017; Gafton and Rosswog, 2019; Goicovic et al., 2019); and iv) assuming stars on bound, highly eccentric orbits instead of parabolic orbits (Sadowski et al., 2016; Hayasaki et al., 2016; Bonnerot et al., 2016; Liptai et al., 2019).

These studies have, nevertheless, provided useful insights into the details of the tidal disruption process. In particular, it has been shown that the energy spread following the initial disruption is roughly consistent with the analytic prediction leading to a $\propto t^{-5/3}$ mass fallback rate, although the details can depend on many factors such as stellar spin, stellar composition, penetration factor and black hole spin (e.g. Lodato et al., 2009; Kesden, 2012; Guillochon and Ramirez-Ruiz, 2013; Golightly et al., 2019; Sacchi and Lodato, 2019). The importance of general relativistic effects in circularising debris has also been demonstrated. The self-intersection of the debris stream, which efficiently dissipates large amounts of orbital energy, is made possible by relativistic apsidal precession (e.g. Hayasaki et al., 2016; Bonnerot et al., 2016; Liptai et al., 2019). But this has only been shown for stars on bound orbits, with correspondingly small apoapsis distances and often deep penetration factors.

In this paper, we present a set of simulations that self-consistently evolve a main-sequence star on a parabolic orbit around an SMBH from disruption to circularization and then accretion. We follow the debris evolution for one year post-disruption, enabling us to compute synthetic light curves from first principles which, to our astonishment, appear to match the key features of observations.

6.2 Method

We model the disruption of stars with mass $M_* = 1M_\odot$ and radius $R_* = 1R_\odot$ by a supermassive black hole with mass $M_{\rm BH} = 10^6 M_\odot$ using the general relativistic implementation of the smoothed particle hydrodynamics code PHANTOM (Price et al., 2018) as described in Liptai and Price (2019). We use the Kerr metric in Boyer-Lindquist coordinates, with the black hole spin vector along the z-axis, and assume an adiabatic equation of state for the gas. We delete from the simulation particles that fall within a radius of $R_{\rm acc} = 5R_g$ (within the innermost stable circular orbit of a non-spinning black hole) to avoid small timesteps close to the horizon.

We place the star on a parabolic orbit initially at a distance of $r_0 = 10R_{\rm t}$ with velocity $v_0 = \sqrt{2GM_{\rm BH}/r_0}$, where $R_{\rm t} = R_*(M_{\rm BH}/M_*)^{1/3}$ is the tidal radius. The parabolic trajectory is oriented such that the star travels counter-clockwise in the x-y plane, and that the Newtonian pericentre $R_{\rm p}$ is located on the negative y axis. For inclined trajectories, we rotate the initial position and velocity vectors by an angle θ about the y-axis. As in our previous paper (Liptai et al., 2019) we model the star as a polytropic sphere with adiabatic index $\gamma = 5/3$ using approximately 512K particles, we do not relax the star prior to beginning the calculation, and we include Newtonian self-gravity in our simulations to hold the star together during the pre-disruption phase. We define the penetration factor as $\beta \equiv R_{\rm t}/R_{\rm p}$. We note that the point of closest approach is typically smaller than the Newtonian pericentre $R_{\rm p}$ due to relativistic effects, and thus the 'true' penetration factor is larger (by up to ~ 1 in our $\beta = 5$ calculation, so that the true β is closer to 6).

6.3 Results

Figure 6.1 shows snapshots of the long-term debris evolution in our simulation where the black hole is rotating with spin $a = 0.99$ and the initial orbit of the star is prograde and inclined by 60° to the black hole equatorial plane. The penetration factor is $\beta = 1$, and the equation of state is adiabatic. The star takes approximately 7 hours to reach pericentre at which point it is tidally disrupted and forms a long, thin debris stream. Approximately half of the stream is bound while the other half is unbound (visible as the thin, dense upward stream in the figure). The head of the stream (i.e., the most bound material) takes ~ 26 days to return to pericentre. As the stream passes through pericentre for a second time, it drives the formation of a bubble of material, which spreads almost isotropically, eventually encasing the black hole. A fraction of the material joins the returning debris and returns to pericentre, however most of it goes into a low density mechanical outflow. Following the fallback for one year post disruption, we find that the bubble continues to expand, without circularising into a disc. This debris structure bears remarkable similarity to the 'Eddington envelope' first proposed by Loeb and Ulmer (1997), except that our envelope is expanding, while their model assumed an envelope in hydrostatic equilibrium.

Figure 6.2 shows the density (*top*), radial velocity (*middle*) and temperature distributions (*bottom*) of particles a year after disruption, the latter assuming a radiation pressure dominated flow. The density of the Eddington envelope is $\sim 10^{-16}$ g cm^{-3}, approximately 6 orders of magnitude lower than the density of the stream, which is $\sim 10^{-10}$ g cm^{-3}. The typical outflow velocity is $\sim 10^4$ km s^{-1}.

Figure 6.3 *top* shows the energy dissipation rate in our simulation, $L_{\rm shock}$ (cf. Liptai et al., 2019). This includes irreversible heating due to viscosity and shocks, and is dominated by re-

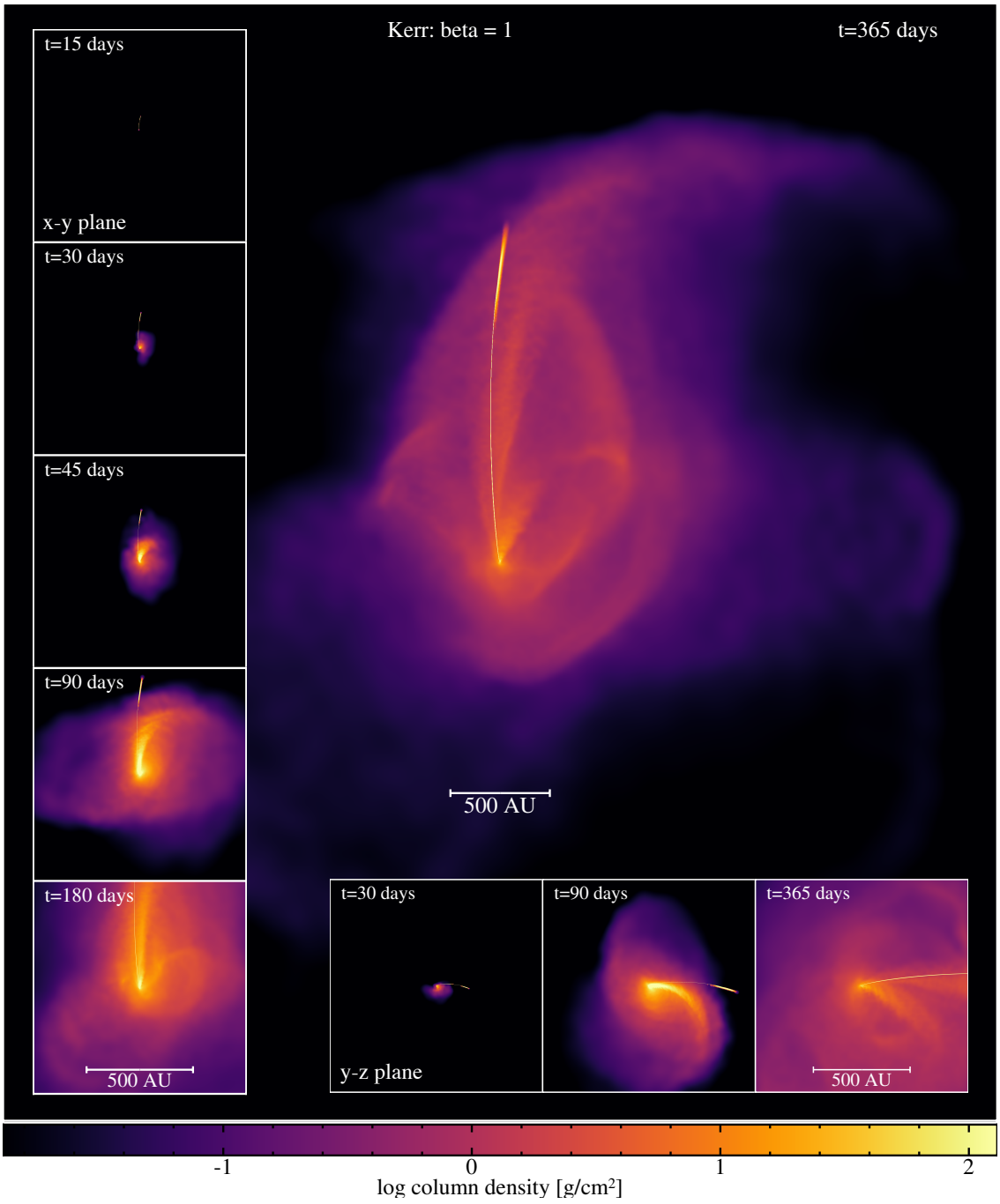

Figure 6.1: One year in the life of a tidal disruption event. We show shapshots of column density in the long-term debris evolution of a $1M_\odot$ star on a parabolic orbit with $\beta = 1$, disrupted by a $10^6 M_\odot$ Kerr black hole with spin $a = 0.99$. The initial orbital plane is misaligned by 60° to the black hole spin plane. *Main* panel shows the debris after 365 days projected in the x-y plane. Inset panels on the *left* show the evolution projected in the x-y plane, while inset panels on the *bottom* show the evolution projected in the y-z plane. The evolution is similar for tidal disruptions by a non-spinning (Schwarzschild) black hole.

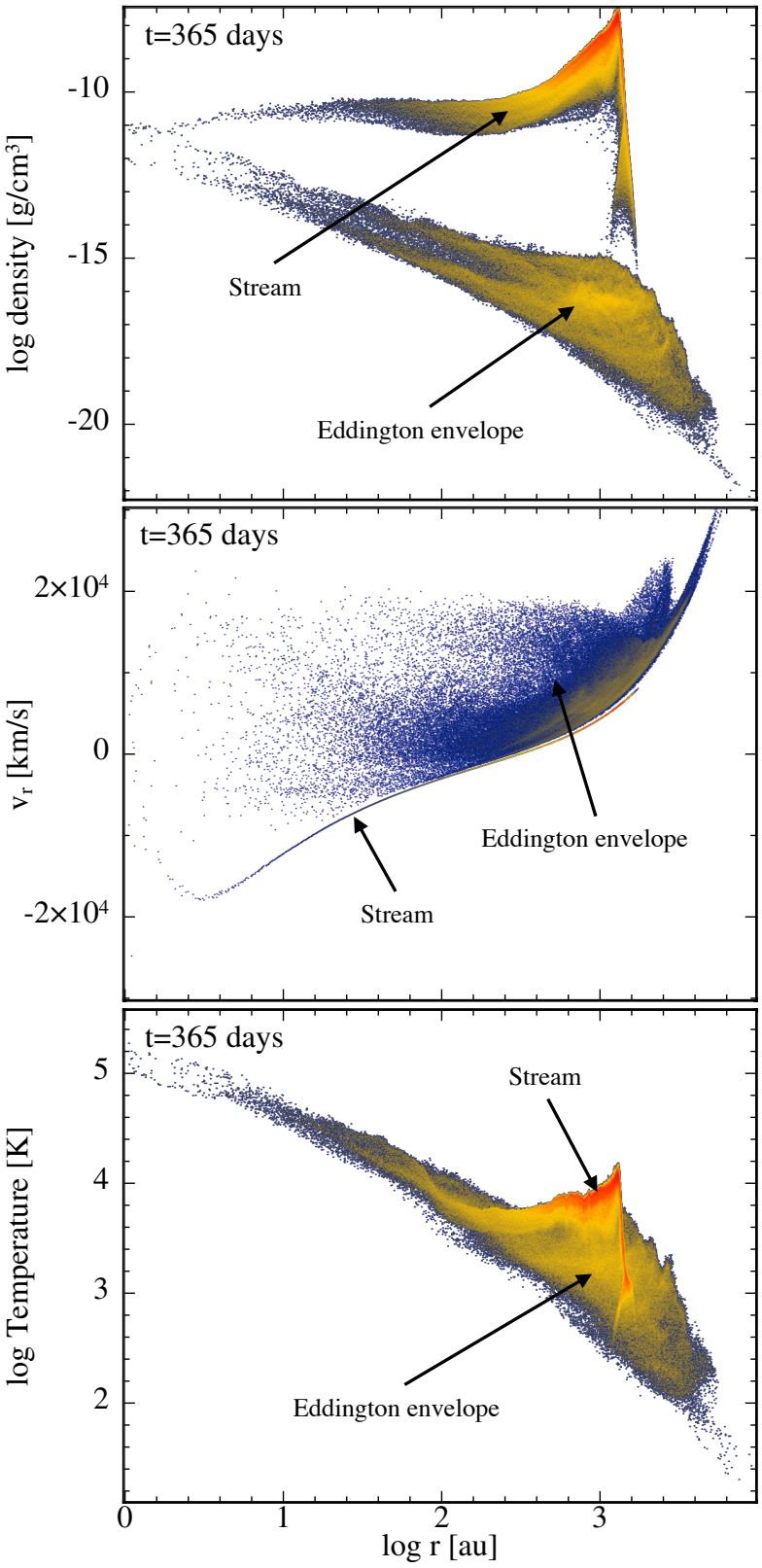

Figure 6.2: Distributions in density (*top*), radial velocity (*middle*) and temperature (*bottom*) at one year post disruption. Colours represent the density of points on the plot, with orange being a high number of points and blue being a low number. All three distributions show features that may be identified as the high density stream and the low density, cool, expanding Eddington envelope. Typical outflow velocities are of order 10^4 km s^{-1}, similar to those measured in observed TDE spectra and to the 'mass loaded outflows' predicted by Metzger and Stone (2016).

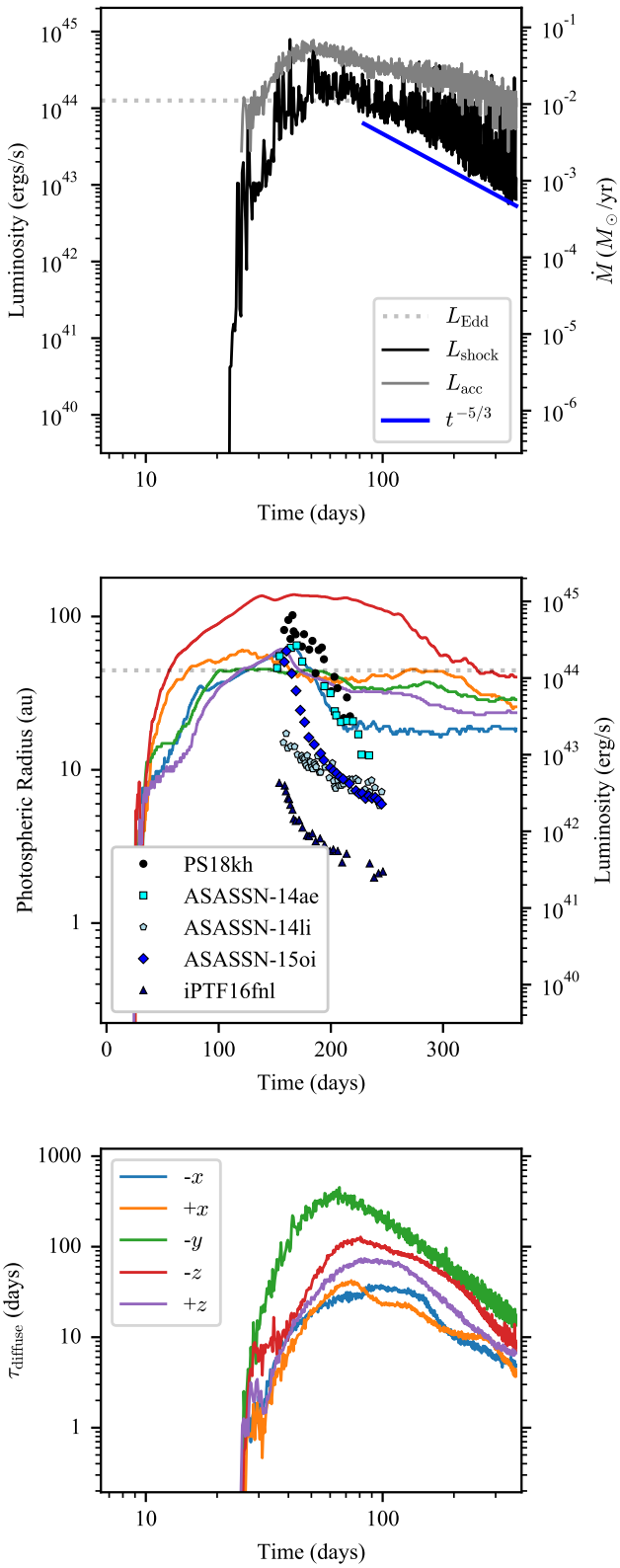

Figure 6.3: *Top:* Energy dissipation rate and accretion luminosity evolution, compared to the Eddington luminosity and a $t^{-5/3}$ slope. *Middle:* Photospheric radius evolution measured along different lines of sight and the corresponding isotropic luminosity, assuming a photosphere temperature of $10^{4.4}$ K. Markers represent the radius evolution of black body fits to various observed TDEs, as in Figure 11 of Holoien et al. (2019). *Bottom:* Estimated photon diffusion timescale along different lines of sight (see legend).

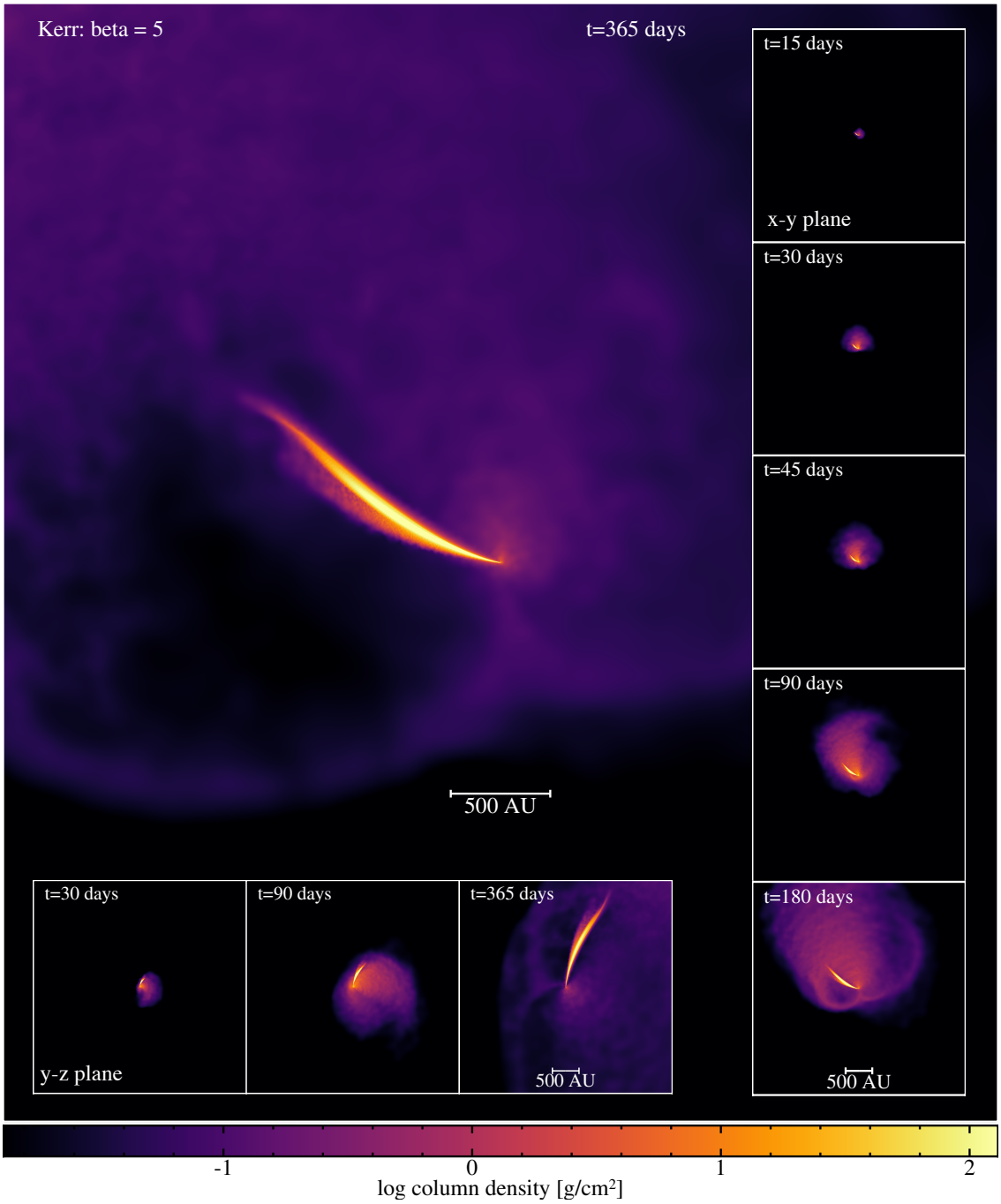

Figure 6.4: As in Figure 6.1, but for a star plunging closer to the black hole ($\beta = 5$). We show column density evolution for a $1M_\odot$ star on a parabolic orbit with $\beta = 5$, disrupted by a $10^6 M_\odot$ Kerr black hole with spin $a = 0.99$. The initial orbital plane is misaligned by 60° to the black hole spin plane. *Main* panel shows the debris after 365 days projected in the x-y plane. Inset panels on the *right* show the evolution projected in the x-y plane, while inset panels on the *bottom* show the evolution projected in the y-z plane.

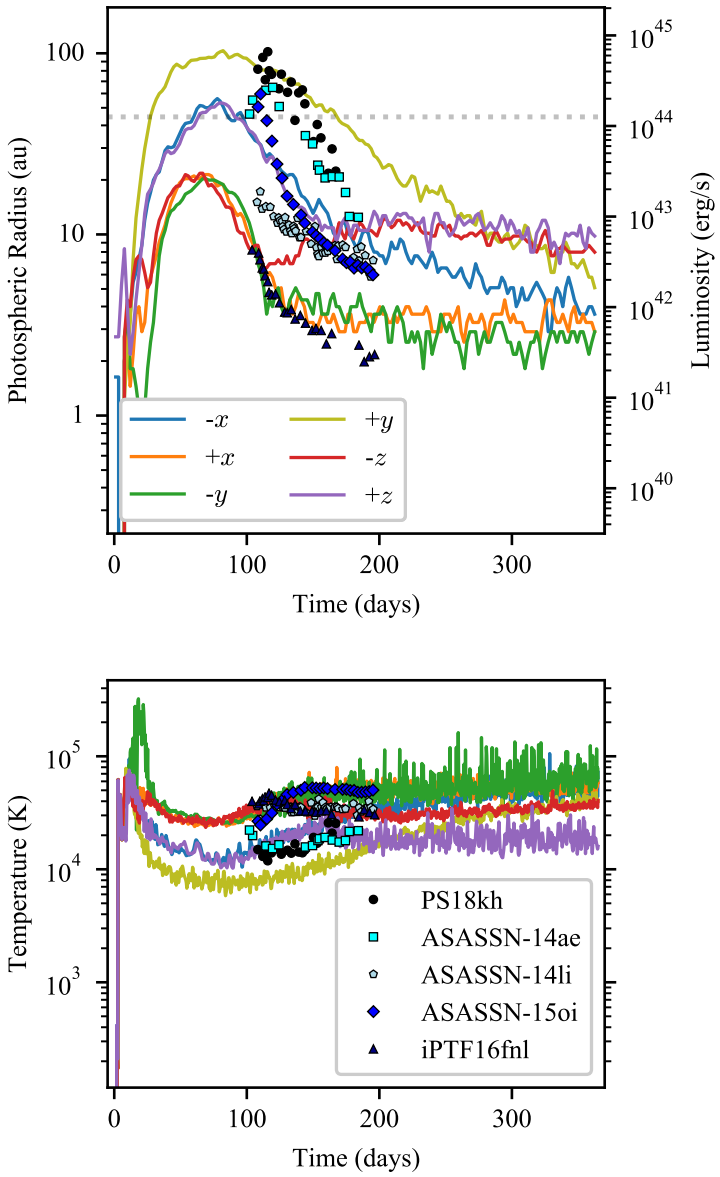

Figure 6.5: Photosphere radius and temperature evolution for a star plunging closer to the black hole with $\beta = 5$, measured along different lines of sight (see legend). The corresponding isotropic luminosity is shown in the secondary y-axis, assuming a photosphere temperature of $10^{4.4}$ K. Markers as in Figure 6.3 (*middle*) represent the radius and temperature evolution of black body fits to various observed TDEs (Holoien et al., 2019). Grey dotted line in top panel represents the Eddington luminosity.

gions close the accretion radius $R_{\rm acc}$. The energy dissipation rate rises rapidly from $\sim$26 days, when accretion begins, until $\sim$50 days after disruption when it reaches a peak of $\sim 10^{44}$ erg s^{-1} (roughly the Eddington limit). This is followed by a power law decay. We compare this to an effective luminosity derived from our measured mass accretion rate $\dot{M}$, given by $L_{\rm acc} = \epsilon \dot{M} c^2$. Here, $\epsilon = 0.2$ is the efficiency based on our inner accretion radius. The accretion luminosity follows the same trend as the energy dissipation rate, but is roughly 0.5–1 orders of magnitude greater throughout the simulation. This suggests that there is some material accreted almost radially, with little to no orbital energy dissipated before accretion (cf. Svirski et al., 2017).

Although most energy is dissipated in regions close to the black hole, where the reservoir of gravitational binding energy is largest, this material is optically thick. The energy is transported outward by mechanical outflows before some of it is radiated through a photosphere. In that sense, our model is closest to the 'super-Eddington outflows' of Strubbe and Quataert (2009) and Lodato and Rossi (2011).

Figure 6.3 *middle* shows the photospheric radius in our simulations computed along multiple lines of sight. We measured the photospheric radius $R_{\rm photo}$ by integrating along radial lines to the black hole until we reached an optical depth of unity. That is, we computed

$$\tau = \int_{R_{\rm photo}}^{\infty} \kappa \, \rho(r) \, dr, \tag{6.1}$$

integrating until $\tau = 1$, using $\kappa = 0.4$ g cm^{-2} as the electron scattering opacity in ionised hydrogen and neglecting the temperature dependence of opacity. We computed Equation 6.1 by integrating 1920 discrete pixel values along each coordinate axis from $\pm$1390 au. We omitted the integration along the positive y axis since this particular line of sight crosses the high density stream and thus does not accurately represent the photospheric radius of the Eddington envelope. The photosphere radius varies between $\sim$20–100 au depending on the line of sight. It reaches a peak after roughly 150 days. We compare the evolution of our measured $R_{\rm photo}$ to the radius evolution of several observed TDEs inferred from black body fits (taken from figure 11 of Holoien et al. 2019 and shifted by 150 days to match the approximate peak in our calculations). The radii from PS18kh and ASASSN-14ae agree with our measured radii, while ASASSN-14li, ASASSN-15oi and iPTF16fnl are smaller by a factor of a few. We also show the approximate isotropic-equivalent luminosity along the same lines of sight on the secondary y-axis, computed by assuming black-body emission from the photosphere and neglecting photon diffusion from sub-photosphere layers. We assume a constant temperature of $T = 10^{4.4}$ K, which is the typical value in the observed TDEs (see figure 10 of Holoien et al. 2019). This is consistent with the prediction from our simulations, obtained by setting the energy density of the radiation, which should dominate the energy and pressure balance, equal to the simulated energy density of the nominally adiabatic gas which does not cool in our simulations. The typical luminosity is around 10^{43}–10^{44} erg s^{-1} ($10^{9.4}$–$10^{10.4}$ $L_\odot$), however we caution that the exact value is sensitive to the chosen temperature (since $L \propto T^4$). Nonetheless, our approximate luminosities are consistent with the observed values (see figure 9 of Holoien et al. 2019), as well as with the analytically computed light curves of Lodato and Rossi (2011) (see left panel of their Figure 7).

Figure 6.3 *bottom* shows the approximate time taken for photons to diffuse from near the black hole out to the photosphere radius, assuming the material remains static. We computed this

using (e.g. Mitalas and Sills, 1992)

$$\tau_{\rm diffuse} \approx \frac{6\pi}{c} \int_0^{R_{\rm photo}} \kappa\, r\, \rho\, dr, \tag{6.2}$$

using 1920 discrete pixels from 0 to ± 200 au along each coordinate axis (again neglecting the $+y$ axis). The typical photon diffusion time varies between $\sim$10–200 days, peaking approximately 80 days after disruption and decaying roughly as a power law.

Figure 6.4 shows snapshots of the debris fallback for a calculation with an increased penetration factor of $\beta = 5$. Since the star approaches much closer to the black hole, the effects of apsidal and Lense-Thirring precession throw the star/debris stream into an orbital plane that is different to the initial one. This changes the debris geometry projected in each coordinate plane, however the overall picture remains unchanged. That is, the returning debris stream feeds the expansion of a low density Eddington envelope as in the $\beta = 1$ case.

Figure 6.5 shows the evolution of $R_{\rm photo}$ in the $\beta = 5$ case measured along multiple lines of sight. We again compare our results to the radius evolution of observed TDEs from Holoien et al. (2019), shifted by 100 days. The radii from observations match remarkably well with our measured radii. The photosphere evolves faster than in the $\beta = 1$ simulation, with the radius (and luminosity) peaking $\sim$75 days after disruption, i.e., approximately a factor of two earlier. The typical radius and luminosity are also lower, which may help explain under-luminous TDEs such as iPTF16fnl.

A notable feature in both the $\beta = 1$ and $\beta = 5$ cases are the almost flat lightcurves and photosphere temperatures predicted at late times along most lines of sight. This is also seen in the observations (e.g. Hung et al., 2017; Holoien et al., 2019). In our simulations this corresponds to the stalling of the photospheric radii in a steadily expanding gas cloud that has roughly reached a steady-state structure in the inner regions; however, as discussed below, our models without cooling do not accurately describe light curves at late times.

6.4 Discussion

Our main new insight from the parabolic case is that we have been able to self-consistently form the hypothesised 'Eddington envelope' for the first time, more or less as predicted by Loeb and Ulmer (1997). With the disrupted star moving on an orbit with a mean energy of zero and low angular momentum, we found that the dissipation of energy and angular momentum through relativistic precession and ensuing stream-stream collisions was not efficient in circularising material at small separations necessary to allow accretion. Instead, we find numerically (and explain analytically in section C.3) that the gradual density contrast and slow mass return rates at the leading edge of the returning stream enable efficient redistribution of energy.

Once accretion commences in the very optically thick environment with inefficient cooling (we assume adiabatic gas), the gravitational energy of accreting material launches mechanical outflows, yielding a large, asymmetric, optically thick Eddington envelope.

Whether or not a disc is formed is largely irrelevant to this picture (re-examining our calculations of initially eccentric encounters (Liptai et al., 2019), we find a similar envelope, but with faster outflows $\sim 5 \times 10^4$ km/s instead of our $\sim 2 \times 10^4$ km/s). Neither disc formation nor disc accretion plays a role in the formation of this envelope (Metzger and Stone, 2016). The structure is broadly similar to other rapidly expanding, optically thick, quasi-spherical outflows powered by

a central energy source, such as supernovae and kilonovae. In this case, the expanding envelope is powered by gravitational energy, dissipated in the radiatively inefficient accretion flow onto the black hole (our black hole mass accretion rate, shown in the top panel of Figure 6.3, is 1–1.5 orders of magnitude lower than the predicted mass fallback rate). This broad conclusion on the formation of an Eddington envelope is unchanged by whether or not the black hole is spinning, or by whether the star approaches closer to the black hole (see Figure 6.4). We confirmed the robustness of this conclusion to the resolution of the simulation (see section C.1).

That our Eddington envelope, or 'black hole sun', is optically thick is demonstrated by our estimated photon diffusion timescales of $\sim$ 10–100 days shown in the bottom panel of Figure 6.3. This means that the debris produced by the disruption cannot cool efficiently, leading to the formation of a photosphere. We computed the radius of this photosphere along different lines of sight to a distant observer, finding a photosphere of radius $\sim$ 10–100 au ($\sim 10^3$–$10^4 R_g$) that expands and contracts with time. Comparing these radii to photospheric radii inferred from observed tidal disruption events shows a remarkable agreement, particularly in the simulation with higher penetration factor. This is surprising, since in no sense have we attempted to tune our simulation parameters to match any particular observation.

We employed an adiabatic approximation, meaning that none of the energy produced is actually radiated in our simulations. This is likely a good approximation at early times (near the peak of the light curve) since the photon diffusion timescale is long, although it does not account for the change to the radiation-pressure dominated regime after shock heating, which implies that the adiabatic index should change to $4/3$. On the other hand, the adiabatic assumption likely breaks down by around 1 year after disruption. At late times, our estimated luminosity becomes comparable to the energy input rate from shock heating (top vs. middle panels of Figure 6.3), while the diffusion timescale drops to a small fraction of a year, allowing photons to escape and the gas to cool. Therefore, at these late times, with relatively efficient diffusion, the observable luminosity should transition to tracking the shock heating rate, which in turn roughly tracks the mass return rate with $\propto t^{-5/3}$ scaling (top panel of Figure 6.3). Efficient cooling may also allow disc formation (see section C.2); the question of whether or not a disc can form in the adiabatic, parabolic case remains open.

Despite this limitation, our photospheric radius estimates yield a luminosity evolution comparable to optical/UV light curves from several recently observed TDEs (see Figures 6.3 and 6.5). We do not expect that the dynamics of our simulations would be significantly affected by allowing the photosphere to radiate at early times, mainly because the energy release via radiation is small — most of the energy in our Eddington envelope is released via mechanical outflows, with typical outflow velocities of ~ 1–2×10^4 km s^{-1} (see bottom panel of Figure 6.2). Such velocities match those observed in spectral lines (e.g. Leloudas et al., 2019). In any case, the cooling and subsequent retreat of the photosphere should stall or plateau at the hydrogen recombination temperature of ~ 6000 K.

We find that the optical light curve is sensitive to the observing angle, as suggested by Dai et al. (2018), but due to different photospheric radii along different lines of sight (see Figures 6.3 and 6.5) rather than the presence of a disc. The mildly supersonic outflows indicate that temperatures are also not in equilibrium across the photosphere.

The photospheric radii plateau at $\sim$ 20 to $\sim$ 100 au, depending on the line of sight and the amount of material participating in the outflow (Figures 6.3 and 6.5). Applying a single-zone model with uniform density $\rho = \frac{4\pi}{3}\frac{M}{R^3}$ to a homologously expanding envelope, this stalling is

estimated to occur when the photospheric radius is $\frac{2}{3}\sqrt{\frac{\kappa M}{4\pi}}$, where the mass M in the envelope depends on the penetration factor β. This estimate yields a photospheric radius plateau of ~ 100 au for our choice of κ and $M = 0.1 M_\odot$. While our predicted radius evolution might change if we allowed radiation to escape (especially at these late times), a significant late-time flattening has been observed in optical/UV for black holes of this mass (van Velzen et al., 2019).

If optical light curves are indeed produced by an expanding and contracting photosphere, we predict a relatively tight anti-correlation between temperature and radius, since smaller photospheric radii correspond to seeing deeper into the envelope where temperatures are higher. Such a correlation is indeed observed (van Velzen, private communication), and was predicted analytically by Lodato and Rossi (2011).

Finally, we do not predict significant X-ray emission. This agrees with the generally low ratio of X-ray to optical luminosities seen in the majority of TDEs (e.g. Auchettl et al., 2017), but is in conflict with observations of ASASSN-14li which show similar X-ray and optical luminosities (Holoien et al., 2016), though with X-rays lagging by 32 days (Pasham et al., 2017), which is difficult to explain via reprocessing. We expect that disc formation may become possible at late times as the material cools and the photosphere retreats to reveal regions close to the black hole. This would produce a rising X-ray luminosity similar to that observed by Gezari et al. (2017) and the class of 'veiled' TDEs (Auchettl et al., 2017). But without a better radiation treatment we are not able to speculate further.

6.5 Conclusions

We have performed a first principles calculation of a tidal disruption event with realistic stellar and orbital parameters, following the simulations for one year post disruption. Our main finding is the production of an optically thick 'Eddington envelope' hypothesised by a number of previous authors (e.g. Loeb and Ulmer, 1997; Metzger and Stone, 2016). Our calculations predict

1. low gas velocities, up to $\sim 2 \times 10^4$ km s^{-1}
2. large photosphere radii of $\sim$ 10–100 au
3. inefficient accretion ($\sim 10^{-2} M_\odot$/yr) mediated by the mechanical outflow of material
4. energy dissipation rates of $\sim 10^{43}$–10^{44} erg/s
5. peak luminosities of $\sim 10^{43}$–10^{44} erg/s

We thus confirm Eddington envelopes as the likely solution to the puzzle of TDE optical/UV emission.

Chapter 7

Conclusions

7.1 Summary

The work presented in this thesis is composed of two main parts: the development of a general relativistic smoothed particle hydrodynamics code, and the investigation of the tidal disruption of stars by supermassive black holes using this new code.

In Chapter 3 we developed our method for GRSPH and presented our results of rigorous, standardised tests in both 1D and 3D. Our method is general in the sense that it can be used with any metric, but our focus was on performing tests in special relativity using the Minkowski metric, and tests in general relativity around black holes using the Schwarzschild and Kerr metrics. We demonstrated that our method is precise and accurate at capturing ultra-relativistic shocks, up to Lorentz factors of at least $\Gamma = 44.5$ and with gas velocities transverse to the shock. This was made possible by several features of our method. Firstly, we evolved an entropy variable instead of the specific total energy. This made our time integration robust, preventing negative pressures from developing under extreme circumstances (such as those in ultra relativistic shocks). Secondly, we implemented new shock capturing terms that provide a positive definite contribution to the entropy in special relativity. We also showed how to split the viscous and thermal conduction components of the shock dissipation terms, which allowed us to treat contact discontinuities accurately. Thirdly, we carefully constructed the signal speeds involved in the dissipative terms to be Lorentz invariant along the line-of-sight between particles, and to not exceed the speed of light. Both the shock capturing terms and signal speeds were also designed to reduce to the non-relativistic terms in the Newtonian limit (as implemented in PHANTOM).

We also demonstrated the ability of our method to correctly capture orbital dynamics around both rotating and non-rotating black holes. We accurately reproduced epicyclic and vertical oscillation frequencies arising from relativistic precession effects. This was made possible by our development of a new, hybrid time-integration algorithm based on generalisations of the Leapfrog algorithm and RESPA scheme. Our scheme is symplectic and reversible for orbital dynamics, whilst also being efficient for relativistic SPH. That is, we conserve angular momentum to machine precession in the Schwarzschild metric, and have no long term drift in the energy error. Our algorithm's efficiency lies in the substepping of external forces and its reuse of the SPH force between subsequent steps.

Finally, we implemented our general relativistic method within the framework of the non-relativistic 3D SPH code PHANTOM. We showed that our code was able to accurately perform

hydrodynamics in curved spacetimes by running calculations of spherically symmetric Bondi accretion onto a black hole and comparing our results to the exact solution.

In Chapter 5 we used GR-PHANTOM to investigate the effect of black hole spin on disc formation from the tidal disruption of stars on eccentric orbits by rotating supermassive black holes. We found that while Lense-Thirring precession can inhibit the self-intersection of tidal debris streams, it only delays disc formation by a few orbital periods, at least for the parameters we investigated. This broad statement was unchanged by black hole spin, inclination and penetration factor. The structure of the remnant disc depends on the efficiency of radiative cooling. We simulated inefficient radiative cooling by employing an adiabatic equation of state, in which case the remnant disc takes the form of a fat torus with an aspect ratio of ~ 1. By contrast, using radiatively efficient cooling produced a narrow ring at roughly twice the pericentre distance. We modelled this regime using an isentropic formulation, in which we discarded all irreversible heating due to viscosity and shocks. In both cases, the remnant disc is formed at roughly the same inclination as the initial stellar orbit, and Lense-Thirring precession causes the remnant disc to precess about black hole spin axis.

We self-consistently computed the energy dissipation rate in our calculations, as well as the accretion rate, which we converted into an effective luminosity (not to be confused with observed luminosity), and which roughly tracked the dissipation rate. The general shape of these approximate light curves involved a rapid rise to $\sim 10^{47}$ erg s^{-1} for deep encounters, or $\sim 10^{45}$ erg s^{-1} for orbits with $\beta = 1$, followed by a power law decay. In both cases the luminosity was super-Eddington.

In Chapter 6 we investigated whether the results from TDEs involving eccentric orbits extended to TDEs involving parabolic orbits — the more realistic orbital scenario. We simulated the disruption of the star and followed the fallback of debris for one year post disruption. This revealed the formation of a large 'Eddington envelope', with an optically thick inner region, encasing the central black hole. Such an envelope was proposed by previous authors to explain puzzling optical and UV emission from TDEs, the idea being that high energy photons generated in the vicinity of the black hole during accretion would be reprocessed by the dense gas and eventually diffuse out through a photosphere at lower energies. We measured the photosphere in our calculations along multiple lines of sight. To our surprise, we found that our photosphere evolution roughly matched observations. In particular, we correctly predicted the rise, fall and subsequent flattening, with a typical photosphere radius between 10–100 au. We also predicted mass loaded outflows with velocities of $\sim$20,000 km/s, low temperatures of $\sim 10^4$ K that stay roughly constant in time, and faint luminosities of $\sim 10^{43}$–10^{44} erg/s, in agreement with observations.

7.2 Future work

7.2.1 Applications

There are a number of applications for future work that do not require further development of our GRSPH method. Much of our investigation on TDEs was restricted to a small part of parameter space. We did not consider retrograde orbits, which can be unique and interesting since frame dragging inside the ergosphere of the black hole can force a particle's trajectory to reverse direction. We also did not consider mass ratios other than 10^6, which changes the tidal radius and

thus the importance of general relativistic effects. We neglected the role of stellar spin, which has been shown to have an impact on the mass fallback rate in non-relativistic studies (Golightly et al., 2019; Sacchi and Lodato, 2019). The stellar structure has also been shown to be important (Lodato et al., 2009), which could be explored further by using a more realistic equation of state (such as those provided by MESA[1]). However, this may be challenging to implement since our entropy evolution currently assumes an adiabatic equation of state. A realistic equation of state would also allow us to treat the transition between gas and radiation pressure dominated regimes in the Eddington envelope.

Relativistic SPH and our ability to accurately treat ultra-relativistic shocks would also be useful in the study of pulsar winds, since current SPH simulations employ non-relativistic flows with a tuned momentum flux (e.g. Okazaki et al., 2011). This approach captures large scale structures but causes differences on the small scale (Rosen et al., 1999) since flows are inherently relativistic.

Finally, GRSPH is well suited for the study of tilted black hole accretion discs, which require an accurate treatment of general relativistic effects. Ivanov and Illarionov (1997) and Lubow et al. (2002) showed that the steady state structure of a tilted accretion disc is warped, and that the innermost part of the disc is not necessarily aligned with the black hole equator but may have an oscillatory profile. This has been demonstrated in non-relativistic 3D SPH simulations with a post-Newtonian treatment of relativistic precession effects (e.g. Nealon et al., 2015), however the approximations used are generally not accurate inside $\approx 10R_g$, which is where the oscillations develop. We briefly attempted to simulate this problem using GRSPH but ran into difficulties that we were unable to overcome given time constraints.

7.2.2 Methods

Our GRSPH code also has many possible extensions that will be the subject of future work. In particular, we would like to improve our artificial viscosity terms to be positive definite in *all* circumstances and in *any* metric. Our current implementation only guarantees a positive definite contribution to the entropy when the fluid velocity in the frame of a local Eulerian observer is a monotonic function of the coordinate velocity (Appendix A.1). This is typically not an issue in practice, although we did find that a very small fraction of particles had negative energy dissipation rates in our TDE simulations, which is unphysical.

While we made every effort to design an efficient time integration algorithm in Section 3.6.3, we find that it performs slower than its non-relativistic counterpart, typically by a factor of a few. This is because it involves implicit steps that require several iterations to solve. As a consequence, it is computationally expensive to perform very high resolution simulations. A possible solution to this is a class of explicit Hamiltonian integrators that are symplectic and time-reversible, even for non-separable Hamiltonians (e.g. Pihajoki, 2015; Tao, 2016). This would be particularly useful for our investigation in Chapter 6, since it is not yet clear if the lack of a disc in the centre of the Eddington envelope is physical or simply a consequence of low resolution.

With the first-ever image of a black hole taken by the Event Horizon Telescope (Event Horizon Telescope Collaboration et al., 2019), we have considered implementing a general relativistic ray-tracing method to visualise our simulations more accurately. In the context of TDE simulations, this would also be useful for generating synthetic, multi-wavelength light curves in post-

[1]Modules for Experiments in Stellar Astrophysics

processing. Furthermore, the ray-tracing method could be developed into a live radiation transport scheme, which would allow us to model the radiative cooling of gas accurately during a TDE, and generate self-consistent light curves.

The presence of magnetic fields may be important in discs that are predicted to form from the tidal disruption of stars (Bonnerot et al., 2017b,a; Svirski et al., 2017). In particular, the magneto-rotational instability (MRI) is thought to be the mechanism that drives accretion in black hole discs. Current SPH simulations of black hole accretion discs typically assume a Shakura and Sunyaev (1973) disc viscosity and model it using the SPH shock capturing terms (e.g. Lodato and Price, 2010; Nealon et al., 2015). Implementing a general relativistic smoothed particle magneto-hydrodynamics (GRSPMHD) method would allow us to model disc viscosity self-consistently, as is done by finite-volume GRMHD codes (e.g. Fragile et al., 2007, 2009; Fragile, 2009; Morales Teixeira et al., 2014).

Our current treatment of self-gravity in simulations of TDEs is rather crude and certainly not covariant. We simply add the Newtonian self-gravity to our relativistic momentum equation. This is typically not a problem in practice, since the contribution is very small and merely acts to hold the star together during the pre-disruption phase. It is also valid in the limit of flat space i.e. far from the black hole, which is where self-gravity is important. However, we suspect that it may be the reason why we have had difficulty performing retrograde, parabolic TDE calculations with high penetration factor. In future, we wish to make the implementation of the star's self-gravity more rigorous by treating it as a perturbation on top of the fixed background metric. Of course, the most accurate way to incorporate self-gravity would be to allow a dynamically evolving spacetime, however this would require coupling our method with a numerical relativity scheme; a task worthy of a PhD in its own right. Such a method would allow us to model many more complex relativistic systems where the spacetime itself is dynamic, such as the merger of two neutron stars. The prospect of this is particularly exciting, given the recent detection of gravitational waves from a binary neutron star merger (Abbott et al., 2017a), and the coincident detection of an electromagnetic afterglow (Abbott et al., 2017b).

Appendix A

GRSPH

A.1 Positivity of the entropy change

A.1.1 Conductivity

First, we will prove that the artificial conductivity contributes to a positive definite change to the total entropy. Taking Equation 3.69 and relating it back to the specific entropy

$$T_a \frac{\mathrm{d}s_a}{\mathrm{d}t} = U_a^0 \left(\Pi_{\mathrm{cond}}^a + \sum_b m_b \frac{q_a \left(v_a^i - v_b^i\right)}{\rho_a^{*2}} D_i^a \right). \tag{A.1}$$

The change in total entropy is

$$\frac{\mathrm{d}S}{\mathrm{d}t} = \sum_a m_a \frac{\mathrm{d}s_a}{\mathrm{d}t}, \tag{A.2}$$

and thus the contribution from artificial conductivity is

$$\left.\frac{\mathrm{d}S}{\mathrm{d}t}\right|_{\mathrm{cond}} = \sum_a \frac{m_a U_a^0}{T_a} \Pi_{\mathrm{cond}}^a, \tag{A.3}$$

$$= \sum_a \sum_b \zeta_{ab} \frac{U_a^0}{T_a} \left(\frac{u_a}{U_a^0} - \frac{u_b}{U_b^0} \right), \tag{A.4}$$

where we have used the relation $U^0 = \Gamma/\alpha$, and defined the negative, symmetric term

$$\zeta_{ab} \equiv \frac{1}{2} \alpha_u m_a m_b \left(\frac{v_{\mathrm{sig},a}^u G_a}{\rho_a^*} + \frac{v_{\mathrm{sig},b}^u G_b}{\rho_b^*} \right) \leq 0. \tag{A.5}$$

Splitting Eq. A.4 into two equal sums, interchanging the labels on one, and then recombining into a single sum, we get

$$\left.\frac{\mathrm{d}S}{\mathrm{d}t}\right|_{\mathrm{cond}} = \sum_a \sum_b \zeta_{ab} \left(\frac{U_a^0}{T_a} - \frac{U_b^0}{T_b} \right) \left(\frac{u_a}{U_a^0} - \frac{u_b}{U_b^0} \right). \tag{A.6}$$

We note that U^0 is a strictly positive quantity, and $u \propto T$. Hence, if $u_a > u_b$, we must have $T_a > T_b$, and

$$\left(\frac{U_a^0}{T_a} - \frac{U_b^0}{T_b} \right) \left(\frac{u_a}{U_a^0} - \frac{u_b}{U_b^0} \right) < 0. \tag{A.7}$$

Thus the contribution to the total entropy, due to artificial conductivity, is always positive in both special and general relativity.

A.1.2 Viscosity

Next, we consider the change in entropy per particle due to artificial viscosity in Cartesian coordinates

$$\left.\frac{\mathrm{d}s_a}{\mathrm{d}t}\right|_{\mathrm{visc}} = \frac{U_a^0}{T_a}\sum_b m_b \frac{q_a\left(v_a^i - v_b^i\right)}{\rho_a^{*2}} D_i^a, \tag{A.8}$$

$$= \sum_b Q_{ab}\left(\Gamma_a^* V_a^* - \Gamma_b^* V_b^*\right)\left(v_a^* - v_b^*\right), \tag{A.9}$$

where $v^* = N_i\, v^i$ is a line of sight velocity, and we defined the positive quantity

$$Q_{ab} \equiv -\frac{1}{2}\frac{U_a^0}{T_a \rho_a^*} m_b \alpha_{\mathrm{AV}} v_{\mathrm{sig},a} w_a G_a \geq 0. \tag{A.10}$$

In the case that V^* is a monotonically increasing function of v^* in a given spacetime, if $v_a^* > v_b^*$ we must have $V_a^* > V_b^*$ as well as $\Gamma_a^* > \Gamma_b^*$, and hence

$$\left(\Gamma_a^* V_a^* - \Gamma_b^* V_b^*\right)\left(v_a^* - v_b^*\right) > 0. \tag{A.11}$$

The condition that V^* be monotonic is easily satisfied in the Minkowski metric, where $V^i = v^i$, since there is no shift, $\beta^i = 0$, and the lapse $\alpha = 1$. Thus in the case of special relativity, the artificial viscosity will only ever increase the entropy of a particle, however this cannot be guaranteed in all spacetimes.

A.2 Recovery of primitive variables

Step 3 of section 3.7 involves solving the equation

$$f(w) \equiv w(\rho, P) - w = 0 \tag{A.12}$$

for w, where ρ and P are functions of w (Eq. 3.97 and 3.98). For this we use the standard Newton-Raphson algorithm

$$w_{n+1} = w_n - \frac{f(w_n)}{f'(w_n)}, \tag{A.13}$$

which requires the derivative $f'(w)$. Here, the subscript n corresponds to the iteration number. For the initial prediction, w_0, we use the enthalpy computed at the previous timestep. Iterations of Equation A.13 are repeated until the following convergence criteria is satisfied

$$\frac{w_{n+1} - w_n}{w_{n+1}} \leq \epsilon_w, \tag{A.14}$$

for some sufficiently small number ϵ_w. In this paper we use $\epsilon_w = 10^{-12}$. Given the ideal gas equation of state (Eq. 3.21), we can write

$$f(w) = \left[1 + \frac{P}{\rho}\left(\frac{\gamma_{\mathrm{ad}}}{\gamma_{\mathrm{ad}} - 1}\right)\right] - w \tag{A.15}$$

and hence the derivative can be written as

$$f'(w) = \frac{\gamma_{\mathrm{ad}}}{\gamma_{\mathrm{ad}} - 1}\left(1 - \frac{p^i p_i\, P}{w^3 \rho\, \Gamma^2}\right) - 1, \tag{A.16}$$

where ρ, P, and Γ are all functions of w (Eq. 3.97, 3.98 and 3.100). Equivalently, when evolving the entropy variable K

$$f'(w) = \frac{\gamma_{\rm ad}\, p^i p_i P}{w^3 \rho\, \Gamma^2} - 1, \tag{A.17}$$

where instead of Equation 3.98 for the pressure, we use

$$P(w) = K\left[\rho(w)\right]^{\gamma_{\rm ad}}, \tag{A.18}$$

$$= K\left[\frac{\rho^*}{\sqrt{\gamma}\,\Gamma(w)}\right]^{\gamma_{\rm ad}}. \tag{A.19}$$

A.3 Metrics in Cartesian Coordinates

A.3.1 Schwarzschild metric

The Schwarzschild metric line element, in standard spherical coordinates (t, r, θ, ϕ) is

$$ds^2 = -\left(1 - \frac{2M}{r}\right)\mathrm{d}t^2 + \frac{\mathrm{d}r^2}{1 - \frac{2M}{r}} + r^2\left(\mathrm{d}\theta^2 + \sin^2\theta\,\mathrm{d}\phi^2\right). \tag{A.20}$$

If we make the coordinate transformation

$$\begin{aligned} x &= r\sin\theta\cos\phi, \\ y &= r\sin\theta\sin\phi, \\ z &= r\cos\theta, \end{aligned} \tag{A.21}$$

we can write the components of the covariant metric in Cartesian coordinates (t, x, y, z)

$$\begin{aligned} g_{tt} &= -\left(1 - \frac{2M}{r}\right), \\ g_{xx} &= \frac{1}{1 - \frac{2M}{r}}\left(1 - \frac{2M}{r^3}(y^2 + z^2)\right), \\ g_{yy} &= \frac{1}{1 - \frac{2M}{r}}\left(1 - \frac{2M}{r^3}(x^2 + z^2)\right), \\ g_{zz} &= \frac{1}{1 - \frac{2M}{r}}\left(1 - \frac{2M}{r^3}(x^2 + y^2)\right), \\ g_{yx} &= g_{xy} = \frac{xy}{1 - \frac{2M}{r}}\frac{2M}{r^3}, \\ g_{zx} &= g_{xz} = \frac{xz}{1 - \frac{2M}{r}}\frac{2M}{r^3}, \\ g_{zy} &= g_{yz} = \frac{yz}{1 - \frac{2M}{r}}\frac{2M}{r^3}, \\ g_{tx} &= g_{ty} = g_{tz} = g_{xt} = g_{yt} = g_{zt} = 0, \end{aligned} \tag{A.22}$$

as well as the components of the contravariant metric

$$g^{tt} = -\frac{1}{1 - \frac{2M}{r}},$$

$$
\begin{aligned}
g^{xx} &= 1 - \frac{2M}{r^3}x^2, \\
g^{yy} &= 1 - \frac{2M}{r^3}y^2, \\
g^{zz} &= 1 - \frac{2M}{r^3}z^2, \\
g^{yx} &= g_{xy} = -\frac{2M}{r^3}xy, \\
g^{zx} &= g_{xz} = -\frac{2M}{r^3}xz, \\
g^{zy} &= g_{yz} = -\frac{2M}{r^3}yz, \\
g^{tx} &= g^{ty} = g^{tz} = g^{xt} = g^{yt} = g^{zt} = 0,
\end{aligned}
\tag{A.23}
$$

where $r = \sqrt{x^2 + y^2 + z^2}$. In these coordinates $\sqrt{-g} = 1$. The derivatives $\partial g_{\mu\nu}/\partial x^i$ can be found analytically by differentiating $g_{\mu\nu}$, or through a finite difference approximation.

A.3.2 Kerr metric

The Kerr metric line element in standard Boyer-Lindquist coordinates (t, r, θ, ϕ) is

$$
\begin{aligned}
ds^2 = &-\left(1 - \frac{2Mr}{\rho^2}\right)\mathrm{d}t^2 - \frac{4Mra\sin^2\theta}{\rho^2}\mathrm{d}t\,\mathrm{d}\phi + \frac{\rho^2}{\Delta}\mathrm{d}r^2 \\
&+ \rho^2\mathrm{d}\theta^2 + \left(a^2 + r^2 + \frac{2Mr}{\rho^2}a^2\sin^2\theta\right)\sin^2\theta\,\mathrm{d}\phi^2,
\end{aligned}
\tag{A.24}
$$

where

$$
\rho^2 = r^2 + a^2\cos^2\theta, \tag{A.25}
$$

$$
\Delta = r^2 - 2Mr + a^2, \tag{A.26}
$$

and $|a| \leq M$ is the spin parameter. If we make the coordinate transformation

$$
\begin{aligned}
x &= \sqrt{r^2 + a^2}\sin\theta\cos\phi, \\
y &= \sqrt{r^2 + a^2}\sin\theta\sin\phi, \\
z &= r\cos\theta,
\end{aligned}
\tag{A.27}
$$

we can write the components of the covariant metric in Cartesian-like coordinates (t, x, y, z)

$$
\begin{aligned}
g_{tt} &= -\left(1 - \frac{2Mr}{\rho^2}\right), \\
g_{xt} &= g_{tx} = \frac{-y}{x^2 + y^2}g_{t\phi}, \\
g_{yt} &= g_{ty} = \frac{x}{x^2 + y^2}g_{t\phi}, \\
g_{zt} &= g_{tz} = 0, \\
g_{xx} &= \frac{r^2x^2}{\rho^2\Delta} + g_{\phi\phi}\left(\frac{y}{x^2 + y^2}\right)^2 + \frac{x^2z^2}{\rho^2(r^2 - z^2)}, \\
g_{yy} &= \frac{r^2y^2}{\rho^2\Delta} + g_{\phi\phi}\left(\frac{x}{x^2 + y^2}\right)^2 + \frac{y^2z^2}{\rho^2(r^2 - z^2)},
\end{aligned}
\tag{A.28}
$$

$$
\begin{aligned}
g_{zz} &= \frac{z^2(a^2+r^2)^2}{r^2\rho^2\Delta} + \frac{\rho^2}{r^2-z^2}\left(1-\frac{z^2(a^2+r^2)}{r^2\rho^2}\right)^2,\\
g_{xy} = g_{yx} &= r^2\frac{xy}{\rho^2\Delta} - g_{\phi\phi}\frac{xy}{(x^2+y^2)^2} + \frac{xyz^2}{\rho^2(r^2-z^2)},\\
g_{xz} = g_{zx} &= (a^2+r^2)\frac{xz}{\rho^2\Delta} - \frac{xz}{(r^2-z^2)}\left(1-\frac{z^2(a^2+r^2)}{r^2\rho^2}\right),\\
g_{yz} = g_{zy} &= (a^2+r^2)\frac{yz}{\rho^2\Delta} - \frac{yz}{(r^2-z^2)}\left(1-\frac{z^2(a^2+r^2)}{r^2\rho^2}\right),
\end{aligned}
$$

and the components of the contravariant metric

$$
\begin{aligned}
g^{tt} &= \frac{-g_{\phi\phi}}{{g_{t\phi}}^2 - g_{\phi\phi}g_{tt}},\\
g^{xt} = g^{tx} &= \frac{-yg_{t\phi}}{{g_{t\phi}}^2 - g_{\phi\phi}g_{tt}},\\
g^{yt} = g^{ty} &= \frac{xg_{t\phi}}{{g_{t\phi}}^2 - g_{\phi\phi}g_{tt}},\\
g^{zt} = g^{tz} &= 0,\\
g^{xx} &= \frac{r^2x^2\Delta}{\rho^2(a^2+r^2)^2} - \frac{y^2g_{tt}}{{g_{t\phi}}^2 - g_{\phi\phi}g_{tt}} + \frac{x^2z^2}{\rho^2(r^2-z^2)},\\
g^{yy} &= \frac{r^2y^2\Delta}{\rho^2(a^2+r^2)^2} - \frac{x^2g_{tt}}{{g_{t\phi}}^2 - g_{\phi\phi}g_{tt}} + \frac{y^2z^2}{\rho^2(r^2-z^2)},\\
g^{zz} &= \frac{r^2-z^2}{\rho^2} + \frac{z^2\Delta}{r^2\rho^2},\\
g^{xy} = g^{yx} &= \frac{r^2xy\Delta}{\rho^2(a^2+r^2)^2} + \frac{xyg_{tt}}{{g_{t\phi}}^2 - g_{\phi\phi}g_{tt}} + \frac{xyz^2}{\rho^2(r^2-z^2)},\\
g^{xz} = g^{zx} &= -\frac{xz}{\rho^2} + \frac{xz\Delta}{\rho^2(a^2+r^2)},\\
g^{yz} = g^{zy} &= -\frac{yz}{\rho^2} + \frac{yz\Delta}{\rho^2(a^2+r^2)},
\end{aligned}
\tag{A.29}
$$

where

$$
r = \sqrt{\frac{R^2-a^2+\sqrt{(R^2-a^2)^2+4a^2z^2}}{2}}, \tag{A.30}
$$

$$
R^2 = x^2+y^2+z^2, \tag{A.31}
$$

$$
\rho^2 = r^2 + a^2\frac{z^2}{r^2}, \tag{A.32}
$$

$$
g_{tt} = -\left(1-\frac{2Mr}{\rho^2}\right), \tag{A.33}
$$

$$
g_{\phi\phi} = \left(r^2+a^2+\frac{2Mr}{\rho^2}a^2\sin^2\theta\right)\sin^2\theta, \tag{A.34}
$$

$$
g_{t\phi} = -\frac{2Mra}{\rho^2}\sin^2\theta, \tag{A.35}
$$

$$
\sin^2\theta = 1-\frac{z^2}{r^2}. \tag{A.36}
$$

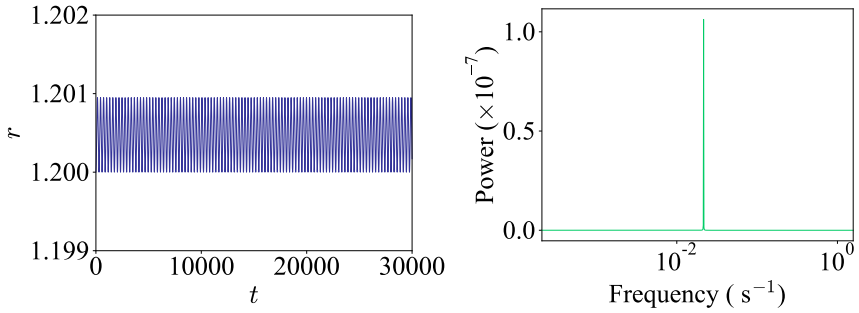

Figure A.1: Radius as a function of time (left), and the corresponding 1D power spectrum (right), for the epicycle at $r = 1.2$ with black hole spin $a = 1$.

We again have $\sqrt{-g} = 1$ in the new coordinates and the derivatives $\partial g_{\mu\nu}/\partial x^i$ can be found analytically by differentiating $g_{\mu\nu}$, or through a finite difference approximation.

A.3.3 Derivatives of the metric

We compute the derivatives of the Schwarzschild metric by analytically differentiating $g_{\mu\nu}$, however for the Kerr metric we choose to compute the derivatives through a 2nd order centred finite difference approximation

$$\frac{\partial g_{\mu\nu}(x^i)}{\partial x^i} \approx \frac{g_{\mu\nu}(x^i + \epsilon) - g_{\mu\nu}(x^i - \epsilon)}{2\epsilon}, \tag{A.37}$$

for $\epsilon \ll 1$. In our simulations we use $\epsilon = 10^{-8}$.

A.3.4 Inverse

The contravariant metric $g^{\mu\nu}$ can also be found by inverting the matrix $g_{\mu\nu}$ at every point, since

$$g_{\mu\alpha} g^{\nu\alpha} = \delta^{\nu}_{\mu}. \tag{A.38}$$

Given the determinant of the covariant metric g, we simply compute the adjugate matrix of $g_{\mu\nu}$, and then

$$g^{\mu\nu} = \frac{1}{g}\mathrm{adj}(g_{\mu\nu}). \tag{A.39}$$

In practice we find that this conserves Eq.A.38 better than the analytic contravariant terms near the event horizon. As such, we compute the contravariant metric in this manner by default.

A.4 Computing oscillation frequencies

To measure the oscillation frequencies described in Sections 3.8.3 and 3.8.3, we take the maximum value of the 1-D power spectrum of $r(t)$, using `numpy.fft.fft` in PYTHON. Figure A.1 shows the time series (left) and corresponding power spectrum (right) for the $a = 1$, $r = 1.2$ case.

Appendix B

Tidal disruption of stars on eccentric orbits

B.1 Effect of resolution

Figure B.1 shows the effect of resolution in Simulation 1 at three different resolutions. The *top* row compares the self-intersection at $t = 37.8$ hrs, the *middle* row shows the accretion dynamics at $t = 55.6$ hrs, and the *bottom* row compares the remnant torus formed at $t = 111$ hrs. We increase the number of particles by approximately a factor of 8 between each panel from left to right, corresponding to a factor of 2 increase in spatial resolution. The self-intersection is better resolved and the torus is more defined with increasing resolution, however the overall structure remains the same.

Figure B.2 compares our approximate luminosity from the accretion rate at each resolution. At early times (see top row of Figure B.1) differences are mainly caused by progressively better resolving of the circularisation process. The increased accretion luminosity at the highest resolution (green curve) seen at $t \approx 50$ hrs (see middle row of Figure B.1) is mainly driven by an increased amount of material on plunging orbits. At late times, $t > 100$ hrs, these differences become irrelevant (bottom row of Figure B.1).

B.2 Self-gravity

We consider the self-gravity of the star as a small perturbation to the background (Kerr) spacetime. That is, we write the metric in the form

$$\tilde{g}_{\mu\nu} = g_{\mu\nu} + h_{\mu\nu}, \tag{B.1}$$

where $|h_{\mu\nu}| \ll |g_{\mu\nu}|$ is a small perturbation. We assume a scalar perturbation to the metric, Φ, in the usual form

$$h_{00} = -2\Phi; \qquad h_{ij} = 2\Phi/c^2\delta_{ij}. \tag{B.2}$$

Our assumption that $|h_{\mu\nu}| \ll |g_{\mu\nu}|$ means that we neglect $h_{\mu\nu}$ in comparison to $g_{\mu\nu}$ always, but do not assume that the gradient of $h_{\mu\nu}$ is small. We thus use $g_{\mu\nu}$ when computing dot products. The only change to the method is then an additional term in the momentum equation in the form

$$\left(\frac{\mathrm{d}p_i}{\mathrm{d}t}\right)_{\mathrm{sg}} = \frac{1}{2}U^0\frac{v^\mu v^\nu}{c^2}\frac{\partial h_{\mu\nu}}{\partial x^i}, \tag{B.3}$$

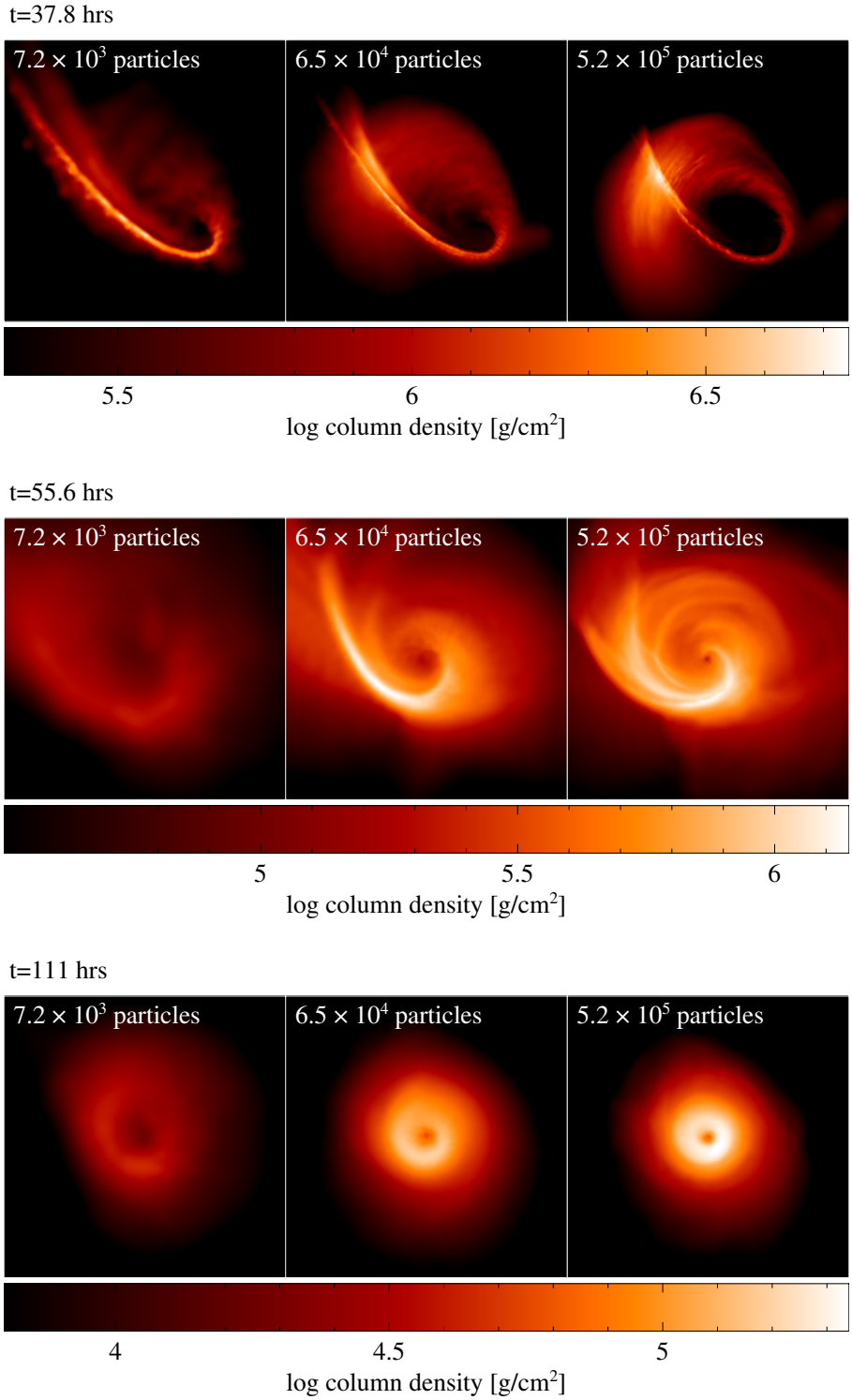

Figure B.1: Effect of resolution in Simulation 1. *Top row:* comparison of the self-intersection at $t = 37.8$ hrs. *Middle row:* comparison of the accretion dynamics at 55.6 hrs. *Bottom row:* comparison of the remnant torus at $t = 111$ hrs. Total number of particles increases by approximately a factor of 8 between panels from left to right, with the right panel corresponding to the resolution shown in Fig. 5.1.

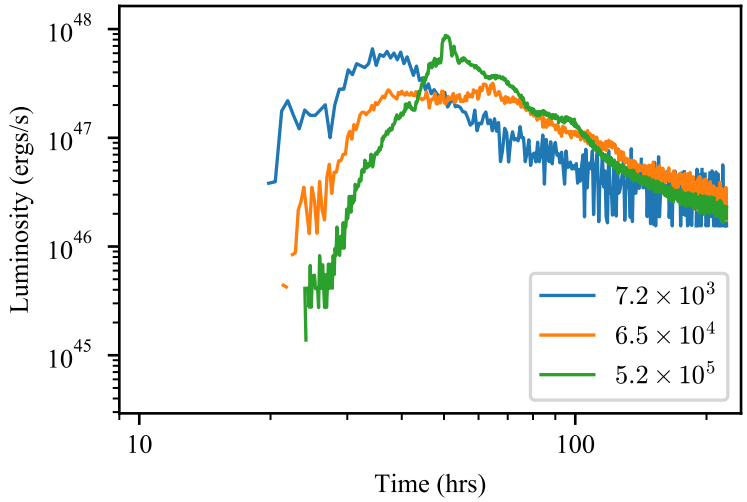

Figure B.2: Comparison of $L_{\rm acc}$ at three different resolutions (number of particles) in Sim. 1. For lower resolutions, the accretion rate is higher during the early stage of the fallback and then lower at late times.

where we have neglected terms of $\mathcal{O}(v/c)^2$. The only non-zero terms are therefore

$$\left(\frac{{\rm d}p_i}{{\rm d}t}\right)_{\rm sg} = -U^0\frac{\partial\Phi}{\partial x^i} + U^0\delta_{lm}\frac{v^l v^m}{c^2}\frac{\partial\Phi}{\partial x^i}, \tag{B.4}$$

The first term is the usual Newtonian acceleration term, while the second is a special relativistic correction of order $(v/c)^2$. Since self-gravity is only important at distances far from the black hole, we neglect the special relativistic correction term, and one may neglect the prefactor to simply use

$$\left(\frac{{\rm d}p_i}{{\rm d}t}\right)_{\rm sg} = -\frac{\partial\Phi}{\partial x^i}. \tag{B.5}$$

This approximation breaks down close to the black hole, but within the tidal radius — by definition — the corrections due to self-gravity are negligible anyway. The Newtonian potential Φ is computed in the usual manner by solving Poisson's equation via a treecode (for details see Price et al. 2018).

A possible improvement to our method would be to take account of the special relativistic corrections in the self-gravity term. We have not attempted to do so in this paper.

Appendix C

Tidal disruption of stars on parabolic orbits

C.1 Effect of resolution

Figure C.1 shows the effect of resolution in our simulations. The setup is identical to that shown in Figure 6.1 except with $a = \theta = 0$. The *top* row compares the large scale structure, while the *bottom* compares the details of the stream fanning on a smaller scale. We increase the number of particles by approximately a factor of 8 between each column from left to right, corresponding to a factor of 2 increase in spatial resolution. On large scales, we find that the envelope is less isotropic at higher resolutions, with more material in a 'spiral arm' that is denser than the rest of the envelope. This is due to improved resolution of the stream at periapsis passage, as discussed in section C.3.

C.2 Radiatively efficient cooling and disc formation

Figure C.2 demonstrates that disc formation can occur if the gas is allowed to cool. We continue the calculation from Fig. 6.1 but at 1 year after disruption switch to an isentropic formulation in which we discard all irreversible heating due to viscosity and shocks (cf. Liptai et al., 2019). This corresponds to radiatively efficient cooling, which is a valid regime for the envelope after one year since the photon diffusion time is short (Fig. 6.3 *bottom*) and the adiabatic cooling rate exceeds the energy dissipation rate. However, in reality, the envelope would transition smoothly from nearly adiabatic expansion with inefficient cooling to efficient radiative cooling represented by the isentropic model.

We also confirmed that when the calculation is isentropic from the beginning, a similar disc/ring is formed roughly 110 days after disruption. This demonstrates that disc formation is suppressed by the lack of cooling and is not due to low resolution.

C.3 Stream disruption

Our numerical simulations show a significant disruption of the stream during the second periapsis passage. Material in the returning stream, with a narrow range of energies and angular momenta, is spread out along a range of trajectories. This seeds the formation of a thick bubble of gas and enabling efficient energy dissipation, and ultimately accretion or ejection, of subsequent inflowing material.

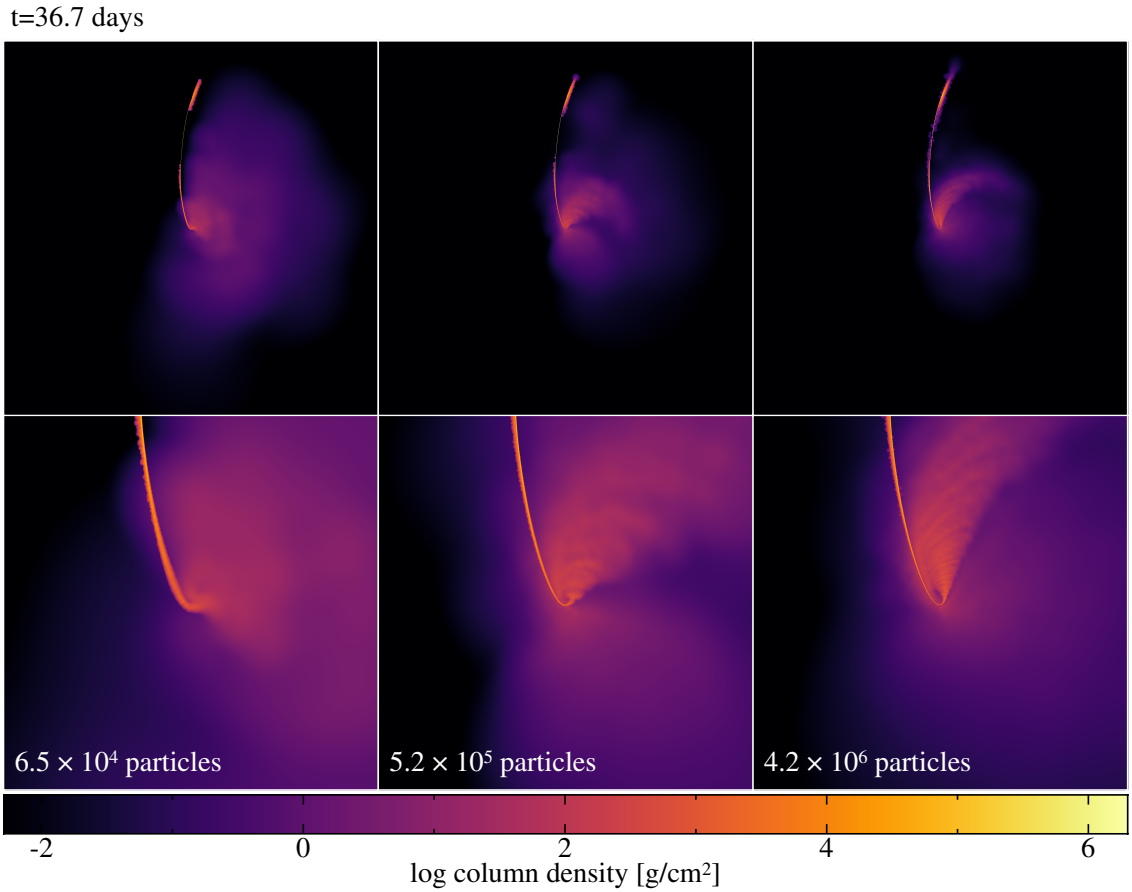

Figure C.1: Effect of resolution in calculations with $a = \theta = 0$ and $\beta = 1$. *Top row:* comparison of the large scale structure, where each panel is 500 au $\times$ 500 au. *Bottom row:* comparison of the stream fanning at small scales where each panel is 100 au $\times$ 100 au. The total number of particles increases by approximately a factor of 8 between columns from left to right, with the third column corresponding to the resolution used in our main calculations.

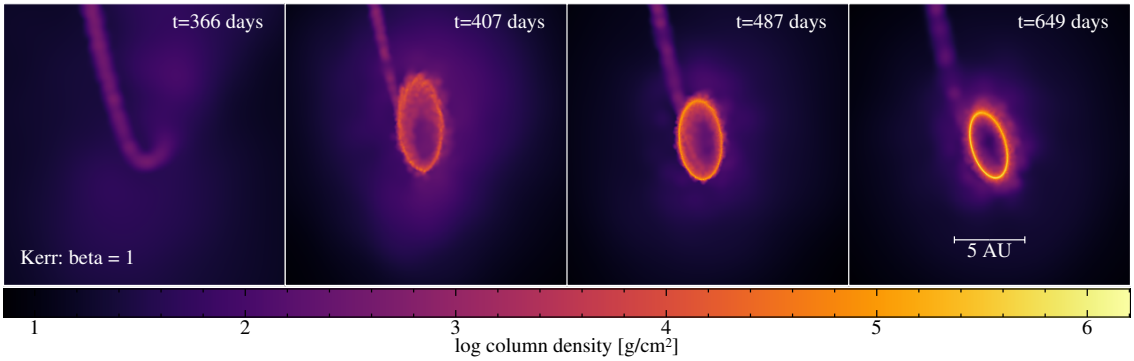

Figure C.2: Disc formation in the core of the envelope with radiatively efficient cooling. We resumed the main calculation show in Figure 6.1 one year after disruption assuming isentropic evolution. A narrow ring of material develops, which is inclined by $\sim 60°$ to the black hole spin plane. Each panel is 20 au $\times$ 20 au.

We find a much enhanced heating of the stream in simulations of tidal disruptions of stars on parabolic orbits than in simulations of tidal disruptions of stars on bound eccentric orbits, even at high eccentricities of $e = 0.95$ (Liptai et al., 2019). The fact that this happens close to the periapsis at $\sim 50R_g$ argues against either apsidal precession or shock dissipation from material passing through the 'nozzle' as being responsible for this behaviour. Resolution studies (see section C.1) indicate that while the degree of spreading depends on the resolution, the qualitative behaviour is unchanged.

Here, we argue that the formation of a bubble of gas and disruption of the stream passing through periapsis for the second time is a generic feature of parabolic orbits that should be expected in realistic conditions.

Suppose that there is a small cloud of gas around the SMBH. In our simulations, this is seeded by the first returning material (which is not well resolved), but as we will show, the required gas density is within the range that could be expected in the vicinity of an SMBH. This cloud will interact with the returning stream, heating it and causing it to spread out. Of course, if a large (relative to the mass of the cloud) parcel of stream material arrives promptly, its linear and angular momentum will overwhelm the cloud and push the cloud's material out along with the stream. However, if the stream returns gradually, with a slow rise in the density, the pressure and SMBH gravity have time to rebuild the thermal cloud. This explains why streams in the parabolic case, in which matter returns more gradually than in the eccentric case, are more easily disrupted.

We make two assumptions:

1. Gravity and pressure redistribute particle velocities inside the cloud on a timescale of order the dynamical timescale of the cloud,

$$\tau \sim \sqrt{R_{\rm p}^3/(GM_{\rm BH})}\,. \tag{C.1}$$

2. The stream can not add too much more mass than the mass of the cloud m on this redistribution timescale, otherwise the newly added material will overwhelm the cloud; so at all times,

$$\tau\dot{m} \lesssim m \tag{C.2}$$

must hold.

We can calculate $\dot{m}$ and m under the assumption that, following the initial disruption of the star at $R_{\rm p}$, all of its material follows ballistic trajectories. Consider a slice of the star at an initial distance $R_{\rm p} - R_* + x$ from the SMBH; we will focus on early times, so $x \ll R_*$. This slice has volume $\sim x^2dx$ and mass $\sim x^2dxM_*/R_*^3$, assuming a roughly uniform-density star. Its specific energy is $\sim E_0 + GM_{\rm BH}x/R_{\rm p}^2$, where E_0 is the specific energy of the most-bound material: $E_0 \sim -GM_{\rm BH}R_*/R_{\rm p}^2$ for the parabolic case, and $E_0 \sim -GM_{\rm BH}(1-e)/R_*$ for the eccentric case with eccentricity $1 - e > (M_*/M_{\rm BH})^{1/3}$. (If the eccentricity of the bound orbit is more extreme than this, it behaves much like a parabolic orbit, since the ballistic trajectory of the most-bound material is similar in these cases and insensitive to the initial eccentricity.)

We can now compute the mass return rate:

$$\dot{m} \sim \frac{dm}{dx}\left(\frac{dP}{dx}\right)^{-1} \sim x^2\frac{M_*}{R_*^3}\frac{R_{\rm p}^2(-E_0)^{5/2}}{(GM)^2} \tag{C.3}$$

where the period P is given by $P \sim GM(-E)^{3/2}$. Substituting in the expressions for E_0, we find

$$\dot{m} \sim x^2 \frac{M_*}{R_\mathrm{p}^3} \sqrt{\frac{GM_\mathrm{BH}}{R_*}} \tag{C.4}$$

in the parabolic case and

$$\dot{m} \sim x^2 \frac{M_*}{R_*^3} \sqrt{\frac{GM_\mathrm{BH}}{R_\mathrm{p}}} (1-e)^{5/2} \tag{C.5}$$

in the eccentric case.

Finally, we can check when the condition in equation (C.2) is satisfied. The total mass in the cloud is $m \sim m_0 + M_* x^3 / R_*^3$, where m_0 is the initial mass. In the parabolic case, the condition is satisfied at all times provided that $m_0 \gtrsim (R_*/R_\mathrm{p})^{9/2} M_*$. In our example, $R_\mathrm{p} \approx 100 R_*$, so the cloud must initially contain at least $\sim 10^{-9}$ of the mass of the star. This requires a cloud density of order 10^{-15} g cm^{-3} in the vicinity of the SMBH; this number density of $\sim 10^9$ cm^{-3} is well below nuclear gas distribution models extrapolated to au distances from the SMBH (e.g., Stern et al., 2014).

Meanwhile, in the bound eccentric encounter case, the condition is satisfied only if $m_0 \gtrsim (R_\mathrm{p}/R_*)^3 (1-e)^{15/2} M_*$. For $R_\mathrm{p} \approx 100 R_*$, this implies that the mass of the cloud must exceed the mass of the star for eccentricities $e \lesssim 0.8$; even at initial eccentricities of 0.95, the initial cloud mass would have to exceed $10^{-4} M_\odot$, requiring a cloud of density 10^{-10} g cm^{-3} to be present at au distances.

We thus find that analytical estimates support spreading of streams for initially parabolic encounters, but not for encounters on initially bound orbits of moderate eccentricity unless very compact gas clouds are present close to the SMBH.

Bibliography

Abbott, B. P., R. Abbott, T. D. Abbott, M. R. Abernathy, F. Acernese, K. Ackley, C. Adams, T. Adams, P. Addesso, R. X. Adhikari, and et al.: 2016, 'Observation of Gravitational Waves from a Binary Black Hole Merger'. Phys. Rev. Lett. **116**(6), 061102.

Abbott, B. P., R. Abbott, T. D. Abbott, F. Acernese, K. Ackley, C. Adams, T. Adams, P. Addesso, R. X. Adhikari, V. B. Adya, and et al.: 2017a, 'GW170817: Observation of Gravitational Waves from a Binary Neutron Star Inspiral'. *Physical Review Letters* **119**(16), 161101.

Abbott, B. P., R. Abbott, T. D. Abbott, F. Acernese, K. Ackley, C. Adams, T. Adams, P. Addesso, R. X. Adhikari, V. B. Adya, and et al.: 2017b, 'Multi-messenger Observations of a Binary Neutron Star Merger'. ApJ **848**, L12.

Abramowicz, M., M. Jaroszynski, and M. Sikora: 1978, 'Relativistic, accreting disks'. A&A **63**, 221–224.

Akiyama, K., K. Kuramochi, S. Ikeda, V. L. Fish, F. Tazaki, M. Honma, S. S. Doeleman, A. E. Broderick, J. Dexter, M. Mościbrodzka, K. L. Bouman, A. A. Chael, and M. Zaizen: 2017, 'Imaging the Schwarzschild-radius-scale Structure of M87 with the Event Horizon Telescope Using Sparse Modeling'. ApJ **838**, 1.

Andersson, N. and G. L. Comer: 2007, 'Relativistic Fluid Dynamics: Physics for Many Different Scales'. *Living Reviews in Relativity* **10**, 1.

Arcavi, I., A. Gal-Yam, M. Sullivan, Y.-C. Pan, S. B. Cenko, A. Horesh, E. O. Ofek, A. De Cia, L. Yan, C.-W. Yang, D. A. Howell, D. Tal, S. R. Kulkarni, S. P. Tendulkar, S. Tang, D. Xu, A. Sternberg, J. G. Cohen, J. S. Bloom, P. E. Nugent, M. M. Kasliwal, D. A. Perley, R. M. Quimby, A. A. Miller, C. A. Theissen, and R. R. Laher: 2014, 'A Continuum of H- to He-rich Tidal Disruption Candidates With a Preference for E+A Galaxies'. ApJ **793**(1), 38.

Armitage, P. J. and P. Natarajan: 2002, 'Accretion during the Merger of Supermassive Black Holes'. ApJ **567**, L9–L12.

Arnowitt, R., S. Deser, and C. W. Misner: 2008, 'Republication of: The dynamics of general relativity'. *General Relativity and Gravitation* **40**, 1997–2027.

Auchettl, K., J. Guillochon, and E. Ramirez-Ruiz: 2017, 'New Physical Insights about Tidal Disruption Events from a Comprehensive Observational Inventory at X-Ray Wavelengths'. ApJ **838**, 149.

Ayal, S., M. Livio, and T. Piran: 2000, 'Tidal Disruption of a Solar-Type Star by a Supermassive Black Hole'. ApJ **545**, 772–780.

Bambi, C.: 2018, 'Astrophysical Black Holes: A Compact Pedagogical Review'. *Annalen der Physik* **530**(6), 1700430.

Barnes, J. E. and L. E. Hernquist: 1991, 'Fueling Starburst Galaxies with Gas-rich Mergers'. ApJ **370**, L65.

Bate, M. R., I. A. Bonnell, and V. Bromm: 2003, 'The formation of a star cluster: predicting the properties of stars and brown dwarfs'. MNRAS **339**, 577–599.

Bauswein, A., R. Oechslin, and H.-T. Janka: 2010, 'Discriminating strange star mergers from neutron star mergers by gravitational-wave measurements'. Phys. Rev. D **81**(2), 024012.

Benz, W. and J. G. Hills: 1987, 'Three-dimensional Hydrodynamical Simulations of Stellar Collisions. I. Equal-Mass Main-Sequence Stars'. ApJ **323**, 614.

Bolton, C. T.: 1972, 'Identification of Cygnus X-1 with HDE 226868'. Nature **235**(5336), 271–273.

Bonnerot, C. and W. Lu: 2019, 'Simulating realistic disc formation in tidal disruption events'. *arXiv e-prints* p. arXiv:1906.05865.

Bonnerot, C., D. J. Price, G. Lodato, and E. M. Rossi: 2017a, 'Magnetic field evolution in tidal disruption events'. MNRAS **469**(4), 4879–4888.

Bonnerot, C., E. M. Rossi, and G. Lodato: 2017b, 'Long-term stream evolution in tidal disruption events'. MNRAS **464**(3), 2816–2830.

Bonnerot, C., E. M. Rossi, G. Lodato, and D. J. Price: 2016, 'Disc formation from tidal disruptions of stars on eccentric orbits by Schwarzschild black holes'. MNRAS **455**(2), 2253–2266.

Borgani, S., G. Murante, V. Springel, A. Diaferio, K. Dolag, L. Moscardini, G. Tormen, L. Tornatore, and P. Tozzi: 2004, 'X-ray properties of galaxy clusters and groups from a cosmological hydrodynamical simulation'. MNRAS **348**(3), 1078–1096.

Bricman, K. and A. Gomboc: 2020, 'The Prospects of Observing Tidal Disruption Events with the Large Synoptic Survey Telescope'. ApJ **890**(1), 73.

Cannizzo, J. K., H. M. Lee, and J. Goodman: 1990, 'The Disk Accretion of a Tidally Disrupted Star onto a Massive Black Hole'. ApJ **351**, 38.

Cerioli, A., G. Lodato, and D. J. Price: 2016, 'Gas squeezing during the merger of a supermassive black hole binary'. MNRAS **457**, 939–948.

Chow, E. and J. J. Monaghan: 1997, 'Ultrarelativistic SPH'. *J. Comp. Phys.* **134**(2), 296–305.

Clark, P. C., S. C. O. Glover, and R. S. Klessen: 2008, 'The First Stellar Cluster'. ApJ **672**(2), 757–764.

Coughlin, E. R. and M. C. Begelman: 2014, 'Hyperaccretion during Tidal Disruption Events: Weakly Bound Debris Envelopes and Jets'. ApJ **781**(2), 82.

Cullen, L. and W. Dehnen: 2010, 'Inviscid smoothed particle hydrodynamics'. MNRAS **408**, 669–683.

Dai, L., J. C. McKinney, N. Roth, E. Ramirez-Ruiz, and M. C. Miller: 2018, 'A Unified Model for Tidal Disruption Events'. ApJ **859**(2), L20.

Del Zanna, L. and N. Bucciantini: 2002, 'An efficient shock-capturing central-type scheme for multidimensional relativistic flows. I. Hydrodynamics'. A&A **390**, 1177–1186.

Di Matteo, T., V. Springel, and L. Hernquist: 2005, 'Energy input from quasars regulates the growth and activity of black holes and their host galaxies'. Nature **433**(7026), 604–607.

Diener, P., V. P. Frolov, A. M. Khokhlov, I. D. Novikov, and C. J. Pethick: 1997, 'Relativistic Tidal Interaction of Stars with a Rotating Black Hole'. ApJ **479**, 164–178.

Dipierro, G., G. Laibe, D. J. Price, and G. Lodato: 2016, 'Two mechanisms for dust gap opening in protoplanetary discs'. MNRAS **459**(1), L1–L5.

Einstein, A.: 1915, 'Die Feldgleichungen der Gravitation'. *Sitzungsberichte der Königlich Preußischen Akademie der Wissenschaften (Berlin* pp. 844–847.

Evans, C. R. and C. S. Kochanek: 1989, 'The tidal disruption of a star by a massive black hole'. ApJ **346**, L13–L16.

Event Horizon Telescope Collaboration, K. Akiyama, A. Alberdi, W. Alef, K. Asada, R. Azulay, A.-K. Baczko, D. Ball, M. Baloković, J. Barrett, and et al.: 2019, 'First M87 Event Horizon Telescope Results. I. The Shadow of the Supermassive Black Hole'. ApJ **875**, L1.

Faber, J. A., P. Grandclément, and F. A. Rasio: 2004, 'Mergers of irrotational neutron star binaries in conformally flat gravity'. Phys. Rev. D **69**(12), 124036.

Finkelstein, D.: 1958, 'Past-Future Asymmetry of the Gravitational Field of a Point Particle'. *Physical Review* **110**(4), 965–967.

Fock, V. A.: 1964, *The theory of space, time and gravitation.*

Foucart, F.: 2012, 'Black-hole-neutron-star mergers: Disk mass predictions'. Phys. Rev. D **86**(12), 124007.

Fragile, P. C.: 2009, 'Effective Inner Radius of Tilted Black Hole Accretion Disks'. ApJ **706**, L246–L250.

Fragile, P. C., O. M. Blaes, P. Anninos, and J. D. Salmonson: 2007, 'Global General Relativistic Magnetohydrodynamic Simulation of a Tilted Black Hole Accretion Disk'. ApJ **668**, 417–429.

Fragile, P. C., C. C. Lindner, P. Anninos, and J. D. Salmonson: 2009, 'Application of the Cubed-Sphere Grid to Tilted Black Hole Accretion Disks'. ApJ **691**, 482–494.

Franchini, A., G. Lodato, and S. Facchini: 2016, 'Lense-Thirring precession around supermassive black holes during tidal disruption events'. MNRAS **455**(2), 1946–1956.

Frolov, V. P., A. M. Khokhlov, I. D. Novikov, and C. J. Pethick: 1994, 'Relativistic tidal interaction of a white dwarf with a massive black hole'. ApJ **432**, 680–689.

Gafton, E. and S. Rosswog: 2019, 'Tidal disruptions by rotating black holes: effects of spin and impact parameter'. MNRAS **487**(4), 4790–4808.

Gammie, C. F., J. C. McKinney, and G. Tóth: 2003, 'HARM: A Numerical Scheme for General Relativistic Magnetohydrodynamics'. ApJ **589**, 444–457.

Gezari, S., S. Basa, D. C. Martin, G. Bazin, K. Forster, B. Milliard, J. P. Halpern, P. G. Friedman, P. Morrissey, S. G. Neff, D. Schiminovich, M. Seibert, T. Small, and T. K. Wyder: 2008, 'UV/Optical Detections of Candidate Tidal Disruption Events by GALEX and CFHTLS'. *The Astrophysical Journal* **676**(2), 944–969.

Gezari, S., S. B. Cenko, and I. Arcavi: 2017, 'X-Ray Brightening and UV Fading of Tidal Disruption Event ASASSN-15oi'. ApJ **851**(2), L47.

Gezari, S., R. Chornock, A. Rest, M. E. Huber, K. Forster, E. Berger, P. J. Challis, J. D. Neill, D. C. Martin, T. Heckman, A. Lawrence, C. Norman, G. Narayan, R. J. Foley, G. H. Marion, D. Scolnic, L. Chomiuk, A. Soderberg, K. Smith, R. P. Kirshner, A. G. Riess, S. J. Smartt, C. W. Stubbs, J. L. Tonry, W. M. Wood-Vasey, W. S. Burgett, K. C. Chambers, T. Grav, J. N. Heasley, N. Kaiser, R. P. Kudritzki, E. A. Magnier, J. S. Morgan, and P. A. Price: 2012, 'An ultraviolet-optical flare from the tidal disruption of a helium-rich stellar core'. *Nature* **485**(7397), 217–220.

Giacomazzo, B. and L. Rezzolla: 2006, 'The exact solution of the Riemann problem in relativistic magnetohydrodynamics'. *Journal of Fluid Mechanics* **562**, 223–259.

Gingold, R. A. and J. J. Monaghan: 1977, 'Smoothed particle hydrodynamics - Theory and application to non-spherical stars'. MNRAS **181**, 375–389.

Goicovic, F. G., V. Springel, S. T. Ohlmann, and R. Pakmor: 2019, 'Hydrodynamical moving-mesh simulations of the tidal disruption of stars by supermassive black holes'. MNRAS **487**(1), 981–992.

Golightly, E. C. A., E. R. Coughlin, and C. J. Nixon: 2019, 'Tidal Disruption Events: The Role of Stellar Spin'. *The Astrophysical Journal* **872**(2), 163.

Governato, F., B. Willman, L. Mayer, A. Brooks, G. Stinson, O. Valenzuela, J. Wadsley, and T. Quinn: 2007, 'Forming disc galaxies in ΛCDM simulations'. MNRAS **374**(4), 1479–1494.

Guillochon, J., H. Manukian, and E. Ramirez-Ruiz: 2014, 'PS1-10jh: The Disruption of a Main-sequence Star of Near-solar Composition'. ApJ **783**, 23.

Guillochon, J. and E. Ramirez-Ruiz: 2013, 'Hydrodynamical Simulations to Determine the Feeding Rate of Black Holes by the Tidal Disruption of Stars: The Importance of the Impact Parameter and Stellar Structure'. ApJ **767**, 25.

Guillochon, J. and E. Ramirez-Ruiz: 2015, 'A Dark Year for Tidal Disruption Events'. ApJ **809**, 166.

Guillochon, J., E. Ramirez-Ruiz, S. Rosswog, and D. Kasen: 2009, 'Three-dimensional Simulations of Tidally Disrupted Solar-type Stars and the Observational Signatures of Shock Breakout'. ApJ **705**, 844–853.

Hawley, J. F., L. L. Smarr, and J. R. Wilson: 1984a, 'A numerical study of nonspherical black hole accretion. I Equations and test problems'. ApJ **277**, 296–311.

Hawley, J. F., L. L. Smarr, and J. R. Wilson: 1984b, 'A numerical study of nonspherical black hole accretion. II - Finite differencing and code calibration'. ApJS **55**, 211–246.

Hayasaki, K., N. Stone, and A. Loeb: 2013, 'Finite, intense accretion bursts from tidal disruption of stars on bound orbits'. MNRAS **434**, 909–924.

Hayasaki, K., N. Stone, and A. Loeb: 2016, 'Circularization of tidally disrupted stars around spinning supermassive black holes'. MNRAS **461**, 3760–3780.

Hills, J. G.: 1975, 'Possible power source of Seyfert galaxies and QSOs'. Nature **254**, 295–298.

Holoien, T. W. S., M. E. Huber, B. J. Shappee, M. Eracleous, K. Auchettl, J. S. Brown, M. A. Tucker, K. C. Chambers, C. S. Kochanek, K. Z. Stanek, A. Rest, D. Bersier, R. S. Post, G. Aldering, K. A. Ponder, J. D. Simon, E. Kankare, D. Dong, G. Hallinan, N. A. Reddy, R. L. Sanders, M. W. Topping, Pan-STARRS, J. Bulger, T. B. Lowe, E. A. Magnier, A. S. B. Schultz, C. Z. Waters, M. Willman, D. Wright, D. R. Young, ASAS-SN, S. Dong, J. L. Prieto, T. A. Thompson, ATLAS, L. Denneau, H. Flewelling, A. N. Heinze, S. J. Smartt, K. W. Smith, B. Stalder, J. L. Tonry, and H. Weiland: 2019, 'PS18kh: A New Tidal Disruption Event with a Non-axisymmetric Accretion Disk'. ApJ **880**(2), 120.

Holoien, T. W. S., C. S. Kochanek, J. L. Prieto, K. Z. Stanek, S. Dong, B. J. Shappee, D. Grupe, J. S. Brown, U. Basu, J. F. Beacom, D. Bersier, J. Brimacombe, A. B. Danilet, E. Falco, Z. Guo, J. Jose, G. J. Herczeg, F. Long, G. Pojmanski, G. V. Simonian, D. M. Szczygieł, T. A. Thompson, J. R. Thorstensen, R. M. Wagner, and P. R. Woźniak: 2016, 'Six months of multiwavelength follow-up of the tidal disruption candidate ASASSN-14li and implied TDE rates from ASAS-SN'. MNRAS **455**(3), 2918–2935.

Hung, T., S. Gezari, N. Blagorodnova, N. Roth, S. B. Cenko, S. R. Kulkarni, A. Horesh, I. Arcavi, C. McCully, L. Yan, R. Lunnan, C. Fremling, Y. Cao, P. E. Nugent, and P. Wozniak: 2017, 'Revisiting Optical Tidal Disruption Events with iPTF16axa'. ApJ **842**(1), 29.

Ivanov, P. B. and A. F. Illarionov: 1997, 'The oscillatory shape of the stationary twisted disc around a Kerr black hole'. MNRAS **285**, 394–402.

Ivezić, Ž., S. M. Kahn, J. A. Tyson, B. Abel, E. Acosta, R. Allsman, D. Alonso, Y. AlSayyad, S. F. Anderson, J. Andrew, and et al.: 2019, 'LSST: From Science Drivers to Reference Design and Anticipated Data Products'. ApJ **873**(2), 111.

Jiang, Y.-F., J. Guillochon, and A. Loeb: 2016, 'Prompt Radiation and Mass Outflows from the Stream-Stream Collisions of Tidal Disruption Events'. ApJ **830**(2), 125.

Kato, S.: 1990, 'Trapped one-armed corrugation waves and QPOs'. PASJ **42**, 99–113.

Kerr, R. P.: 1963, 'Gravitational Field of a Spinning Mass as an Example of Algebraically Special Metrics'. *Physical Review Letters* **11**, 237–238.

Kesden, M.: 2012, 'Black-hole spin dependence in the light curves of tidal disruption events'. Phys. Rev. D **86**(6), 064026.

Kheyfets, A., W. A. Miller, and W. H. Zurek: 1990, 'Covariant smoothed particle hydrodynamics on a curved background'. Phys. Rev. D **41**, 451–454.

Khokhlov, A., I. D. Novikov, and C. J. Pethick: 1993, 'Strong Effects during Close Encounters of a Star with a Massive Black Hole'. ApJ **418**, 181.

Kobayashi, S., P. Laguna, E. S. Phinney, and P. Mészáros: 2004, 'Gravitational Waves and X-Ray Signals from Stellar Disruption by a Massive Black Hole'. ApJ **615**, 855–865.

Komossa, S.: 2015, 'Tidal disruption of stars by supermassive black holes: Status of observations'. *Journal of High Energy Astrophysics* **7**, 148–157.

Kormendy, J. and D. Richstone: 1995, 'Inward Bound—The Search For Supermassive Black Holes In Galactic Nuclei'. ARA&A **33**, 581.

Laguna, P., W. A. Miller, and W. H. Zurek: 1993, 'Smoothed particle hydrodynamics near a black hole'. ApJ **404**, 678–685.

Lanzafame, G., D. Molteni, and S. K. Chakrabarti: 1998, 'Smoothed particle hydrodynamic simulations of viscous accretion discs around black holes'. MNRAS **299**(3), 799–804.

Leimkuhler, B. and S. Reich: 2005, *Simulating Hamiltonian Dynamics*, Cambridge Monographs on Applied and Computational Mathematics. Cambridge University Press.

Leloudas, G., L. Dai, I. Arcavi, P. M. Vreeswijk, B. Mockler, R. Roy, D. B. Malesani, S. Schulze, T. Wevers, M. Fraser, E. Ramirez-Ruiz, K. Auchettl, J. Burke, G. Cannizzaro, P. Charalampopoulos, T.-W. Chen, A. a. Cikota, M. Della Valle, L. Galbany, M. Gromadzki, K. E. Heintz, D. Hiramatsu, P. G. Jonker, Z. Kostrzewa-Rutkowska, K. Maguire, I. Mandel, F. Onori, N. Roth, S. J. Smartt, L. Wyrzykowski, and D. R. Young: 2019, 'The spectral evolution of AT 2018dyb and the presence of metal lines in tidal disruption events'. *arXiv e-prints* p. arXiv:1903.03120.

Lidskii, V. V. and L. M. Ozernoi: 1979, 'Tidal triggering of stellar flares by a massive black hole'. *Soviet Astronomy Letters* **5**, 16–19.

Liptai, D. and D. J. Price: 2019, 'General relativistic smoothed particle hydrodynamics'. MNRAS **485**, 819–842.

Liptai, D., D. J. Price, I. Mandel, and G. Lodato: 2019, 'Disc formation from tidal disruption of stars on eccentric orbits by Kerr black holes using GRSPH'. *arXiv e-prints* p. arXiv:1910.10154.

Liptai, D., D. J. Price, J. Wurster, and M. R. Bate: 2017, 'Does turbulence determine the initial mass function?'. MNRAS **465**, 105–110.

Lodato, G.: 2012, 'Challenges in the modeling of tidal disruption events lightcurves'. In: *European Physical Journal Web of Conferences*, Vol. 39 of *European Physical Journal Web of Conferences*. p. 01001.

Lodato, G., A. Franchini, C. Bonnerot, and E. M. Rossi: 2015, 'Recent developments in the theory of tidal disruption events'. *Journal of High Energy Astrophysics* **7**, 158–162.

Lodato, G., A. R. King, and J. E. Pringle: 2009, 'Stellar disruption by a supermassive black hole: is the light curve really proportional to $t^{-5/3}$'. MNRAS **392**, 332–340.

Lodato, G. and D. J. Price: 2010, 'On the diffusive propagation of warps in thin accretion discs'. MNRAS **405**, 1212–1226.

Lodato, G. and E. M. Rossi: 2011, 'Multiband light curves of tidal disruption events'. MNRAS **410**(1), 359–367.

Loeb, A. and A. Ulmer: 1997, 'Optical Appearance of the Debris of a Star Disrupted by a Massive Black Hole'. ApJ **489**(2), 573–578.

Lubow, S. H., G. I. Ogilvie, and J. E. Pringle: 2002, 'The evolution of a warped disc around a Kerr black hole'. MNRAS **337**, 706–712.

Lucy, L. B.: 1977, 'A numerical approach to the testing of the fission hypothesis'. AJ **82**, 1013–1024.

Lufkin, G., T. Quinn, J. Wadsley, J. Stadel, and F. Governato: 2004, 'Simulations of gaseous disc-embedded planet interaction'. MNRAS **347**(2), 421–429.

MacLeod, M., J. Guillochon, and E. Ramirez-Ruiz: 2012, 'The Tidal Disruption of Giant Stars and their Contribution to the Flaring Supermassive Black Hole Population'. ApJ **757**(2), 134.

Mann, P. J.: 1991, 'A relativistic smoothed particle hydrodynamics method tested with the shock tube'. *Computer Physics Communications* **67**, 245–260.

Martí, J. M., J. M. Ibáez, and J. A. Miralles: 1991, 'Numerical relativistic hydrodynamics: Local characteristic approach'. Phys. Rev. D **43**, 3794–3801.

Martí, J. M. and E. Müller: 1994, 'Analytical solution of the Riemann problem in relativistic hydrodynamics'. *Journal of Fluid Mechanics* **258**, 317–333.

Martí, J. M. and E. Müller: 2003, 'Numerical Hydrodynamics in Special Relativity'. *Living Reviews in Relativity* **6**, 7.

Martí, J. M. and E. Müller: 2015, 'Grid-based Methods in Relativistic Hydrodynamics and Magnetohydrodynamics'. *Living Reviews in Computational Astrophysics* **1**, 3.

Mayer, L., T. Quinn, J. Wadsley, and J. Stadel: 2002, 'Formation of Giant Planets by Fragmentation of Protoplanetary Disks'. *Science* **298**(5599), 1756–1759.

Metzger, B. D.: 2017, 'Kilonovae'. *Living Reviews in Relativity* **20**, 3.

Metzger, B. D. and N. C. Stone: 2016, 'A bright year for tidal disruptions'. *Monthly Notices of the Royal Astronomical Society* **461**(1), 948–966.

Michel, F. C.: 1972, 'Accretion of Matter by Condensed Objects'. Ap&SS **15**, 153–160.

Mihos, J. C. and L. Hernquist: 1996, 'Gasdynamics and Starbursts in Major Mergers'. ApJ **464**, 641.

Miller, M. C.: 2015, 'Disk Winds as an Explanation for Slowly Evolving Temperatures in Tidal Disruption Events'. ApJ **805**(1), 83.

Milosavljević, M. and E. S. Phinney: 2005, 'The Afterglow of Massive Black Hole Coalescence'. ApJ **622**, L93–L96.

Mitalas, R. and K. R. Sills: 1992, 'On the Photon Diffusion Time Scale for the Sun'. ApJ **401**, 759.

Monaghan, J. J.: 1992, 'Smoothed particle hydrodynamics'. ARA&A **30**, 543–574.

Monaghan, J. J.: 1997, 'SPH and Riemann Solvers'. *Journal of Computational Physics* **136**, 298–307.

Monaghan, J. J.: 2002, 'SPH compressible turbulence'. MNRAS **335**, 843–852.

Monaghan, J. J.: 2005, 'Smoothed particle hydrodynamics'. *Reports on Progress in Physics* **68**(8), 1703–1759.

Monaghan, J. J. and D. J. Price: 2001, 'Variational principles for relativistic smoothed particle hydrodynamics'. MNRAS **328**, 381–392.

Montgomery, C., W. Orchiston, and I. Whittingham: 2009, 'Michell, Laplace and the origin of the black hole concept'. *Journal of Astronomical History and Heritage* **12**(2), 90–96.

Morales Teixeira, D., P. C. Fragile, V. V. Zhuravlev, and P. B. Ivanov: 2014, 'Conservative GRMHD Simulations of Moderately Thin, Tilted Accretion Disks'. ApJ **796**, 103.

Morris, J. P. and J. J. Monaghan: 1997, 'A Switch to Reduce SPH Viscosity'. *Journal of Computational Physics* **136**, 41–50.

Nealon, R., D. J. Price, and C. J. Nixon: 2015, 'On the Bardeen–Petterson effect in black hole accretion discs'. MNRAS **448**(2), 1526–1540.

Nicholl, M., P. K. Blanchard, E. Berger, S. Gomez, R. Margutti, K. D. Alexander, J. Guillochon, J. Leja, R. Chornock, B. Snios, K. Auchettl, A. G. Bruce, P. Challis, D. J. D'Orazio, M. R. Drout, T. Eftekhari, R. J. Foley, O. Graur, C. D. Kilpatrick, A. Lawrence, A. L. Piro, C. Rojas-Bravo, N. P. Ross, P. Short, S. J. Smartt, K. W. Smith, and B. Stalder: 2019, 'The tidal disruption event AT2017eqx: spectroscopic evolution from hydrogen rich to poor suggests an atmosphere and outflow'. MNRAS **488**(2), 1878–1893.

Nixon, C., A. King, D. Price, and J. Frank: 2012, 'Tearing up the Disk: How Black Holes Accrete'. ApJ **757**, L24.

Nixon, C. and G. Salvesen: 2014, 'A physical model for state transitions in black hole X-ray binaries'. MNRAS **437**, 3994–3999.

Oechslin, R., H. T. Janka, and A. Marek: 2007, 'Relativistic neutron star merger simulations with non-zero temperature equations of state. I. Variation of binary parameters and equation of state'. A&A **467**(2), 395–409.

Oechslin, R., S. Rosswog, and F.-K. Thielemann: 2002, 'Conformally flat smoothed particle hydrodynamics application to neutron star mergers'. *Physical Review D* **65**(10), 103005.

Okazaki, A. T., S. Nagataki, T. Naito, A. Kawachi, K. Hayasaki, S. P. Owocki, and J. Takata: 2011, 'Hydrodynamic Interaction between the Be Star and the Pulsar in the TeV Binary PSR B1259-63/LS 2883'. PASJ **63**, 893–901.

Oppenheimer, J. R. and H. Snyder: 1939, 'On Continued Gravitational Contraction'. *Physical Review* **56**(5), 455–459.

Oppenheimer, J. R. and G. M. Volkoff: 1939, 'On Massive Neutron Cores'. *Physical Review* **55**(4), 374–381.

Pasham, D. R., S. B. Cenko, A. Sadowski, J. Guillochon, N. C. Stone, S. van Velzen, and J. K. Cannizzo: 2017, 'Optical/UV-to-X-Ray Echoes from the Tidal Disruption Flare ASASSN-14li'. ApJ **837**(2), L30.

Phinney, E. S.: 1989, 'Manifestations of a Massive Black Hole in the Galactic Center'. In: M. Morris (ed.): *The Center of the Galaxy*, Vol. 136 of *IAU Symposium*. p. 543.

Pihajoki, P.: 2015, 'Explicit methods in extended phase space for inseparable Hamiltonian problems'. *Celestial Mechanics and Dynamical Astronomy* **121**(3), 211–231.

Piran, T., G. Svirski, J. Krolik, R. M. Cheng, and H. Shiokawa: 2015, 'Disk Formation Versus Disk Accretion - What Powers Tidal Disruption Events?'. ApJ **806**, 164.

Price, D. J.: 2008, 'Modelling discontinuities and Kelvin Helmholtz instabilities in SPH'. *Journal of Computational Physics* **227**, 10040–10057.

Price, D. J.: 2012, 'Smoothed particle hydrodynamics and magnetohydrodynamics'. *Journal of Computational Physics* **231**, 759–794.

Price, D. J. and C. Federrath: 2010, 'A comparison between grid and particle methods on the statistics of driven, supersonic, isothermal turbulence'. MNRAS **406**, 1659–1674.

Price, D. J. and J. J. Monaghan: 2007, 'An energy-conserving formalism for adaptive gravitational force softening in smoothed particle hydrodynamics and N-body codes'. MNRAS **374**, 1347–1358.

Price, D. J., J. Wurster, T. S. Tricco, C. Nixon, S. Toupin, A. Pettitt, C. Chan, D. Mentiplay, G. Laibe, S. Glover, C. Dobbs, R. Nealon, D. Liptai, H. Worpel, C. Bonnerot, G. Dipierro, G. Ballabio, E. Ragusa, C. Federrath, R. Iaconi, T. Reichardt, D. Forgan, M. Hutchison, T. Constantino, B. Ayliffe, K. Hirsh, and G. Lodato: 2018, 'Phantom: A Smoothed Particle Hydrodynamics and Magnetohydrodynamics Code for Astrophysics'. PASA **35**, e031.

Ramirez-Ruiz, E. and S. Rosswog: 2009, 'The Star Ingesting Luminosity of Intermediate-Mass Black Holes in Globular Clusters'. ApJ **697**, L77–L80.

Rees, M. J.: 1988, 'Tidal disruption of stars by black holes of 10 to the 6th-10 to the 8th solar masses in nearby galaxies'. Nature **333**, 523–528.

Remillard, R. A. and J. E. McClintock: 2006, 'X-Ray Properties of Black-Hole Binaries'. ARA&A **44**(1), 49–92.

Rosen, A., P. A. Hughes, G. C. Duncan, and P. E. Hardee: 1999, 'A Comparison of the Morphology and Stability of Relativistic and Nonrelativistic Jets'. ApJ **516**(2), 729–743.

Rosswog, S.: 2009, 'Astrophysical smooth particle hydrodynamics'. *New Astronomy Reviews* **53**(4–6), 78–104.

Rosswog, S.: 2010a, 'Conservative, special-relativistic smoothed particle hydrodynamics'. *Journal of Computational Physics* **229**, 8591–8612.

Rosswog, S.: 2010b, 'Relativistic smooth particle hydrodynamics on a given background spacetime'. *Classical and Quantum Gravity* **27**(11), 114108.

Rosswog, S., E. Ramirez-Ruiz, W. R. Hix, and M. Dan: 2008, 'Simulating black hole white dwarf encounters'. *Computer Physics Communications* **179**, 184–189.

Roth, N. and D. Kasen: 2018, 'What Sets the Line Profiles in Tidal Disruption Events?'. ApJ **855**(1), 54.

Roth, N., D. Kasen, J. Guillochon, and E. Ramirez-Ruiz: 2016, 'The X-Ray through Optical Fluxes and Line Strengths of Tidal Disruption Events'. ApJ **827**(1), 3.

Ryu, T., J. Krolik, T. Piran, and S. C. Noble: 2020, 'Tidal disruptions of main sequence stars – II. Simulation methodology and stellar mass dependence of the character of full tidal disruptions'. *arXiv e-prints* p. arXiv:2001.03502.

Sacchi, A. and G. Lodato: 2019, ''Failed' tidal disruption events and X-ray flares from the Galactic Centre'. MNRAS **486**(2), 1833–1839.

Sadowski, A., E. Tejeda, E. Gafton, S. Rosswog, and D. Abarca: 2016, 'Magnetohydrodynamical simulations of a deep tidal disruption in general relativity'. MNRAS **458**(4), 4250–4268.

Salpeter, E. E.: 1964, 'Accretion of Interstellar Matter by Massive Objects.'. ApJ **140**, 796–800.

Schmidt, M.: 1963, '3C 273 : A Star-Like Object with Large Red-Shift'. Nature **197**(4872), 1040.

Schwarzschild, K.: 1916, 'On the Gravitational Field of a Mass Point According to Einstein's Theory'. *Abh. Konigl. Preuss. Akad. Wissenschaften Jahre 1906,92, Berlin,1907* **1916**, 189–196.

Shakura, N. I. and R. A. Sunyaev: 1973, 'Black holes in binary systems. Observational appearance.'. A&A **24**, 337–355.

Shiokawa, H., J. H. Krolik, R. M. Cheng, T. Piran, and S. C. Noble: 2015, 'General Relativistic Hydrodynamic Simulation of Accretion Flow from a Stellar Tidal Disruption'. ApJ **804**, 85.

Siegler, S. and H. Riffert: 2000, 'Smoothed Particle Hydrodynamics Simulations of Ultrarelativistic Shocks with Artificial Viscosity'. ApJ **531**, 1053–1066.

Springel, V.: 2005, 'The cosmological simulation code GADGET-2'. MNRAS **364**(4), 1105–1134.

Springel, V. and L. Hernquist: 2002, 'Cosmological smoothed particle hydrodynamics simulations: the entropy equation'. MNRAS **333**, 649–664.

Springel, V. and L. Hernquist: 2003, 'Cosmological smoothed particle hydrodynamics simulations: a hybrid multiphase model for star formation'. MNRAS **339**(2), 289–311.

Stern, J., A. Laor, and A. Baskin: 2014, 'Radiation pressure confinement - I. Ionized gas in the ISM of AGN hosts'. MNRAS **438**(2), 901–921.

Stone, N. C., M. Kesden, R. M. Cheng, and S. van Velzen: 2019, 'Stellar tidal disruption events in general relativity'. *General Relativity and Gravitation* **51**, 30.

Stone, N. C. and B. D. Metzger: 2016, 'Rates of stellar tidal disruption as probes of the supermassive black hole mass function'. MNRAS **455**(1), 859–883.

Strubbe, L. E. and E. Quataert: 2009, 'Optical flares from the tidal disruption of stars by massive black holes'. MNRAS **400**(4), 2070–2084.

Svirski, G., T. Piran, and J. Krolik: 2017, 'Elliptical Accretion and Low Luminosity from High Accretion Rate Stellar Tidal Disruption Events'. MNRAS **467**(2), 1426–1432.

Tao, M.: 2016, 'Explicit symplectic approximation of nonseparable Hamiltonians: Algorithm and long time performance'. Phys. Rev. E **94**(4), 043303.

Tejeda, E.: 2012, 'An analytic Kerr-accretion model as a test solution for a new GR SPH code'. Ph.D. thesis, International School for Advanced Studies Via Bonomea 265, 34136 Trieste, Italy.

Tejeda, E., E. Gafton, S. Rosswog, and J. C. Miller: 2017, 'Tidal disruptions by rotating black holes: relativistic hydrodynamics with Newtonian codes'. MNRAS **469**, 4483–4503.

Tejeda, E. and S. Rosswog: 2013, 'An accurate Newtonian description of particle motion around a Schwarzschild black hole'. MNRAS **433**(3), 1930–1940.

Thorp, S., E. Chadwick, and A. Sesana: 2019, 'Tidal disruption events from massive black hole binaries: predictions for ongoing and future surveys'. MNRAS **488**(3), 4042–4060.

Toupin, S., K. Braun, L. Siess, A. Jorissen, H.-P. Gail, and D. Price: 2015a, '3D Simulation of a Dust-Driven Wind In a Binary System'. In: *EAS Publications Series*, Vol. 71 of *EAS Publications Series*. pp. 173–174.

Toupin, S., K. Braun, L. Siess, A. Jorissen, and D. Price: 2015b, 'Hydrodynamics of Mass Transfer in Binary Star Systems'. In: F. Kerschbaum, R. F. Wing, and J. Hron (eds.): *Why Galaxies Care about AGB Stars III: A Closer Look in Space and Time*, Vol. 497 of *Astronomical Society of the Pacific Conference Series*. p. 225.

Tuckerman, M., B. J. Berne, and G. J. Martyna: 1992, 'Reversible multiple time scale molecular dynamics'. J. Chem. Phys. **97**, 1990–2001.

van Velzen, S.: 2018, 'On the Mass and Luminosity Functions of Tidal Disruption Flares: Rate Suppression due to Black Hole Event Horizons'. ApJ **852**(2), 72.

van Velzen, S., G. R. Farrar, S. Gezari, N. Morrell, D. Zaritsky, L. Östman, M. Smith, J. Gelfand, and A. J. Drake: 2011, 'Optical Discovery of Probable Stellar Tidal Disruption Flares'. ApJ **741**(2), 73.

van Velzen, S., S. Gezari, E. Hammerstein, N. Roth, S. Frederick, C. Ward, T. Hung, S. B. Cenko, R. Stein, D. A. Perley, K. Taggart, J. Sollerman, I. Andreoni, E. C. Bellm, V. Brinnel, K. De, R. Dekany, M. Feeney, R. J. Foley, C. Fremling, M. Giomi, V. Z. Golkhou, A. Y. Q. Ho, M. M. Kasliwal, C. D. Kilpatrick, S. R. Kulkarni, T. Kupfer, R. R. Laher, A. Mahabal, F. J. Masci, J. Nordin, R. Riddle, B. Rusholme, Y. Sharma, J. van Santen, D. L. Shupe, and M. T. Soumagnac: 2020, 'Seventeen Tidal Disruption Events from the First Half of ZTF Survey Observations: Entering a New Era of Population Studies'. *arXiv e-prints* p. arXiv:2001.01409.

van Velzen, S., N. C. Stone, B. D. Metzger, S. Gezari, T. M. Brown, and A. S. Fruchter: 2019, 'Late-time UV Observations of Tidal Disruption Flares Reveal Unobscured, Compact Accretion Disks'. ApJ **878**(2), 82.

Verlet, L.: 1967, 'Computer "Experiments" on Classical Fluids. I. Thermodynamical Properties of Lennard-Jones Molecules'. *Physical Review* **159**, 98–103.

Vigneron, Q., G. Lodato, and A. Guidarelli: 2018, 'Tidal disruption of stars in a supermassive black hole binary system: the influence of orbital properties on fallback and accretion rates'. MNRAS **476**, 5312–5322.

Wadsley, J. W., J. Stadel, and T. Quinn: 2004, 'Gasoline: a flexible, parallel implementation of TreeSPH'. New A **9**(2), 137–158.

Wadsley, J. W., G. Veeravalli, and H. M. P. Couchman: 2008, 'On the treatment of entropy mixing in numerical cosmology'. MNRAS **387**, 427–438.

Webster, B. L. and P. Murdin: 1972, 'Cygnus X-1-a Spectroscopic Binary with a Heavy Companion ?'. Nature **235**(5332), 37–38.

Wegg, C.: 2012, 'Pseudo-Newtonian Potentials for Nearly Parabolic Orbits'. ApJ **749**, 183.

Yalinewich, A., J. Guillochon, R. Sari, and A. Loeb: 2019, 'Shock breakouts from tidal disruption events'. MNRAS **482**(3), 2872–2877.

Yoshida, H.: 1993, 'Recent Progress in the Theory and Application of Symplectic Integrators'. *Celestial Mechanics and Dynamical Astronomy* **56**, 27–43.

Zel'dovich, Y. B.: 1964, 'The Fate of a Star and the Evolution of Gravitational Energy Upon Accretion'. *Soviet Physics Doklady* **9**, 195.

Zhang, W. and A. I. MacFadyen: 2006, 'RAM: A Relativistic Adaptive Mesh Refinement Hydrodynamics Code'. ApJS **164**, 255–279.